The Formation and Evolution of Bars, and Its Impact on Galaxy Dynamics

A THESIS

SUBMITTED FOR THE DEGREE OF

Doctor of Philosophy

IN THE FACULTY OF SCIENCE

by

Sandeep Kumar Kataria

Joint Astronomy Programme
Department of Physics
Indian Institute of Science
Bangalore – 560 012, INDIA

July 31, 2019

Declaration

I hereby declare that the work reported in this doctoral thesis titled "The Formation and Evolution of Bars, and Its Impact on Galaxy Dynamics" is entirely original and is the result of investigations carried out by me in the Department of Physics, Indian Institute of Science, Bangalore, under the supervision of Prof. Mousumi Das at Indian Institute of Astrophysics, Bangalore.

I further declare that this work has not formed the basis for the award of any degree, diploma, fellowship, associateship or similar title of any University or Institution.

Date:
Bangalore, India

Sandeep Kumar Kataria
Department of Physics
Indian Institute of Science

To,
My Family

Acknowledgements

Here I would like to thank those with whom I have good interaction at some point of time during my PhD. These communications certainly shaped the work presented in this thesis.

First of all I would like to heartily thank my supervisor Prof. Mousumi Das for her continuous support and guidance to reach the finishing point. I want to thank her for providing a friendly environment which helped me in learning various skills required for my research. I would like to thank my collaborators Dr. Sudhanshu Barway and Prof. Stacy McGaugh with whom I had several interesting and thought provoking discussions.

I would also like to thank other faculties from various institutes in Bangalore: Prof. Preeti Kharb(currently at NCRA), Prof. Pravabati Chingangbam, Prof. S. P. Rajaguru, Prof. Prateek Sharma, Prof. Sivrani, Prof. Chanda Jog, Prof. Nirupam Roy, Prof. Tarun Deep Saini, Prof. Sridhar S, Prof. Manish Jain, Prof. Sreekumar, Prof. Biman Nath, Prof. Annapoorni, Prof. Smitha, Prof. Ravinder, Prof. Ganesan Srinivasan, Prof. Kanak.

I would also like to thank Prof. Volker Springel, and Prof. Monica Valluri with whom I had various discussions related to my research mostly over email communications.

Further I would also like to thank to senior/contemporary/junior friends at various institutes (IIA, RRI, IISc, IIT Kgp) with whom I had discussions about astronomy: Gopal, Soumovo, Sudip, Aabir, Deovrat, Kartick, Priyanka, Karamveer, Prasun, Upasana, Arpita, Avijeet, Sajal, Prasanna, Honey, Vaibhav, Saurabh, Jankee, Priyanka, Susmita Rubinur, Prasanta, Avrajeet, Avinash, Sidhartha, Akanksha, Raj, Nancy, Olushina, Samrat, Chayan, Deepanwita, Tridib, Snehalata, Anirban, Megha, Rahool, Krishna, Pavan, Panini, Ritesh, Bhoomika, Prerna, Priya, Deepak, Raghubar, Aritra, Pavana, Suchira, Ritesh, Ankit, Jyoti, Sioree, Fazlu, Harsh, Satabdwa, Anirbaan, Tushar, Soumya, Partha, Suman, Athira, Subhankar, Sahel.

Apart from this I would also like to thank various post doctoral fellows from whom I got encouragement to work better: Naveen, Benjamin, Brajesh, Suvendu, Kanhaiya, Ashish, Supriyo, Chandrashekhar, Dipen.

Most of the simulation work in the thesis have been done on HYDRA and NOVA (IIA), CRAY Machine (IISc) and ULMO (CWRU). I would like to acknowledge various staff member who helped me familiarizing with cluster environment: Anish, Fayaz, Charlie.

I would also like to thank all the staff members at IIA and IISc.

Finally, I will thank my family members who always supported me during high and low tide phases of life. I will thank my dad for his continuous encouragement to do better in life.

Preface

Observations of galaxies show that in the nearby universe we see that approximately 2/3 of the disk galaxies are barred ones (Eskridge et al., 2000). The formation and evolution scenarios of bars are mainly studied with N-body simulations. In an isolated disk galaxy which is rotationally supported, the disk tends to form a bar as it has globally unstable modes (Kalnajs, 1972). It has been suggested that a massive halo surrounding the disk can stabilize it against bar type instabilities (Ostriker & Peebles, 1973) by increasing the random motion of the stars. There are several other studies which claims that central mass concentration may not allow bars to form. It is also known that as disks become bar unstable, it transport the angular momentum from the inner disk to outer disk as well as to the surrounding dark matter halo.

In this thesis we have studied bar formation and evolution using N-body simulations. We have focused on the effect of bulge mass and concentration on bar formation and evolution, and derived a new bar formation criterion. We also tested the criterion with observations collected from literature. We then investigated the effect of bulge mass on bar pattern speed since observations do not give a clear idea of the nature and origin of slow and fast of bars in galaxies. Bars also a potential candidate for changing the dark matter profile in the central regions of galaxies as they transports angular momentum from disk to the dark halo. We have also studied this effect using N-body simulations. We have given a brief introduction about barred galaxies and its formation mechanisms in the Chapter 1 of thesis. In the following paragraphs we summarize our thesis projects along with the main results.

I. The Effect of Bulges on Bar Formation and Evolution.

We use N-body simulations of bar formation in an isolated galaxy to study the effect of bulge mass and bulge concentration on bar formation and its evolution. Two sets of models are generated using GalIC code (Yurin & Springel, 2014), one that has a dense bulge and high surface density disk and a second model that has a less concentrated bulge and a lighter disk. We have evolved these galaxy models using GADGET-2 code (Springel, 2005) which computes the gravitational forces among the particles.

Our simulations of both the models show that there is an upper cut-off in bulge to disk mass ratio M_b/M_d above which bars cannot form; the cut-off is smaller for denser bulges (Mb/Md = 0.2) compared to less dense ones ($M_b/M_d = 0.5$). We define a new criterion for bar formation in terms of bulge to disk radial force ratio (F_b/F_d) at the disk scale length above which bars cannot form and show that if $F_b/F_d > 0.35$, a disk is stable against bar formation (Kataria & Das, 2018). We further cross check our results with the observations of galaxies which require following observable quantities: bulge masses, disk scale lengths and rotation curves of galaxies at disk scale length.

II. Observational Test for Bar Formation Criterion.

It is well known that massive bulges impede bar formation in disk galaxies. Recent N-body simulations have derived a bar formation criterion that depends on the radial bulge force in the galaxy disk. We test this theoretical prediction using observational data obtained from the literature. Our sample consists of 39 barred galaxies with a wide range of Hubble classes from the *S*4*G* catalogue (Salo et al., 2015) for which bulge, disk and bar decomposition have been done. We find that all of our sample galaxies satisfy the condition F_b/F_d <0.35 and hence agree with the theoretical bar formation criterion given by simulations, even though a few galaxies in the sample have very massive bulges. We find that this criterion have few caveats: (a) it is valid for galaxies which has just formed bar, (b) effect of velocity dispersion which is a result of several physical processes like spiral arms, interactions and mergers has not been included, may be important.

III. Effect of Bulge Mass on Bar Pattern Speed.

Earlier studies have shown that bars transfer angular momentum from the inner to outer disks of galaxies and to their surrounding dark matter halos. The result is the slowdown of bar pattern speeds. In this work we investigate how the mass of the other spheroidal component, the bulge, affects bar pattern speeds. We find that the decrease in bar pattern speed clearly depends on bulge mass in galaxies and decreases faster for those with more massive bulges. We also find that the gain in angular momentum by bulges is larger for more massive bulges. Our results indicate that the dynamical friction of bulges on bars results in the slowdown of their pattern speeds, which is similar to the dynamical friction exerted by galaxy halos on bars. We discuss the implications of our results for observations of bar pattern speeds in galaxies.

IV. Can Bars Erode Cuspy Halos ?

One of the major and long standing problems of the widely accepted Lambda CDM cosmological model is the core-cusp problem (de Blok, 2010), which is the following - observations

show that the dark matter profile of galaxy halos in the inner regions of galaxies is flat, while cosmological simulations produce galaxies that have steep or cuspy dark matter profiles. There have been several attempts to resolve this problem, which includes baryonic processes such as supernova feedback and infalling satellites. But there is no general solution to this problem, which can explain the observed flat core nature of dark matter halos in all disk galaxies. In this study we use N-body simulations to investigate whether bar instabilities can erode cuspy dark matter halos profiles and change them into flatter core profiles.

We find that the resolution of the simulations plays an important role in determining the final results, as the cusp to core transition occurs for only low resolution simulations. As the resolution is increased, i.e. number of disk particles becomes larger, the cusp-to-core transition takes $\sim 7 \times 10^9$ years which is too long to be meaningful for eroding the cusps of dark matter halos.

List of Publications

1. **Kataria, S.** & Das, M., 2018, *A Study of the Effect of Bulges on Bar Formation in Disk galaxies*. **Monthly Notices of the Royal Astronomical Society, 475, 1653**.

2. **Kataria, S.** & Das, M., 2019. *The Effect of Bulge Mass on Bar Pattern Speed in Disk Galaxies*. **Astrophysical Journal, 886, 1**.

Table of contents

List of figures

List of tables

Science is not perfect. It's often misused; it's only a tool, but it's the best tool we have. Self-correcting, ever changing, applicable to everything: with this tool, we vanquish the impossible

Carl Sagan

1 Introduction

Galaxies in our nearby universe have a wide variety of shapes but can be broadly classified as ellipticals, spirals and irregulars depending on their morphological features. They are arranged in a sequence widely known as the Hubble Sequence (Hubble, 1926), which is in the shape of a tuning fork, with ellipticals on one side and barred/unbarred galaxies on the other side. The physics of the formation and evolution of galaxies can be understood with the help of numerical simulations, which have emerged as an important tool for understanding astrophysical systems. Simulations are especially important for understanding the large scale distribution of galaxies. We know that the widely accepted LCDM model of cosmology explains most the large scale structure of universe, although it has several problems on smaller scales such as the problem of missing satellites, cuspy dark matter halos and the existence of bulgeless galaxies (Weinzirl et al., 2009; Kormendy et al., 2010; Del Popolo & Le Delliou, 2017) . In the past few decades, a huge amount of scientific effort has been put into understanding galaxy formation and evolution and trying to fit it with the global snapshot of the Universe. In this thesis we focus on how non-axisymmetric instabilities such as bars form in disk galaxies and how they affect the overall dynamical evolution of these systems.

1.1 Barred Galaxies

We know that most of the disk galaxies in the local universe are non-axisymmetric. These non-axisymmetric features correspond to bars and spiral arms in the disk. Bars appear as elongated features in the centres of disk galaxies. Optical observations do not provide a complete idea about the fraction of barred galaxies in our local Universe as it is limited by the dust obscuration from star forming regions in disk galaxies. For example, the same sample of galaxies observed in H-band infra-red observations (Eskridge et al., 2000) give almost double the bar fraction as observed in optical catalogues such as the Third Reference Catalogue RC3 (de Vaucouleurs, 1991) and the Carnegie Atlas of Galaxies (Sandage & Bedke, 1994). It is also seen that some observations show a slightly higher bar fraction in the near-infrared (NIR) than in the optical (Knapen et al., 2000; Eskridge et al., 2000) , while others do not (Menéndez-Delmestre et al., 2007; Sheth et al., 2008). All together optical and infra-red observations (Eskridge et al., 2000; Knapen et al., 2000; Menéndez-Delmestre et al., 2007; Reese et al., 2007; Barazza et al., 2008; Sheth et al., 2008) show that two-thirds of the disk galaxies in our local Universe are barred. This fraction includes both strong and weak bars in the galaxies. The variation of bar fraction with the redshifts has also been a part of earlier studies as it gives an idea about bar survival in the disks. Many studies show that the fraction of barred galaxies decreases with redshift (Sheth et al., 2008; Nair & Abraham, 2010; Melvin et al., 2014) but some observations have found constant bar fractions up to z$\sim$1 (Elmegreen et al., 2004; Jogee et al., 2004; Marinova & Jogee, 2007) or even z$\sim$2 (Simmons et al., 2014). The latter maybe attributed to the inclusion of small size bars and different galaxy selection criteria in different surveys. However, it appears from these observations that most of the bars survive for at least t$\sim$8 Gyr in galaxies in our low redshift Universe.

Figure 1.1, 1.2 and 1.3 show the NIR and optical images of the barred spiral galaxies NGC1300, NGC1365 and NGC1097. The galaxy NGC1300 lies in the Eridanus constellation while NGC1365 and NGC1097 lie in Fornax constellation. Although bars are common among disk galaxies, their formation mechanism is not clearly understood. Given the complex background of galaxy disks, their formation mechanism is not easy to understand without numerical simulations. We will discuss the different formation mechanism in the later part of this chapter. In the following section, we discuss more about the observational properties of bars in disk galaxies.

Bar properties vary significantly from early to late type spiral galaxies in the Hubble sequence (Elmegreen & Elmegreen, 1985; Binney & Merrifield, 1998; Elmegreen, 1998; Buta et al., 2015). Bars in early type Hubble galaxies have flat surface brightness profile with sharp cutoff at the edges while bars in late type galaxies have exponential profile similar to disk profile. The bars are lengthier for early type galaxies (between corotation and inner 4:1 resonance)

Fig. 1.1 Above image of NGC1300 was taken by ACS instrument of HST in I,R,B and H-alpha band. The spiral arm of NGC1300 contains clusters of blue stars, pink star forming clouds and star forming regions. Two prominent dust lanes cut through the central bar region which merge into central spiral region.

Fig. 1.2 The image of NGC1365 is captured by FORS1 instrument of VLT UT1 in B, V and R optical bands.

Fig. 1.3 The above image of NGC1097 is taken by multi-mode VIMOS instrument of VLT in B, V and R bands. This is an interacting galaxy with it's satellite galaxy NGC1097A which is evident from the tidal tails.

compare to late type galaxies (between ILR and inner 4:1 resonance). Recent studies (Lee et al., 2019) claim that strong bars are prominent in early type galaxies while weak bars are more common in late type galaxies.

1.2 The Bar in the Milky Way

It is well known that our galaxy, the Milky Way (MW) has a bar in its center. The presence of a bar in the MW has been shown by many studies using different approaches i.e. gas kinematics and NIR photometry (Binney et al., 1991; Weiland et al., 1994), star counts of red clump giants (RCGs) (Stanek et al., 1994, 1997; Babusiaux & Gilmore, 2005; Rattenbury et al., 2007), giant star counts (López-Corredoira et al., 2005), COBE integrated NIR emission (Dwek et al., 1995; Binney et al., 1997; Freudenreich, 1998; Bissantz & Gerhard, 2002). Furthermore, the presence of an X-shape bulge or B/P bulge has been shown using two different magnitudes of RCG stars in the central region close to the bulge minor axis $|b| > 5^{\circ}$ (McWilliam & Zoccali, 2010; Nataf et al., 2010). Such B/P bulges are commonly detected in N-body simulations of bars (Athanassoula, 2005; Martinez-Valpuesta et al., 2006; Erwin & Debattista, 2013; Kataria & Das, 2018).

Recent studies (Wegg et al., 2015b) have also determined the properties of the MW bar outside the bulge region, using homogenized data from following surveys: the United Kingdom Infrared Deep Sky Survey (UKIDSS) Galactic Plane Survey (GPS) (Cabrera-Lavers et al., 2008), the Vista Variables in Via Lactea (VVV) (Saito et al., 2012), 2Mass data (Skrutskie et al., 2006), GLIMPSE data (Benjamin et al., 2003; Churchwell et al., 2005a,b) which covers the central region of MW; $|l| < 40^{\circ}$, $|b| < 9^{\circ}$. In this recent study the bar extends to $l \approx 25^{\circ}$ at $b \approx 5^{\circ}$ while it extends to $l \approx 30^{\circ}$ at lower latitudes. It lies at an angle of $28 - 33^{\circ}$ which is aligned with the bulge of the MW (Cao et al., 2013; Wegg & Gerhard, 2013). Half the bar length in this study corresponds to (5.0 $\pm$0.2) kpc which is larger than previous studies (4.5 kpc by Cabrera-Lavers et al. (2008)). These different bar lengths correspond to differences in the observed bar angles in the various studies. The latter study claims that there is a transition in scale height from the central B/P region to the outer bar region. The scale height is higher in central region compared to the outer bar region. Furthermore, it also claims the presence of two components in the bar; one is a thin component of scale height 180 pc whose density decreases outwards, another is a super-thin component with scale height of 45 pc whose density increases outwards along the bar. The modeling of the bar in this study corresponds to bar mass of 1.8 x 10^{10} M_{sun}.

Other recent studies (Portail et al., 2017) provide the modeling of the MW bar using red clump giants density from VVV, UKIDSS and 2MASS infrared surveys combined with stellar kinematics from the BRAVA and OGLE surveys, and ARGOS survey. This study claims that the bar pattern speed of the MW is equal to 39 ± 3.4 Km/s/kpc which places the corotation radius at 6.1 ± 0.5 kpc from the galactic center. The R parameter which is the ratio of corotation radius to bar length is equal to 1.22 ± 0.11; here bar length is taken as 5.0 ± 0.2 kpc (Wegg et al., 2015b). In this modeling bar mass turns out to be $1.3 \pm 0.1 \times 10^{10}$ M_{sun}. Figure 1.4 shows the best fitted model of bar from Portail et al. (2015).

Other studies are based on the chemodynamical modeling of bars (Portail et al., 2017) and use data from the Abundance and Radial Galactic Origins Surveys (ARGOS) (Freeman et al., 2013) and the Apache Point Observatory Galactic Evolution Experiment (APOGEE DR12) surveys. Freeman et al. (2013) gives an idea about how the MW bar formed and the bar structure. The study claims that the complex, bar orbital structure which results from bar formation and buckling, consists of metal rich stars that have a common origin which is the galaxy thin disk. Like many other barred galaxies, the MW also has a Boxy/Peanut shaped bulge in the central region (Blitz & Spergel, 1991; Weiland et al., 1994; Skrutskie et al., 2006). This B/P shape is also called an "X shape" (McWilliam & Zoccali, 2010; Nataf et al., 2010; Wegg & Gerhard, 2013).

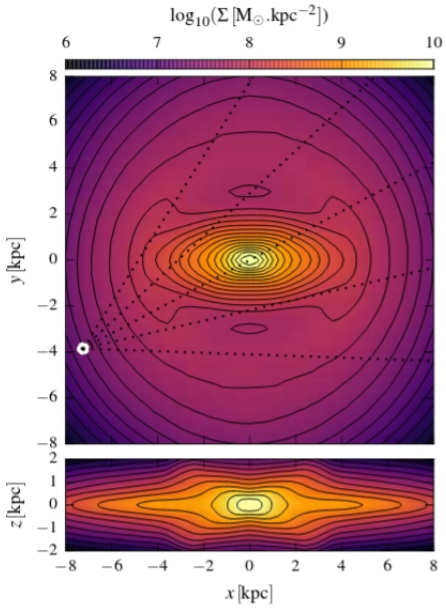

Fig. 1.4 Face on (upper panel) and edge-on(lower panel) view of Milky Way bar of best fitted model (M85) from Portail et al. (2015). The bar is 5 kpc long and it is at an angle of $\alpha = 28\,\mathrm{deg}$ from the line connecting sun to Galactic Center.

On-going and future spectroscopic surveys such as APOGEE, GAIA-ESO, GALAH and MOONS will provide stellar abundances of several elements, for more than 105 stars each. This will put even better constraints on the origin of stars.

1.3 Disk Dynamics

This section deals with the basics of equations governing the motion of stars in the disk galaxies. It contains the details about the motion of stars in the axisymmetric disk potential and the changes in stellar motion when non-axisymmetric perturbations are introduced. More details can be found in (Binney & Tremaine, 2008).

1.3.1 Stellar dynamics in the disks

All the calculations given here follow a fundamental assumption which is that individual interactions due to stars are neglected; instead a smooth stellar potential is adopted to determine the motion of stars. We derive the motion of stars in equatorial and meridional planes separately. All the quantities such momentum, energy and angular momentum are given in terms of per unit mass only.

1.3.1.1 Motion in equitorial plane

First let us calculate the motion of a star in a generalized gravitational potential and then discuss its motion in an axisymmetric potential. We know that for a centrally directed gravitational field the angular momentum (**L**) is a conversed quantity of motion. Therefore the motion of a star will be confined to an orbital plane. Let us calculate the motion of a star in polar coordinates (r, ϕ) where r=0 is center of attraction and ϕ is azimuthal angle in the plane of orbit. The langrangian for the particle is given as

$$\mathscr{L} = \frac{1}{2}[\dot{r}^2 + (r\dot{\phi})] - \Phi(r) \tag{1.1}$$

Here $\Phi(r)$ is the potential and is a function of radius only. So the equations of motion of a star particle are given as follows,

$$0 = \frac{d}{dt}\frac{d\mathscr{L}}{d\dot{r}} - \frac{d\mathscr{L}}{dr} = \ddot{r} - r\dot{\phi}^2 + \frac{d\Phi}{dr} \tag{1.2}$$

$$0 = \frac{d}{dt}\frac{d\mathscr{L}}{d\dot{\phi}} - \frac{d\mathscr{L}}{d\phi} = \frac{d(r\dot{\phi})^2}{dt} \tag{1.3}$$

Equation 1.3 implies that

$$r\dot{\phi} = constant = L \tag{1.4}$$

Let us proceed by using the above equation to replace time t by ϕ as an independent variable in equation 1.2.

$$\frac{d}{dt} = \frac{L}{r\phi}\frac{d}{d\phi} \tag{1.5}$$

Then equation 1.2 becomes

$$\frac{L^2}{r^2}\frac{d}{d\phi}(\frac{1}{r^2}\frac{dr}{d\phi}) - \frac{L^2}{r^3} = -\frac{d\Phi}{dr} \tag{1.6}$$

This equation is further simplified by putting $h = \frac{1}{r}$

$$\frac{d^2h}{d\phi^2} + h = \frac{1}{L^2h^2}\frac{d\Phi}{dh}(1/h) \tag{1.7}$$

There are two type of solutions for an equation of the above type; unbound orbits with r$\rightarrow\infty$ or h $\rightarrow$0, or bound orbit when r and h oscillate between minimum and maximum values.

Therefore each bound orbit is possible with periodic solutions of the above equation. To get further insights about the orbits we multiply the above equation with $\frac{dh}{d\phi}$ and integrate it with respect to ϕ.

$$\left(\frac{dh}{d\phi}\right)^2 + \frac{2\Phi}{L^2} + h^2 = constant = \frac{2E}{L^2} \tag{1.8}$$

Here E is constant and is the energy of the orbit. For bound orbits $dh/d\phi = 0$,

$$h^2 + \frac{2[\Phi(1/h) - E]}{L^2} = 0 \tag{1.9}$$

The above equation has generally two solutions, h_1 and h_2 around which the star oscillates as it rotates along ϕ. The inner radius $r_1 = h_1^{-1}$ is called the apocenter and the outer radius $r_2 = h_2^{-1}$ is called the pericenter. For circular orbits apocenter and pericenter are equal and the eccentricity of the orbit is zero.

Furthermore, T_r is twice the time a star takes to go from apocenter to pericenter, and $\Delta\phi$ is the increase in azimuthal angle as a star goes from apocenter to pericenter and comes back. The quantities T_r which corresponds time period of to radial oscillations and $\Delta\phi$ are calculated from 1.9 as

$$T_r = 2\int_{r_1}^{r_2} \frac{dr}{\sqrt{2[E - \Phi(r)] - L^2/r^2}} \tag{1.10}$$

$$\Delta\phi = 2L\int_{r_1}^{r_2} \frac{dr}{r^2\sqrt{2[E - \Phi(r)] - L^2/r^2}} \tag{1.11}$$

Then the azimuthal time period can be written as

$$T_\phi = \frac{2\pi}{|\Delta\phi|} T_r \tag{1.12}$$

In general $\Delta\phi/2\pi$ will not be a rational number, hence the orbit will not be closed or will have a rossette type of shape. The orbit is closed only for two types of potentials which are the spherical harmonic oscillator and the kepler potential. For disk like axisymmetric potentials the orbits will be rosette types as shown in Figure 1.5.

1.3.1.2 Motion in meridional plane

We use the cylindrical coordinate system (r,ϕ,z) for this calculation. We can study the 3D motion of a star particle in the meridional plane (2D) by using the property of conservation of angular momentum along the z direction (L_z). Let us assume that the potential $\Phi(r,z)$ is

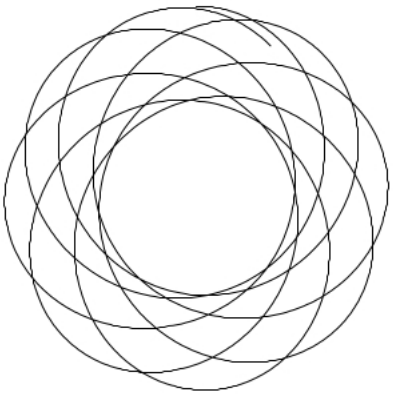

Fig. 1.5 A typical Rosette type orbits in axisymmetric potential which is similar to that in spherical potential.Courtesy: (Binney & Tremaine, 2008)

.

symmetric about the plane z=0. The lagrangian of the system can be given as,

$$\mathscr{L} = \frac{1}{2}[\dot{r}^2 + (r\dot{\phi})^2 + \dot{z}^2] - \Phi(r,z) \tag{1.13}$$

Then the generalized momentum of the system can be written as

$$p_r = \dot{r}; \qquad p_\phi = r^2\dot{\phi}; \qquad p_z = \dot{z} \tag{1.14}$$

Now the hamiltonian for the system can be written as

$$\mathscr{H} = \frac{1}{2}[p_r^2 + \frac{p_\phi^2}{r^2} + p_z^2] + \Phi(r,z) \tag{1.15}$$

$$\dot{p_r} = \ddot{r} = \frac{p_\phi}{r^3} - \frac{\partial\phi}{\partial r} \tag{1.16}$$

$$\dot{p_\phi} = \frac{d}{dt}(r^2\dot{\phi}) = 0 \tag{1.17}$$

$$\dot{p_z} = \ddot{z} = -\frac{\partial\Phi}{\partial z} \tag{1.18}$$

Equation 1.16 and 1.18 are the coupled equation of star in r and z axis while equation 1.17 represents conservation of angular momentum in z direction ($p_\phi = L_z$). After replacing L_z in

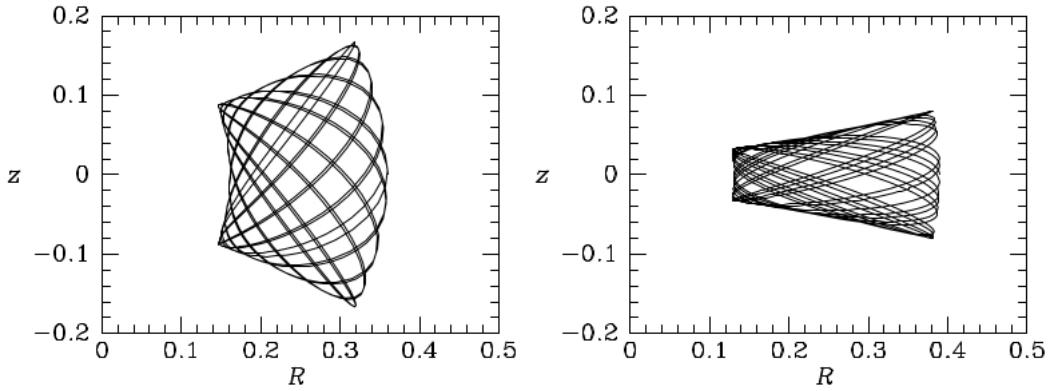

Fig. 1.6 Two orbits of star in potential given by 1.22 with q=0.9, $L_z = 0.2$, $v_o = 1$ and energy E=-0.8. Courtesy: Binney & Tremaine (2008).

equation 1.16 and 1.18 we get following equations

$$\ddot{r} = -\frac{\partial \Phi_{eff}}{\partial r}; \qquad \ddot{z} = -\frac{\partial \Phi_{eff}}{\partial z} \tag{1.19}$$

where Φ_{eff} is effective potential of the system and given as

$$\Phi_{eff} = \Phi(r,z) + \frac{L_z^2}{2R^2} \tag{1.20}$$

Now 3D motion of star is reduced to 2D motion with the following Hamiltonian

$$\mathscr{H}_{eff} = \frac{1}{2}(p_r^2 + p_z^2) + \Phi_{eff}(r,z) \tag{1.21}$$

The value of H_{eff} for an orbit is the total energy of the orbit (E). Since $\frac{1}{2}(p_r^2 + p_z^2)$ is the kinetic energy and is a positive quantity, therefore the motion of a star in the meridional plane is restricted to an area satisfying $E > \Phi(r,z)$ which is bound by a zero-velocity curve.

The typical motion of a star in the meridional plane is shown in Figure 1.6 for an example potential with $v_0 = 1$, $L_z = 0.2$ and q value of 0.9. The potential is given as

$$\Phi_{eff} = \frac{1}{2}v_o^2 ln(r^2 + \frac{z^2}{q^2}) + \frac{L_z^2}{2R^3} \tag{1.22}$$

Now the minimum of Φ_{eff} has a further significance.

$$0 = \frac{\partial \Phi_{eff}}{\partial z} \tag{1.23}$$

The above condition holds for orbits in the equatorial plane i.e. z=0 plane, about which the potential is symmetric. The following condition provides the information about the guiding centre R_g where

$$0 = \frac{\partial \Phi_{eff}}{\partial r} = \frac{\partial \Phi}{\partial r} - \frac{L_z^2}{R_g^3}; \qquad \left(\frac{\partial \Phi}{\partial r}\right)_{(R_g,0)} = \frac{L_z^2}{R_g^3} = R_g \dot{\phi}^2 \tag{1.24}$$

The above condition corresponds to a circular orbit with an orbital angular speed of $\dot{\phi}$ which we also call Ω_c. Hence, the minimum of Φ_{eff} occurs when the angular momentum of the orbit is L_z and this minimum value of Φ_{eff} is the energy (E) of circular orbit.

For eccentric orbits the angular speed Ω_ϕ is less than that of the angular speed required for circular orbits (Ω_c). The radial oscillations are anharmonic where $\Omega_r = 2\pi/T_r$ and T_r is the time period of radial oscillations. For a galaxy like potential $\Omega_\phi < \Omega_r < 2\Omega_\phi$ which means a star can make more than one but less than two radial oscillation during one orbital rotation. For near circular orbits Ω_ϕ becomes close to Ω_c and radial oscillations become harmonic around the guiding center which make Ω_r close to the epicyclic frequency κ which is then given by,

$$\kappa^2 = \left(\frac{\partial^2 \Phi}{\partial R^2}\right)_{R_g,0} + \frac{3}{R_g}\left(\frac{\partial \Phi}{\partial R}\right)_{R_g,0} \tag{1.25}$$

In the vertical direction, the oscillations have a period T_z. When the radial and vertical oscillations are small, they are decoupled and the angular frequency ν is given as

$$\nu^2(R_g) = \left(\frac{\partial^2 \Phi}{\partial z^2}\right)_{R_g,0} \tag{1.26}$$

Furthermore, for these small oscillations we have $\Omega_z = 2\pi/T_z$ and tends to ν.

In general, the motion of a star in a static axisymmetric potential can be decomposed into three independent oscillation directions, corresponding to Ω_r, Ω_ϕ and Ω_z. These type of orbits are called regular orbits. For regular orbits, in addition to two integrals of motion, E and L_z, there is a third non-classical integral of motion which can not be represented in any phase-space variable. There are some orbits for which these decompositions cannot be done, they are called irregular orbits. The other category of orbits are chaotic orbits.

1.3.2 Non-axisymmetric Perturbations and Resonances

The non-axisymmetric perturbation in $z = 0$ plane for a time varying potential can written in the following complex functional form $\mathbf{\Phi}$

$$\mathbf{\Phi}(\boldsymbol{r}, \boldsymbol{\phi}, \boldsymbol{t}) = \boldsymbol{A}(\boldsymbol{r}) exp^{i(m\phi - \omega t)} \tag{1.27}$$

where the complex function $\boldsymbol{A}(\boldsymbol{r})$ contains the information about the radial variation of amplitude and phase of the perturbation. Here m represents the m-fold symmetry of the potential i.e $m = 2$ corresponds to a bi-symmetric bar or a spiral perturbation. The $\mathscr{R}(\omega)/m$ is the pattern speed of the potential (Ω_p) and $\mathscr{I}(\omega)/m$ gives the exponent for the exponential variation of pattern speed (Sellwood, 2014) which basically tells about the angular speed of bar rotation and rate of change of angular speed of bar.

When orbit of a star is in resonance with a weakly perturbed potential which is rotating at an angular speed Ω_p, it can be expressed by the following relation.

$$\Omega_p = \Omega_\phi + \frac{l}{m}\kappa \tag{1.28}$$

where κ is the radial epicyclic frequency defined by equation 1.25 for near circular orbits, Ω_{phi} is the angular velocity of the star and l is an integer, which can positive or negative.

Corotation resonance occurs when the guiding center of a star rotates with the pattern speed of the potential i.e. $l = 0$.

$$\Omega_p = \Omega_\phi \tag{1.29}$$

Lindblad resonances occurs when a star encounters the maxima of the perturbed potential at a frequency equal to the radial frequency κ i.e $l = \pm 1$

$$m(\Omega_\phi - \Omega_p) = \pm\kappa \tag{1.30}$$

The positive sign in the above equation ($l = 1$) describes a star which rotates faster than the rotating potential and encounters its maxima at the resonant frequency κ; this is called the **inner lindblad resonance**. The negative sign ($l = -1$) corresponds to a star which rotates slower than rotating potential and maxima of potential crosses the star at resonant frequency κ. Resonances with higher values of $|l|$ are of lesser dynamical interests as they corresponds to radial ranges beyond the radii of Lindblad resonances.

Ultraharmonic resonances correspond to $|l| = 1$ when m is interchanged with 2m in equation 1.28. In this resonance, the star performs two radial oscillations as it crosses the successive maxima in the potential. These resonances are closer to corotation rather then

Lindblad resonances as the difference between angular speed and pattern speed is less for these orbits. Further higher order orbits are present in the disk when m is replaced with 3m or 4m. These resonances move closer to corotation radius as the difference between the stellar angular velocity and pattern speed reduces further. The ultraharmonic resonances are not important in linear perturbation theory but important for non-linear analysis. So these resonances are important for bar studies in disk galaxies.

Vertical resonances in the disk are given by the following equation.

$$m(\Omega_\phi - \Omega_p) = n\nu \tag{1.31}$$

where ν is the vertical epicyclic frequency as given in equation 1.26. Here n is a signed integer. The value $n = 0$ corresponds to vertical coroation which does not have much significance. $n = \pm 1$ corresponds to vertical resonances. As ν is much larger compared to κ therefore vertical resonances lie outside the Lindblad resonance ranges. Therefore, these resonances are of lesser importance for linear perturbation theory but important for non-linear theory. They play an important role in the evolution of bar type instabilities in the disk which we will discuss later. Stars can be trapped by the resonances and this increases the size of the trapped region in phase-space; this also increases as the perturbing potential grows.

1.3.3 Local stability

The global normal modes of stellar disks are hard to calculate as the computation of the perturbed potential is not an easy task (Kalnajs, 1977; Jalali, 2007; Binney & Tremaine, 2008). The WKB approach provides a tool where local spatial disturbances can be replaced by a plane wave and some insight about the global modes can be deduced. Toomre (1964) used this approach to give an idea about scales which can be stabilized in a razor thin disk with surface density Σ that has axisymmetric oscillations. The scales which are stable should be larger than a critical value given by

$$\lambda > \lambda_{crit} = \frac{4\pi^2 G\Sigma}{\kappa^2} \tag{1.32}$$

here κ is the radial epicyclic frequency given by equation 1.25. The λ_{crit} is infinite in the complete absence of random motion in the disk, which means that all scales which are obviously smaller than λ_{crit} will be unstable to gravitational clumping. As the random motion or κ increases the value of λ_{crit} decreases which can be thought as stars being held rigidly in the disk but rotating about the guiding center. The value of λ_{crit} in our Galaxy, close to the sun is 6 kpc which is quite large given that the distance of the sun from the Galactic center is 8kpc. It points out the limited extrapolation of the WKB approximation. The random motion in the

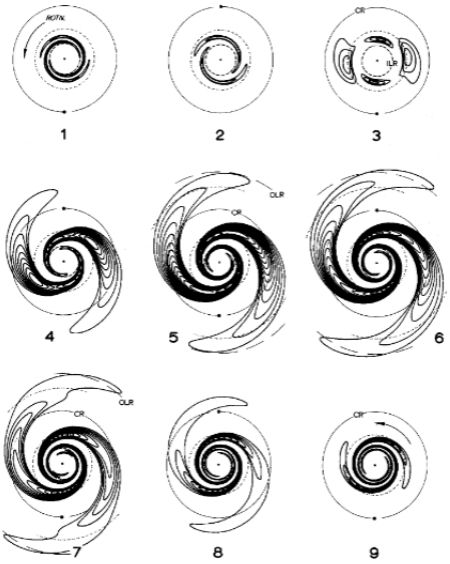

Fig. 1.7 This Figure shows an input leading wave packet in half-mass Mestel disk which evolves with time. Time units are given in terms of half the orbital time at corotation radius.ILR, CR and OLR denotes the radius of inner lindblad resonance, corotation radius and outer lindblad resonance. Courtest: Toomre (1981a)

disk provides stability to the disk at small scales while the disk rotation stabilizes it on larger scales. Toomre also put this stability condition into a criterion which has been widely used in the literature. This Toomre's instability criterion is as follows : if a stellar disk has gaussian distribution of it's radial velocity dispersion σ_r then the disk is locally stable if

$$Q = \frac{\sigma_r}{\sigma_{r,crit}} > 1, \qquad \sigma_{r,crit} = \frac{3.36G\Sigma}{\kappa} \tag{1.33}$$

For solar neighbourhood parameteres, σ_{crit} is close to 20 kms^{-1}. The above criterion for a razor-thin gas disk follows as

$$Q = \frac{c_s \kappa}{\pi G \Sigma} \tag{1.34}$$

where c_s is the sound speed in the fluid. The constant value in the denominater decreases as the disk thickness increases, which means the disk thickness provides extra stability to the disk(Romeo, 1992). Further the study of local stability for disk with both gas and stellar component has been seen here Rafikov (2001) and a formulation similar to Toomres criterion has been computed by Romeo & Wiegert (2011). The disk which is locally stable i.e. satisfies the local stability criterion given by 1.33 is not guaranteed to being stable against large scale non-axisymmetric modes of instability. The general formulation of disk stability against non-axisymmetric modes is yet to be developed.

Local non-axisymmetric stability analysis was performed by Goldreich & Lynden-Bell (1965) and Julian & Toomre (1966). In these independent studies the idea of swing amplification was conceptualized. Toomre (1981a) calculated the global evolution of disk swing amplification by introducing a leading spiral mode within the ILR region of disk as shown in Figure 1.7. The disk is linearly stable as $Q > 1.5$, and the input mode expands or unwinds due to differential rotation of the disk until it swings back from leading to trailing mode. The input wave mode is amplified at corotation by a large amount during this period when the mode is wound by small amount. The wave propagates with a group velocity which returns back to the ILR as a trailing wave from corotation and then transmits from corotation as a leading wave. The waves which are going out of corotation fade away in a wider area while waves coming back into the central region are absorbed by the ILR. The second order effect of this phenomena causes significant changes in the disk compared to first order effects.

The amplification of waves at corotation has been calculated using various approximations (Drury, 1980; Toomre, 1981a). For this purpose, one of the most important parameters which is given by Julian & Toomre (1966).

$$X = \frac{\lambda_y}{\lambda_{crit}} = \frac{2\pi R_{CR}}{m} \frac{\kappa^2}{4\pi^2 G\Sigma} \tag{1.35}$$

where λ_y is the wavelength of the disturbance with m-fold symmetry around the corotation radius R_{CR}. For a flat rotation curve where $1 \leq X \leq 3$, the amplification is significant. As the rotation curve rises, the range of X values for the amplification to occur decreases while it increases for a decreasing rotation curve. When there is no differential rotation the value of X tends to zero for strong amplification.

As the Toomre factor Q (1.33) increases, the value of the amplification factor decreases for the same X parameter. For example, a wave mode can be amplified after being reflected a hundred times for $Q \approx 1.2$ and $X \approx 2$ which is merely a few time for $Q \approx 2$.

1.4 Bar Formation Mechanism in disks

The formation of bars in disk galaxies is a complex process and there is very little known analytically about the mechanism of forming a strong bar. In this section we discuss the previous studies which explored the bar formation mechanisms both with N-body simulations and analytical approaches.

1.4.1 Global Bar forming modes

N-body simulations (Hohl, 1971; Ostriker & Peebles, 1973) and global stability studies (Kalnajs, 1972, 1978; Jalali, 2007) have shown that rotationally supported disks are unstable to global modes. In the linear regime, the disks are unstable to 2 arm spiral modes which after saturation lead to bars in inner disk and dispersing spiral in the outer part of the disk. This causes an exchange in the angular momentum between the inner part and outer parts of the disk. It results in increasing the stellar mass in the inner part of the disk as well as spreading the mass over the outer parts of the disk (Hohl, 1971). The non-linear bar formation process by the instability is understood to be caused by a standing wave. Inner rotation curves must be rising linearly for the instability to grow which is provided by a quasi-harmonic potential generated by the combined mass distribution of disk, bulge and dark matter halos within the core radius R_{core} of the galaxy. Figure 1.7 shows that group velocity of leading waves approached towards co-rotation while that of trailing wave approaching towards the center. The incoming trailing wave can be absorbed at the ILR while it can also transmitted to the central region given the potential is quasi-harmonic. In this case the potential is quasi-harmonic in the central region, therefore the $m = 2$ mode trailing wave does not get absorbed at the ILR rather it transmits through the centre and comes out as a leading wave. The leading wave which is reflected from the co-rotation is amplified as a trailing wave moving inwards. Further a trailing wave is also generated which moves outwards as a result of wave action conservation. The unstable modes are amplified at co-rotation and happens at orbital timescales of stars at co-rotation radius. The bar sizes generated by these global modes are $20-30\%$ of the core radius R_{core}.

1.4.1.1 Stabilizing Mechanisms

Swing amplification along with the presence of a positive feedback loop allows the global modes to amplify in a massive disk with low velocity dispersion. These amplifications are highly sensitive to the value of Q. The strong amplification of $m = 2$ modes occurs when a massive disk is centrally concentrated and has a stability parameter of $1 \leq X \leq 3$ and $Q < 2$.

The disk with a central quasi-harmonic potential supports the $m = 2$ mode to grow by a feedback mechanism which allow the trailing wave to pass through the center and generate a leading outgoing wave. This feedback mechanism can be stopped by either introducing large amount of random motion in the disk (Athanassoula & Sellwood, 1986). It can also be done by making the disk stable against the $m = 2$ mode by increasing the value of the stability parameters i.e $X \geq 3$. This has been studied in the literature (Ostriker & Peebles, 1973; Efstathiou et al., 1982; Christodoulou et al., 1995) by introducing a centrally concentrated rigid halo component which can be either a bulge or a dark matter halo. On the other hand rotating

and interacting halo components allow bars to grow faster (Saha & Naab, 2013). Apart from these processes, there are other mechanisms which can stabilize the disk. Toomre (1981a) has pointed out that if the reflected trailing wave does not get reflected from centre, it will stop the feedback mechanism and as a result prohibit the formation of bar instability. This can be achieved easily by the introducing an ILR in the disk which will absorb incoming trailing waves. The stability against bar mode has been demonstrated in numerical simulations by introducing a high central mass concentration which allows ILR at any pattern speed. The disks used in the above experiments have realistic rotation curves and medium values of velocity dispersion.

1.4.2 Bar Formation through Nonlinear Trapping

Efstathiou et al. (1982) found that bars formed in the their galaxy disks irrespective of the presence of a central mass concentration or bulge which contradicts Toomres' prediction. This effect was further explored by (Sellwood, 1989) who also showed that the introduction of centrally dense bulges allowed the bar to form in disks with initial random distribution of particles. He had further shown that the bar is not allowed to form if the particles are distributed uniformly on the ring which reduces the initial shot noise to low order harmonics, also called a quiet start. The reason for different outcomes in the two cases is due to absorption of trailing spiral wave at ILR and happens only for small amplitude disturbances. The shot noise in the distribution of particles produces high amplitude disturbances which cannot be absorbed by the ILR. This results in non-linear trapping of orbits which is similar to global mode amplification. The other natural way to reduce the shot noise is to use larger number of disk particles which was not the case in Efstathiou et al. (1982). Thus earlier criteria like bulge or halo mass required to prohibit the bar instability (Ostriker & Peebles, 1973; Efstathiou et al., 1982; Christodoulou et al., 1995) can be simply used for centrally concentrated disks or high resolution simulations with similar scenarios.

The shot noise in real galaxies is very small as real galaxies have approximately 10^{10} stars. Apart from this disk perturbations can be due to star clusters and Giant Molecular Clouds (GMCs) but these are not thought form non-linear bars. However, large perturbations due to the merger/interaction of a satellite can result in non-linear bar type instability.

1.4.3 Slow Trapping of Orbits

The pioneering work by Lynden-Bell (1979) has shown a method which allows the secular growth of bars in galaxies. In this work it has been shown that eccentric orbits under certain paradigm, get trapped into the slowing rotating bar structure. Furthermore, he has shown that the angular momentum from the inner part of the galaxy will be transferred to the outer part and

carried away by the spiral arm which has also been shown in simulations (James & Sellwood, 1978). Further work by Polyachenko (2004, 2013) have shown that this slow trapping of orbits can lead to the formation of a slow bar. Further studies explained the weak and slow nature of bars in the simulated models Athanassoula & Sellwood (1986) by this mechanism. The velocity distribution in these models was radially biased. A similar mechanism is also shown to be the origin of bars (Palmer et al., 1990) where the velocity dispersion is radially biased.

1.4.4 Bar Formation through mergers or tidal interaction

There are many studies in the literature (Byrd et al., 1986; Noguchi, 1987; Gerin et al., 1990; Salo, 1991; Mayer & Wadsley, 2004; Romano-Díaz et al., 2008) which show that bars can be triggered by encounters with satellites. This can also happen through nonlinear trapping of orbit if the unperturbed disk is stable. Miwa & Noguchi (1998) have shown that bars generated by tidal encounters are slower or $\mathscr{R} >> 1$ compared to global mode and other formation scenarios. Cosmological simulations (Curir et al., 2006) also show that bars are formed in cosmological halos which have moving substructures within it. The presence of gas does not support bar formation in encounters as similar models with gas free components show bar formation (Berentzen et al., 2007). The conclusion of this study maybe limited by the high viscosity in the Smooth Particle Hydrodynamics(SPH) method. The encounters of galaxies (including gas) has not been fully explored given the range of parameters such mass ratios, orbits, spin directions and gas mass fractions.

There are numerous studies which look for whether the presence of bars in galaxies is associated with the presence of a companion or due to crowded environments (e.g. galaxy groups). Despite the large number of studies, the results are inconclusive. These studies have been reviewed by Skibba et al. (2012) which finds the there are a significant number of bars in galaxies with companions at moderate distances. To determine the real significance of interactions for bar formation requires much more elaborate theoretical and observational studies (Menéndez-Delmestre et al., 2007).

1.5 Orbits in bar

A self-consistent bar is a non-linear structure which is mostly visualized in the bar rotating frame. It has been seen that most of the orbits in a bar moves ahead in the rotating frame which implies that the period of these stars are much lower than the rotating pattern. A detailed analysis of orbits in the bar is given by (Sellwood & Wilkinson, 1993). Here we give brief detail about the most important orbits which are present in the bar.

Bars have several periodic orbits along with trapped orbits around it which is called the resonant family of orbits. The stars in these bar orbit occupy most of the phase-space. The typical orbits in the rotating bar frame is shown in Figure 1.8. The effective potential of the bar is given by (Binney & Tremaine, 2008)

$$\Phi_{eff} = \frac{1}{2}v_o^2 ln\left(1+\frac{x^2+y^2/q}{R_c^2}\right) - \frac{1}{2}\Omega_p^2 R^2 \tag{1.36}$$

where $q \leq 1$ is flattening parameter, $R^2 = x^2+y^2$, R_c is core radius below which the potential is close to harmonic and v_o is the rotation speed at large R when q=1. Periodic orbits are the resonant orbits which close in bar rotating frames, the solid line in Fig. 1.8 shows 2:1 orbits which close after two radial oscillations when a star completes one circular rotation about the galactic center. These periodic orbits which are aligned along the bar are called x_1 orbits. There is a transition energy around which x_1 orbit show peculiar changes in their shape. These x_1 orbits are elongated and lens shaped on low energy side this transition energy while these orbits are self intersecting on the high energy side of transition energy. Figure 1.9 shows two of the non-closed orbits in the family of x_1 orbits which are doing fundamental oscillations about the periodic stable orbits. The x_1 family of orbits have the major contribution to the bar structure (Contopoulos, 1980) because the stars trapped around these orbits have a density distribution more elongated than the bar potential. As the poisson's equation requires the potential to be more circular compared to the density distribution therefore a self consistent bar must be confined to smaller region than that is available for them given the energy ranges. This further requires bars to have more regular orbits compared to chaotic orbits which fill most of the volume by their given energy.

Figure 1.10 shows that there are five Lagrange points in a bar potential given by equation 1.36 where stars can be stationary in the rotating frame of the bar. Here the Lagrange point L_3 lies on the bar center while the other four Lagrange points lie on the corotation radius. Out of these four L_1 and L_2 do lie along the bar major axis and another two points L_4 and L_5 lie along the bar minor axis. Theoretically it has been seen that self-consistent bars cannot exceed the Lagrange points along the bar axis. The reason is that bar potentials which is extended beyond the corotation causes stellar response to be elongated along the orthogonal direction of bar. Further, overlapping of resonances (Chirikov, 1979) and the increase in density of resonances specially ultra-harmonic orbits (Contopoulos & Papayannopoulos, 1980) strengthen the argument for bar being within the corotation radius. Elmegreen et al. (1996) defined a new parameter to measure dynamical properties of bars which is given as

$$\mathscr{R} = R_L/R_b \tag{1.37}$$

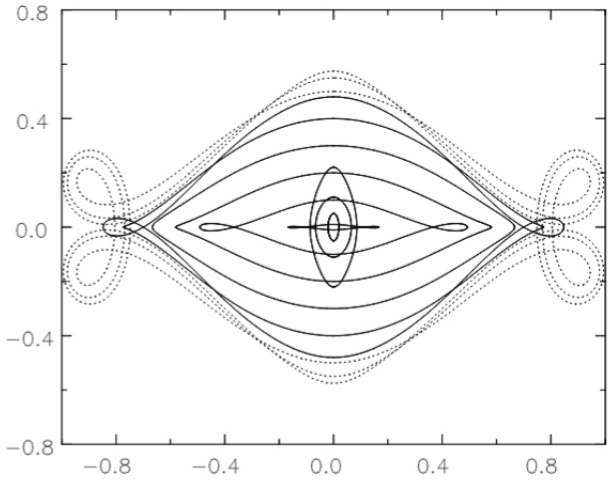

Fig. 1.8 The solid line shows 2:1 orbits which corresponds to two radial radius of star for every circular rotation around galactic center. The family of orbits which are elongated along bar are called x_1 orbits while the orbits which are elongated perpendicular to the bar are called x_2 orbits. The dotted line orbits are 4:1 which closes after 4 radial oscillation for a single circular rotation. These closed periodic orbits are shown in bar rotating frame. Courtesy: Sellwood (2014)

.

where R_L is the distance of the Lagrange point from the galactic center which is close to the corotation radius and R_b is half the bar length or distance of semi-major axis from galactic centre. A bar is called fast if $\mathscr{R}$ <1.4 and slow when $\mathscr{R}$ >1.4. Theoretical bar formation models and observational studies claim that most of the bars are fast with very few being slower (Aguerri et al., 2015).

There are other 2:1 orbits which are called x_2 orbits. As shown in Figure1.8 these x_2 are found in the very inner region of bar and they are elongated in the direction which is orthogonal to bar axis. x_2 orbits go to stable family while their unstable counterpart is called x_3 orbits (Contopoulos & Papayannopoulos, 1980). These x_2 orbits are generally found in the dense core where the orbital period is small. The existence of an ILR in the potential for a given mass distribution is necessary but does not guarantee the presence of x_2 orbits. The influence of resonances can identified from orbit structure but it is difficult to determine location or radius of x_2 orbits in the strong bar as some of the elongated x_1 orbits along the bar overlap the x_2 orbits in the central region.

The edge-on view of bars have a boxy appearance (Kormendy, 1983; Athanassoula et al., 1990; Gadotti, 2011) which indicates the presence of rectangular shape orbits. The dotted lines in Figure 1.8 show the 4:1 orbits which are elongated along bar major axis and can be linked

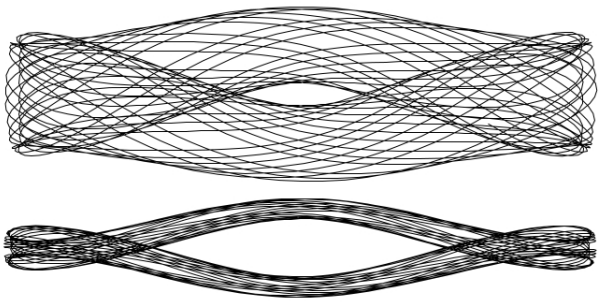

Fig. 1.9 Non closed orbits from the family of x_1 orbits.(Courtesy: Binney & Tremaine (2008))

with the presence of a box shape in the edge-on view of the bar. In these orbits, a star performs 4 radial oscillation for every circular rotation around the galactic centre. Furthermore, these orbits are found near co-rotation radius where the period of the orbit is large enough such that it can accommodate 4 radial oscillation within one circular rotation of star around galactic centre. Therefore these orbits are mostly found in fast bars.

The 2:1 and 4:1 orbits families are the most important in the bar when the motion is confined to a plane though there are many other less important families of orbits. The orbits in three dimensional bars do have multiple possible commensurabilities between in-plane oscillations and vertical oscillation frequencies. Despite many possibilities the families of orbits which have projection similar to x_1 remains the most important family of orbits. Another important family is that which show arc like structure when seen from side view. This is called 2:2:1 orbit family in which the star oscillates twice in the radial as well as vertical direction when it revolves once around the galactic center. Figure 1.11 shows the 3 projection and tube views of these family of orbits.

1.6 Buckling Instability

Once the bar has formed, it evolves and generates other kind of instability which causes it to appear like a peanut shape as it thickens out of plane (Combes & Sanders, 1981). Combes et al. (1990) and Pfenniger & Friedli (1991) have shown that thickening of bars can occur due to vertical resonances and simulations of disks show that buckling is suppressed when the potential is forced to be symmetric due to thickening along the vertical axis about the mid plane of the galaxy. Although Pfenniger et al. (1994) argue that thickening is more pronounced when the buckling is allowed. There are several simulations (Raha et al., 1991; O'Neill & Dubinski, 2003; Martinez-Valpuesta & Shlosman, 2004; Martinez-Valpuesta et al., 2006) which shows that the bending of bars as seen from an edge-on view, is the main reason behind the peanut

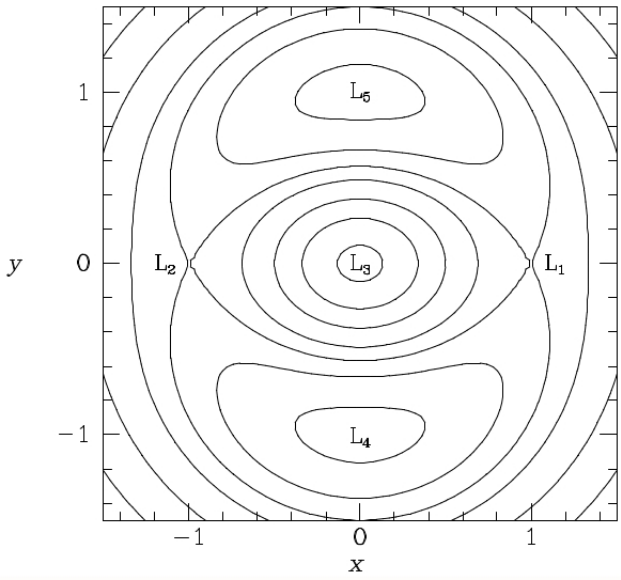

Fig. 1.10 Contours of constant effective potential (Φ_{eff}) given by equation 1.36 for parameters v_o=1, $q = 0.8$, $R_c = 0.1$ and $\Omega_p = 1$. The point L_3 is the minima of Φ_{eff} and L_3, L_5 are the maxima. While L_1 and L_2 are the saddle points. Courtesy: Binney & Tremaine (2008)

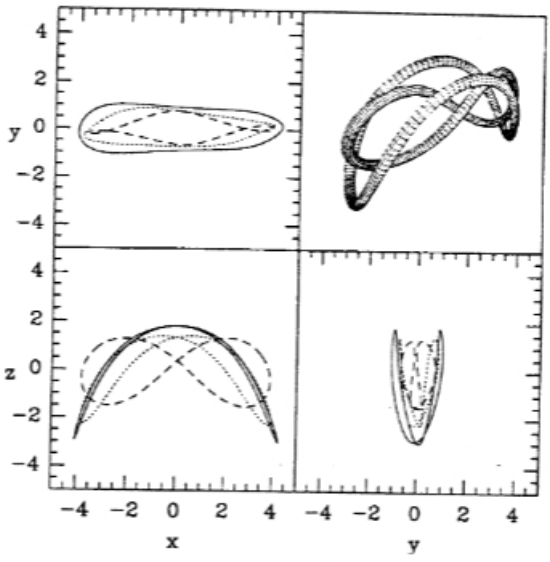

Fig. 1.11 Three orthogonal projection and one tube view of 3D shapes of 2:2:1 orbits. The solid line corresponds to symmetric orbits, dashed line presents anti-symmetric orbits and dotted line show the intermediate cases. Courtesy: (Pfenniger & Friedli, 1991).

shapes of bars. The peanut shape of the Milky Way bulge has been also explained to be formed by buckling instabily of bar (Shen et al., 2010; Gerhard & Martinez-Valpuesta, 2012; Li & Shen, 2012) which is backed by kinematic observations Vásquez et al. (2013).

The stellar systems which are excessively flattened tend to show buckling instability (Julian & Toomre, 1966; Kulsrud et al., 1971; Fridman & Poliachenko, 1984). The uniform stellar sheet with vertical $sech^2(z/z_0)$ profile having $\sigma_z < 0.3\sigma_x$ generates buckling instability which agrees with global axisymmetric models (Sellwood, 1996). When the nonlinear evolution of a flattened bar like stellar system does not allow the self-gravity of the system to confine the star particles in the bending layer, then the system becomes thick in the vertical direction with smaller vertical anisotropy as shown for prolate systems (Merritt & Hernquist, 1991) and disks (Sellwood & Merritt, 1994).

Buckling instability is clearly explained by the presence of 2:2:1 resonant orbit families in the bar (Pfenniger & Friedli, 1991). Further work also shows that 3D bars have mainly 2:2:1 resonant orbit families (Pfenniger & Friedli, 1991; Martinez-Valpuesta et al., 2006) in the rotating frame of the bar which corresponds to two radial oscillation and two vertical oscillations. Here the amplitude of vertical oscillations increases with distance from the center.

As the buckling instability causes the transfer of horizontal energy to the vertical direction, it makes bars weaker and centrally concentrated (Raha et al., 1991; Debattista et al., 2004; Martinez-Valpuesta & Shlosman, 2004; Debattista et al., 2006). The peanut shape of bar after buckling depends on the central concentration in the disk, for quasi-uniform inner density the bar will have pronounced peanut shape while it will be uniform for disk having high central concentrated (Berentzen et al., 2007).

Athanassoula & Misiriotis (2002) show that as the bar length grows the peanut shape becomes more significant. (Martinez-Valpuesta et al., 2006) show that lengthy bars can show buckling twice during their evolution.

1.7 Renaissance of a bar ?

As we know that bar type global instability results in largest mass and angular momentum redistribution in the disk (Debattista et al., 2006)). The bar type global instability is thought to occur once in the lifetime of a galaxy. Bournaud & Combes (2002) and Combes (2008) show that in their simulations bar can recur. The bar formation and dissolution of bar leaves disk with high random motion of star or hotter component which make disk unlikely to have bar instability again. Though the incoming gas which settle in circular orbits and form stars, have lesser random motion which is prone to bar type instability. Therefore in their work (Bournaud & Combes, 2002) high accretion rate of gas is considered to check recur of bar. They find few

of their model generates bar second time where disk become double the size of initial disk given the high accretion rate.

However, it is really difficult to find such phenomena where a lot of gas mass is added to hotter disk component. Apart from this first bar formation will cause angular momentum transport which will increase central concentration of disk making disk stable against bar instabilities (Sellwood & Moore, 1999).

1.8 Effect of CMC

Ostriker & Peebles (1973) have shown that the presence of massive halo surrounding a disk makes disks hot enough to be stable against bar type of instabilities. Furthermore, Sellwood (1980) have shown that the presence of a massive rigid bulge in the center of galaxy does not allow bar instabilities. The effect of the bulge becomes prominent with the concentration of the bulge. A physical picture of effect of the massive central concentration is discussed by Toomre (1981a). He has shown that the presence of massive bulge introduces an ILR in the disk which further cuts the feedback loop for swing amplification to work. Swing amplification (Toomre, 1981a) is thought to play an important role in formation of bar type instability, it can be nullified by the presence of central concentration.

The effect of imposed central mass concentration has been looked in the previous studies Norman et al. (1996); Shen & Sellwood (2004); Athanassoula et al. (2005); Debattista et al. (2006) which claim that the bar gets weaker with the increasing central mass concentration until these mass is few percentage of the disk mass. Massive compact CMC (Shen & Sellwood, 2004) has been seen to dissolve the bar as it makes large phase space region to be chaotic while the lower mass CMC makes a bar weak by producing small phase space region to be chaotic. As the CMC mass increases it makes eccentric bar orbits to deviate from the bar and causes enhanced random motion (Das et al., 2003, 2008). Finally as the bar dissolves it leaves disk kinematically hotter.

As we see above that central spherical mass in the disk play an important role in determining the stability of the disk against bar type instability. In this thesis we explore and quantify the effect of central bulges on the bar formation in the disk.

1.9 Bar Halo Friction

The bar is thought to experience friction from the spherical component in the galaxy (Sellwood, 1980; Weinberg, 1985). As a result of this friction due to the halo, a bar grows in length and

strength. Weinberg & Katz (2007b) explained that only a small number of resonances especially ILR, out of existing many resonances between bar and halo orbits, contribute to frictional drag.

The frictional drag force varies with the angle between bar major axis and halo response due to bar (Debattista & Sellwood, 2000; Sellwood, 2006). In the beginning of bar evolution when the angular speed of bar is large, the frictional drag due to the bar is small as the halo response is almost perpendicular to the axis of bar. The drag increases as this angle reduces and reaches a maximum value around 45°. The frictional drag becomes almost negligible when the halo response aligns with the bar which happen as bar completely stops. When halo response or halo bar align with bar major axis align, galaxy reaches the steady state (Athanassoula, 2007).

It has been shown that frictional drag due to the halo on bar varies with the degree and sense of halo rotation (Debattista et al., 2006). The friction due to the halo is similar, with a mildly rotating halo having the same sense of rotation as a disk. This frictional drag decreases significantly if the halo rotation is unrealistically high. As a result of dynamical friction due to the halo, a bar slows down and increases its length. If the halos are highly concentrated (Athanassoula & Misiriotis, 2002; Athanassoula, 2003; Martinez-Valpuesta et al., 2006), the bar can increase its size to the extent of disk which makes the co-rotation lie outside of the disk. Thus, the unrealistically large bars suggest the absence of dense dark matter halo in most of the galaxies.

The spherical component which provides the frictional drag to bar and absorbs angular momentum from the bar can also be the central spheroidal component (Saha et al., 2012). It has been shown that initially non-rotating classical bulge can significantly gain angular momentum from the bar and corotate with bar. In this thesis we further explore the angular momentum transfer from the bar to these spheroidal components.

1.10 Bar Pattern Speed

Tremaine & Weinberg (1984b) proposed a technique to measure the pattern speed of bar by measuring kinematics of stellar population. This technique uses the continuity equation and assumes a single pattern speed in the stellar disk. If there are multiple pattern speeds in the disk, this technique may lead to misleading predictions of pattern speeds as the disk has pattern speeds with multiple frequencies. This technique is suitable for early type disk galaxies as the stellar population in the early type disk follows the continuity equation and has less dust obscuration as well as little star formation. The pattern speeds of early-type galaxies have been compiled by Corsini (2008) and they have found have mostly fast bars as $1 < \mathscr{R} < 1.4$.

The method of Tremaine and Weinberg has been applied to ionized gas (Fathi et al., 2009) and molecular gas (Meidt et al., 2009) though these components do not obey continuity

equation. The measurements indicate fast bars from ionized gas study (Fathi et al., 2009) while the molecular gas study (Meidt et al., 2008) claims radial variation of pattern speed. Furthermore, Meidt et al. (2009) claim that pattern is higher in the central regions of galaxies compared to that in the outer regions.

There have been several other methods to measure the bar pattern speeds in disk galaxies, such as the gas flow patterns in bars. The studies with this method (Lindblad et al., 1996; Weiner et al., 2001; Pérez et al., 2004; Zánmar Sánchez et al., 2008) finds fast bars in all the cases as $\mathscr{R} \approx 1.2$. Also, Athanassoula (1992) claimed that shapes and locations of dust lane in the bar suggests $\mathscr{R} \approx 1.2$. This is supported by the presence of 4:1 orbits in the bar, as fast bar are more likely to possess these orbits. Furthermore Buta & Combes (1996) use the presence of rings in the disk to measure the location of major resonance with a bar as a kinematic indicator of pattern speed.

Recent measurements of bar pattern speeds by Rautiainen et al. (2008) claims bar pattern speed depend on the morphological class of galaxy while Aguerri et al. (2015) claims that bar pattern speed does vary along the hubble sequence. In this thesis we explore the bar pattern speed in the models with the increasing bulge masses covering galaxies all over the hubble sequence.

1.11 Thesis Plan

We discuss the plan of thesis in this section. We know that there is no analytical theory which explains strong bars. These bar type of instabilities are mainly studied with N-body/SPH simulations. In this thesis, we have conducted most of our study with the help of numerical simulations. So we dedicate chapter 2 to discuss the details of numerical methods used in this study.

As we have seen in section 1.8 that central mass concentration play an important role in bar formation and it's evolution. In this thesis we first explore how the central concentration affects the bar formation and it's evolution. We look for the effect of both mass and concentration of the central bulge on the bar instability. We discuss the impact of bulges on bar formation in Chapter 3. Further, we also test our predictions with the galaxies with varying range of central masses in Chapter 4.

After we have looked the effect of central concentration on bar formation we look at the effect of bulge mass on the pattern speed of the bars. As we have seen that a spherical component provide a friction to bar in section 1.9 we explore this in detail. In this part we also explore the slowness/fastness of bar as we increase central bulge mass. We discuss the effect of bulges on pattern speeds in Chapter 5.

In the end of the thesis we explore how the presence of bars in the disk can alter the cuspy dark matter halo profile along the line of core-cusp problem of LCDM cosmological model. We also explore if the resolution of the simulation affects this result. We discuss the effect of bars on dark matter profiles in Chapter 6.

Finally, we conclude the thesis along with future directions in Chapter 7.

Science is a way of thinking much more than it is a body of knowledge.

Carl Sagan

2

Numerical Techniques Used

As mentioned in the earlier chapter, bars are a very complex phenomena in disk galaxies which are mainly studied with numerical simulations. In this chapter, we discuss the numerical methods and techniques used to study bar instability in the disk galaxies. We have used N-body simulations to study the disk stability and our methods are described in this chapter.

2.1 Initial N-body models for disk galaxies

In order to study the disk instability we aim to generate equilibrium N-body models of disk galaxies. For this purpose we have explored several publicly available codes which includes ZENO (Barnes, 2011), NEMO (Teuben, 1995), and GALIC (Yurin & Springel, 2014). We were able to generate disk galaxy models which contains disk, bulge and halo components. We proceeded with the GALIC code as it produces equilibrium models with a control on the density distribution of each component in the galaxy. GalIC uses mainly the Schwarzschild method of iterating the particle orbits until the target density distribution of each component in the galaxy is reached. GALIC is a parallelized code which further reduces the time of initial model generation as the method require several iterations to reach target density distributions. This code does not include the gas component in the disk. We have introduced gas component to test

its effect in bar formation, but we have not included it in the thesis. For generating gas particles, we converted a fraction of star particles into gas particles (Smooth particle hydrodynamics) by converting the mean random motion of stellar particles to gas thermal energy and mean stellar streaming velocity of disk particles to circular velocities.

2.2 Code used for Evolving Galaxy

After we generated the initial N-body galaxy models, we wanted to observe its isolated evolution along with time. We have used a publicly available code Gadget-2 (Springel, 2005) for evolving the galaxy models.This code is efficiently parallelized which reduces the force computation time by dividing the work load among several processors. This way we can use a large number of particles in the simulations to compute gravitational forces in optimal time. The code computes gravitational forces using the hierarchical tree algorithm (Barnes & Hut, 1986). We have not included the gas component in the study conducted during thesis work so we don't use SPH technique available in the code. In the next subsection we briefly summarise the N-body method and time integration techniques used in this code.

2.2.1 N-body Method

In the N-body method, the star and dark matter particles are evolved from initially defined position ($\vec{r}$) and velocity ($\vec{v}$) distributions of all N particles under mutual gravitational interaction forces. The initial distribution of all the N particles correspond has to be defined at each step. We know that galaxy systems are collisionless as the collisional relaxation time is much higher compared to the age of the universe. The equation which evolves the initial positions and velocities of particles under their mutual gravity, is given by

$$a_i = -\sum \frac{G m_j |\vec{r}_i - \vec{r}_j|}{|\vec{r}_i - \vec{r}_j|^3} \tag{2.1}$$

where a_i is the acceleration of i^{th} particle from all the surrounding j particles with each particle having mass m_j. All particles satisfy this equation which results in N coupled and nonlinear second order differential equations. For N>2, the solution can only be obtained by numerical integration of these equations. These equations possess numerical singularity when $|\vec{r}_i - \vec{r}_j| \to 0$. As the particles approach each other and have a close spatial encounter, the time step of evolution of the particles is decreased for maintaining the force calculation accuracy which enhances the computation time by large amount. Constant timing can be used in the cases of close encounters but it can lead to large errors in determining the trajectory of particles

and un-physical solutions to the equations of motion. Since we know that galaxy systems are collisionless these close encounters are avoided in numerical simulations by introducing a softening parameter (ε) in the denominator of equation 2.1. Now the new equation of motion becomes

$$a_i = -\sum \frac{Gm_j|\vec{r}_i - \vec{r}_j|}{(|\vec{r}_i - \vec{r}_j|^2 + \varepsilon^2)^{3/2}} \tag{2.2}$$

The softening parameter is chosen on the basis of simulation type, though generally it is taken to be the mean inter-particle separation. This softening parameter decides the resolution of the simulation. Therefore, if softening is ε then a scale less than ε cannot be used to predict the results. In order to ensure the force calculation at large scale is not affected by this small scale modification parameter ε, a smoothening kernel is defined which ensures forces are Newtonian at small scales of the order of ε. GAGDET-2 uses a spline kernel (Monaghan & Lattanzio, 1985) $W(r, h = 2.8\varepsilon)$ which has the following form.

$$W(r,h) = \frac{8}{\pi h^3} \begin{cases} 1 - 6\left(\frac{r}{h}\right)^2 + 6\left(\frac{r}{h}\right)^3, & 0 \geq \frac{r}{h} \leq 0.5 \\ 2\left(1 - \frac{r}{h}\right)^3, & 0.5 \geq \frac{r}{h} <= 1 \\ 0, & \frac{r}{h} > 1 \end{cases} \tag{2.3}$$

where, r denotes the separation of the particles among which force calculations are performed. If the force calculation using softening are performed it leads to $\frac{1}{2}N(N-1)$ calculations which are the order of N^2 at a given time. When the forces are computed in small time steps the processing time becomes tremendously large for the evolution of astrophysical systems that have large number of particles (million to billion particles). Apart from this, gravity has a long range nature which results in force computation over larger scales, making direct force calculation inefficient. Another method known as "tree algorithm" is largely efficient in this scenario which groups the particles in a hierarchical multipole expansion. The GADGET-2 code uses specifically the Barnes-Hut(BH) octal tree algorithm (Barnes and Hut 1986). This algorithm involves the grouping of distant particles which leads to the total computation of forces for all N particles to be of the order of $NlogN$. This significantly reduce the computation time suitable for studying astrophysical systems. In the BH tree algorithm, the entire mass distribution is enclosed in a cubic node and it is recursively sub-divided into 8 equal daughter cells until only one particle remains in the one daughter cell which is also called the leaf. Each node is associated with a hierarchical multipole expansion of daughter cells. The accuracy of this algorithm depends on the opening angle which is defined as θ in the following equation

for a node of mass M and size l at a distance r:

$$\frac{GM}{r^2}\left(\frac{l}{r}\right) \leq \theta |a| \tag{2.4}$$

where $|a|$ is the total gravitational acceleration calculated in the previous time step.

2.2.2 Time Integration

The timescale which causes the collapse of a density distribution under its self gravity is inversely proportional to the square root of its density. If all the particles in the simulations have to share equal time-steps, then low density regions will have much smaller time steps. Therefore, adaptive and individual time steps are important for numerical simulations. The Gadget-2 code uses leapfrog second order method for time integration of positions and velocities of particles. As the name suggests, velocities and positions of particles are calculated at half time-steps while positions and velocities leaps over each other. The equations which perform leap frog method for an uniform time step dt, position x_i, velocity v_i and acceleration a_i at time t_i is given as:

$$\begin{aligned} x_i &= x_{i-1} + v_{i-dt/2} \times dt/2, \\ a_i &= g(x_i), \\ v_{i+dt/2} &= v_{i-dt/2} + a_i \times dt \end{aligned} \tag{2.5}$$

where, $g(x)$ provides the net acceleration of particles if position is given as input. Therefore in this method velocities are defined at $t_{i-1/2}$, $t_{i+1/2}$, $t_{i+3/2}$ while the positions are defined at t_i, t_{i+1}, t_{i+2} etc.

The leapfrog method is time reversible and it maintains the total energy to oscillate around real energy value. The orbits in the simulations for astrophysical system will be stable for small errors in the integrator (Quinn et al., 1997).

The time step for each particle is calculated from the following formula in GADGET-2,

$$\Delta t_{grav} = min\left(\Delta t_{max}, \left(\frac{2\eta\varepsilon}{|a|}\right)\right) \tag{2.6}$$

where Δt_{max} defines the maximum time-step allowed for a particle, ε is gravitational softening parameter, η is the numerical accuracy parameter and $|a|$ is the acceleration of the particle.

2.3 Exploring parameters for bar formation

We did several test runs to get the idea of stability of axi-symmetric disk against the global non-axisymmetric disks. Here we give brief overview of the test runs rather than going into details.

2.3.1 Halo spin and disk surface density

In this test we generated various galaxy models using GalIC where we increased the halo spin. As we increase halo spin it increases the total angular momentum of halo. The disk angular momentum is chosen to be a fraction of the total angular momentum of halo by the GALIC code. We found that in our galaxy models the disk scale length increases and hence surface density decreases with increasing halo spin. The anticorrelation between disk surface density and halo spin is also seen by Kim and Lee (2013)

2.3.2 Disk surface density

In this case we first prepared mock galaxy models with GalIC with decreasing disk surface densities. Then we evolved these models with GADGET-2 code for checking the stability against bar formation. We started with a high surface density model which forms a bar after few Gyr of evolution. We find that as we reduce the disk surface density, the bar formation time scale increases. As we further reduce the disk surface density the disk becomes stable against the bar mode over 10 Gyr of evolution. This indicates that as the disk surface density decreases, there is not enough self gravity in the disk to allow bar formation. The test gives us an idea of how to form bars in stellar disks of varying densities as also shown in the literature (Athanassoula, 2003).

Imagination will often carry us to worlds that never were. But without it we go nowhere.

Carl Sagan

3

Effect of Bulges on Bar Formation and Evolution

In this chapter we discuss the effect of bulge mass and bulge concentration on bar formation and evolution in galactic disks. We know that bars in the Hubble sequence vary from early to late type spiral galaxies (Binney & Merrifield, 1998; Elmegreen & Elmegreen, 1985; Buta et al., 2015). The bars associated with early type, bulge dominated galaxies (SBa, SBb) appear to be longer than those found in late type spirals (Sc) (Erwin, 2005). There is also a significant correlation between bar strength and bulge mass (Sheth et al., 2008; Skibba et al., 2012; Kim et al., 2014).

The bulges themselves can be broadly classified into two types, the classical bulges that have a sersic index $n > 2$ and the more oval or disky pseudobulges that have $n < 2$ (Fisher & Drory, 2008). Their structure suggests a different formation mechanisms for both types of bulges (Gadotti, 2009). The origin of classical bulges is thought to be a result of major mergers (Kauffmann et al., 1993; Baugh et al., 1996; Hopkins et al., 2009; Naab et al., 2014), multiple minor mergers (Bournaud et al., 2007; Hopkins et al., 2010), monolithic collapse of primordial gas clouds (Eggen et al., 1962) or the accretion of small satellites (Aguerri et al., 2001). Pseudo bulges are formed due to disk instability during secular evolution (Wyse et al., 1997; Kormendy

& Kennicutt, 2004) or buckling instability of bars (Combes et al., 1990; Raha et al., 1991; Martinez-Valpuesta et al., 2006), the inward pull of gas by bars (Combes & Sanders, 1981) and heating of bars by vertical resonances (Combes & Sanders, 1981), resulting in boxy/peanut shaped bulges.

Theoretical studies have shown that bars will form in self gravitating, rotating disks when most of the kinetic energy is in rotational motion i.e. in cold disks (Hohl, 1971; Kalnajs, 1972) unless there is a massive dark matter halo that stabilizes it against bar formation by providing a spherical gravitational field (Ostriker & Peebles, 1973). However recent studies (Athanassoula & Misiriotis, 2002; Athanassoula, 2003) show that a cold disk can become bar unstable despite the presence of a massive halo, which shakes the credibility of these previous studies. Global disk instabilities such as bars and spirals arms can also be triggered by disk perturbations due to interactions/mergers with minor satellites or larger galaxies (Noguchi, 1987; Gerin et al., 1990; Salo, 1991; Barnes & Hernquist, 1991; Mayer & Wadsley, 2004; Romano-Díaz et al., 2008). The evolution of bars in disk galaxies has been extensively studied with N-body simulations over the past few decades (Sellwood, 1980; Combes & Sanders, 1981; Efstathiou et al., 1982; Athanassoula & Misiriotis, 2002; Athanassoula, 2002, 2003; Valenzuela & Klypin, 2003; Machado et al., 2012; Saha & Naab, 2013; Long et al., 2014). The disk-halo interaction has been shown to play an important role not only in bar formation but also bar rotation speeds (Weinberg & Katz, 2007a; Debattista & Sellwood, 2000). Studies with live halos show that bars evolve secularly in isolated galaxies through the exchange of angular momentum between disk stars and halo particles at radii corresponding to the disk resonances (Long et al., 2014). Faster rotating halos may also trigger early bar formation (Long et al., 2014) but can also make bars weaker in the secular evolution phase. The bulges also gain angular momentum from the disk at resonances and this results in the spinning up of bulges(Saha et al., 2012). These studies are similar to previous classical studies in which disk stars lose angular momentum at resonances (Lynden-Bell & Kalnajs, 1972; Lynden-Bell, 1979) or by being trapped in slowly rotating bar structures through dynamical friction (Tremaine & Weinberg, 1984a).

Although there have been many simulation studies of the effect of disk-halo interaction on bars, there are very few studies of the effect of bulges on bars. Since bulges contribute significantly to the radial force in disks, bulge masses and sizes can affect bar formation (Hohl, 1976). One of the earlier theoretical studies of the effect of bulges on disk instabilities (Toomre, 1981b) showed that the presence of a strong bulge component in disk galaxies cuts off the feedback mechanism during swing amplification (Binney & Tremaine, 2008) by introducing an Inner Lindblad Resonace (ILR) in the disk. The ILR does not allow trailing waves to go through the center and emerge out as leading waves; this prohibits the growth of bar type instabilities. However, detailed N-body simulations showed that this is not always true (Sellwood, 1980);

about 50 to 70 % of total galactic baryonic mass has to be in a spherical component to prevent the onset of bar instability in disk galaxies. These early studies used a spherical mass smaller than the disk but referred to it as a "halo" rather than a bulge (Sellwood, 1980). Further studies (Efstathiou et al., 1982) showed that bar type instabilities can be sustained irrespective of the density of the bulge component. However, these studies used rigid bulges (Sellwood, 1980; Efstathiou et al., 1982). When live bulges were used, it was found that the bulges gained angular momentum from the disks and this increased as the bar evolved (Sellwood, 1980). The disadvantage of all these early studies is that they did not include dark matter halo components in their galaxy models.

The above discussion holds for mainly isolated galaxies that are secularly evolving. However, when there are external perturbations to galaxy disks due to interactions with nearby galaxies, stellar bars can form even in the presence of a strong bulge. In such cases the ILR is not able to prevent the growth of bars. Later studies that included halo components in their models suggested that the presence of massive bulges make disks stable against bar formation (Sellwood & Evans, 2001). It is well known that the probability of having an ILR is higher when there is a massive bulge as the angular velocity Ω of stars in the disk increases and hence the critical value $\Omega_{crtical} = \Omega_p + \kappa/2$ will be reached, therefore cutting off feedback mechanism as discussed in the last paragraph, where Ω_p and κ are the pattern speed of bar and epicyclic frequency of stars. However, there are many non-linear processes in galaxy evolution which allow bar formation in bulge dominated disk galaxies (Widrow et al., 2008; Dubinski et al., 2009). Cosmological hydrodynamic simulations (Scannapieco & Athanassoula, 2012) also show that strong bars can form in galaxies that have prominent bulges rather than those without bulges.

Recent studies have shown that bars can also affect bulges by increasing their spin (Saha et al., 2012; Saha, 2015; Saha et al., 2016). However, there is no detailed study which explores the effect of bulge masses on bar formation and its evolution. In this chapter we re-visit the dependence of bar formation on bulges but with a difference; we vary not only the bulge mass but also its concentration. We also focus on the angular momentum transfer between the disk and bulge, since angular momentum transfer between disks and dark matter halos has been found to play a key role in bar evolution (Long et al., 2014). Thus the goal of this chapter is to determine how bulge mass and concentration affects bar formation, morphology, pattern speed and angular momentum transfer between the different galaxy components (bulge, disk, halo). Our models start from bulgeless galaxies to bulge dominated disks where the bulge to disk mass ratio can be as high as 70%. We have two sets of models, one with a concentrated bulge and the other with a less concentrated bulge.

The plan of the chapter is as follows. In Section 3.1 we discuss the numerical techniques used for this work which includes initial condition generation and simulation methods. In Section 3.2 we discuss the evolution of various bar parameters in the different cases, such as pattern speed, bar strength, angular momentum transfer between disk and bulge components and the origin of pseudo bulges in our models. Apart from this in the same section we discuss a model independent parameter that can be used to determine the limiting bulge force for bar formation. In Section 3.3 we discuss the implication of our results for bulge-bar correlations in disk galaxies. Finally in the Section 3.4 we summarize our work.

3.1 Modelling and Evolving Galaxies

3.1.1 Initial Conditions of modelled galaxies

For generating initial disk galaxy models we have used the code GalIC (Yurin & Springel, 2014). The number of particles used for the simulation is 10^6 dark matter halo particles, 10^5 disk particles and $5\text{x}10^4$ bulge particles.

We present here two categories of galaxy models that we denote as MA and MB (here onwards in this chapter) that have disk, bulge and dark matter halo components. The models MA have relatively smaller disks and higher disk mass surface densities than that of models MB. The purpose of taking these two models is to see the growth and evolution of bar instabilities in both larger and smaller disk galaxies. The galaxy models MA have more concentrated or denser bulges compared to models MB. The various parameters of the initial models generated is shown in Table 5.1. From top to bottom the bulge mass content is increasing in both MA and MB models respectively. Fig. 3.1 and 3.4 show initial and final rotation curves, initial surface density and initial toomre parameter with radius for both MA and MB models respectively. Fig. 3.3 and 3.5 shows the contribution of the different galaxy components to the rotation curves of the galaxy models. Fig 3.2 and 3.6 show the initial radial velocity dispersion of stellar disk for models MA and MB respectively.

The density profile for a spherically symmetric halo is chosen as

$$\rho_h = \frac{M_{dm}}{2\pi} \frac{a}{r(r+a)^3} \tag{3.1}$$

where a is the scale length of the halo component. This scale length is related to the concentration parameter of the NFW halo having $M_{dm} = M_{200}$ (Springel et al., 2005) so that

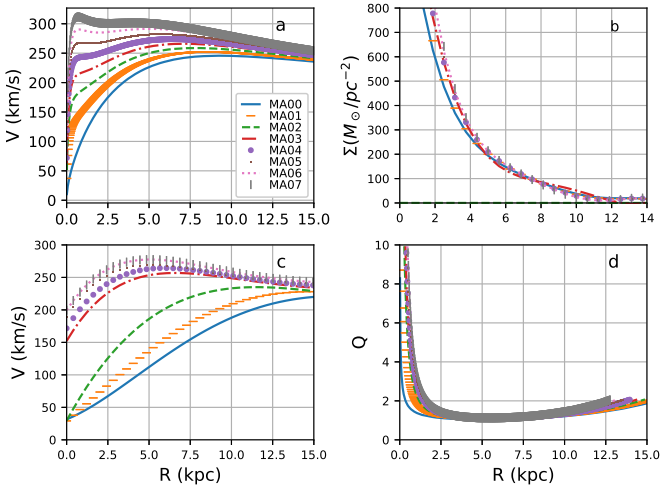

Fig. 3.1 a) Initial rotation curves of disk stars; b) Surface density; c) final rotation curve at 9.78Gyr. d) toomre parameter variation with radius for all the MA models

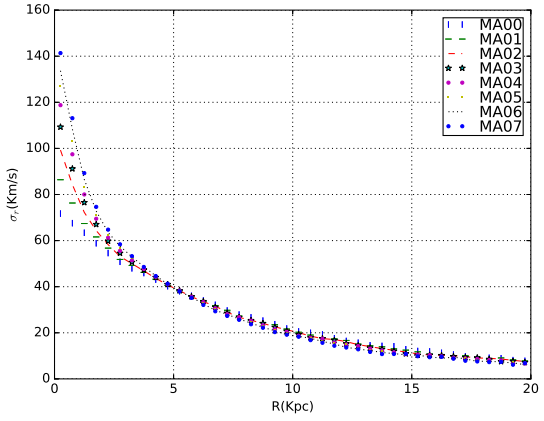

Fig. 3.2 Initial radial velocity dispersions for all the MA models

Table 3.1 Initial Disk Models with increasing bulge masses

Models	$\frac{M_B}{M_D}$	$\frac{M_B}{M_T}$	$\frac{M_D}{M_T}$	$\frac{M_H}{M_T}$	$\frac{R_b}{R_d}$	$Q(R_D)$	M_B $[10^{10}M_\odot]$	t_{OP}
MA00	0	0	0.1	0.9	0	1.077	0	0.180
MA01	0.1	0.01	0.1	0.89	0.174	1.123	0.64	0.179
MA02	0.2	0.02	0.1	0.88	0.180	1.171	1.28	0.179
MA03	0.3	0.03	0.1	0.87	0.186	1.220	1.93	0.177
MA04	0.4	0.04	0.1	0.86	0.192	1.269	2.55	0.175
MA05	0.5	0.05	0.1	0.85	0.198	1.319	3.19	0.176
MA06	0.6	0.06	0.1	0.84	0.204	1.368	3.83	0.177
MA07	0.7	0.07	0.1	0.83	0.210	1.418	4.47	0.177
MB00	0	0	0.1	0.9	0	1.239	0	0.192
MB01	0.1	0.01	0.1	0.89	0.439	1.273	1.86	0.193
MB02	0.2	0.02	0.1	0.88	0.447	1.305	3.72	0.194
MB03	0.3	0.03	0.1	0.87	0.456	1.337	5.58	0.195
MB04	0.4	0.04	0.1	0.86	0.465	1.370	7.44	0.196
MB05	0.5	0.05	0.1	0.85	0.473	1.401	9.30	0.197
MB06	0.6	0.06	0.1	0.84	0.481	1.433	11.16	0.198
MB07	0.7	0.07	0.1	0.83	0.490	1.465	13.02	0.199

column(1)Model name (2)Ratio of bulge to disk mass (3) Ratio of bulge to total galaxy mass (4) Ratio of disk to total galaxy mass (5) Ratio of halo to total mass (6) Ratio of half mass bulge radius to disk scale length(R_b/R_d) (7)Toomre parameter at disk scale length R_d(8) Bulge mass (9) Ostriker and Peebles criterian for bar instability t_{OP} explained in section 3.2.4

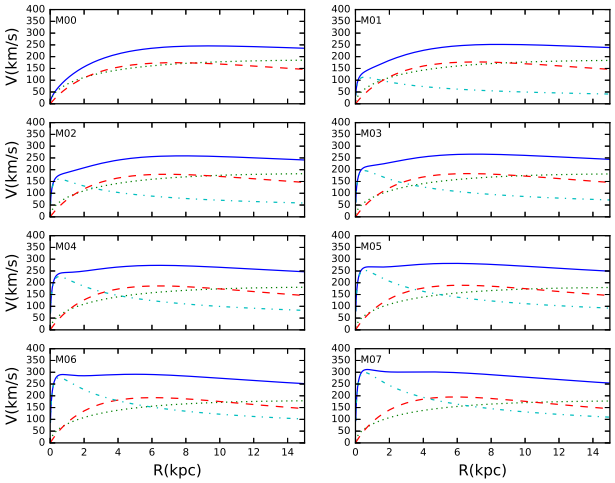

Fig. 3.3 Represents rotational curves for all of our MA models. Here solid line shows rotational velocity due to all the components; Halo (dotted line);disk (dashed line);Bulge (dash-dot line)

the inner shape of the halo is identical to the NFW halo. Here a and c are related as following

$$a = \frac{R_{200}}{c}\sqrt{2[ln(1+c) - c/1+c]} \tag{3.2}$$

where M_{200}, R_{200} are virial mass and virial radius for NFW halo respectively.

The density profile for the disk component has an exponential distribution in the radial direction and $sech^2$ profile in the vertical direction.

$$\rho_d = \frac{M_d}{4\pi z_0 h^2} exp\left(-\frac{R}{R_d}\right) sech^2\left(\frac{z}{z_0}\right) \tag{3.3}$$

where R_d and z_0 are the radial scale length and vertical scale length respectively. The values of these parameters are listed in Table 5.1 for all of our models.

Finally the bulge component in our models has a Hernquist density profile given by

$$\rho_b = \frac{M_b}{2\pi}\frac{R_b}{r(r+R_b)^3} \tag{3.4}$$

where M_b, R_b are total bulge mass and bulge scale length respectively. These values are listed in Table 5.1.

Table 5.1 also contains many other parameters like bulge to disk fraction, bulge to total galaxy mass fraction, disk to total galaxy mass fraction, halo to total galaxy mass fraction, Toomre factor at disk scale length (R_d) and bulge mass. For all the MA and MB type models

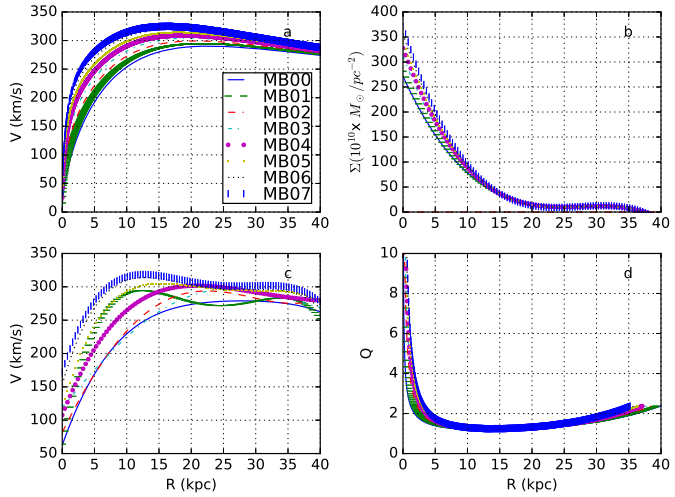

Fig. 3.4 a)Initial rotation curves of disk stars; b)surface density; c)final rotation curve at 9.78Gyr; d)toomre's parameter variation with radius for all the MB models

the total mass of the galaxies is decided by the velocity at virial radius which in our model is equal to 140 Km/s and 200 Km/s respectively. Total galaxy mass for MA galaxy models is equal to 63.8 x$10^{10} M_{\odot}$ and for MB type models it is 186 x$10^{10} M_{\odot}$. Mass content in disk component for all the MA and MB models are 6.38 x$10^{10} M_{\odot}$ and 18.6x$10^{10} M_{\odot}$ respectively. In our models, ratio of particle masses in halo, disk and bulge varies for different models. For MA models, ratio of particle masses goes from 1:1.12:0.22 for MA01 to 1:1.2:1.68 for MA07. For MB models, ratio of particle masses of halo, disk and bulge varies from 1:1.2:0.22 for MB01 to 1:1.20:1.03 for MB07. Both of our models are dark matter dominated and dark matter makes up 90% of the total galaxy mass. In our models we have chosen the spin parameter for the dark matter halo component to be 0.035 which is shown to be the most probable value from cosmological simulations (Bullock et al., 2001). Bulges in all the models are non-rotating. We have checked that all the models are locally stable as Toomre parameter is greater than 1 for all the models through out the disk. The Toomre factor varies with radius and is given by $Q(r) = \dfrac{\sigma(r)\kappa(r)}{3.36G\Sigma(r)}$. Here $\sigma(r)$ is the radial dispersion of disk stars, $\kappa(r)$ is the epicyclic frequency of stars and $\Sigma(r)$ is the mass surface density of the disk.

3.1.2 Simulation Method

After all the initial galaxy models are prepared we evolve these models in isolation with Gadget-2 code (Springel, 2005). We evolved these galaxies up to 9.78 Gyr to check secular evolution of the disks in our models. The opening angle for the tree is chosen as θ_{tot} =0.4. The softening

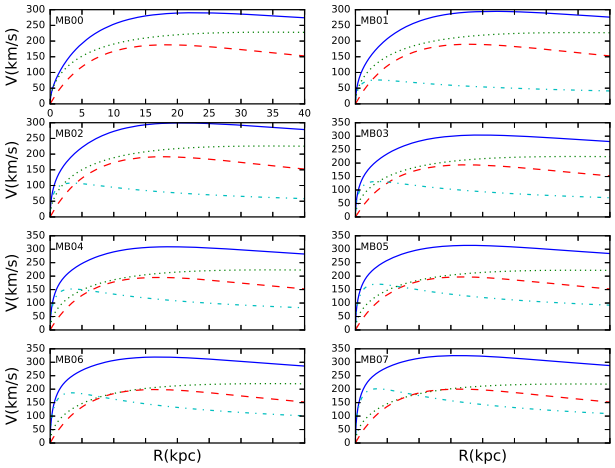

Fig. 3.5 Represents rotational curves for all of our MB models. Here solid line shows rotational velocity due to all the components; Halo (dotted line);disk (dashed line);Bulge (dash-dot line)

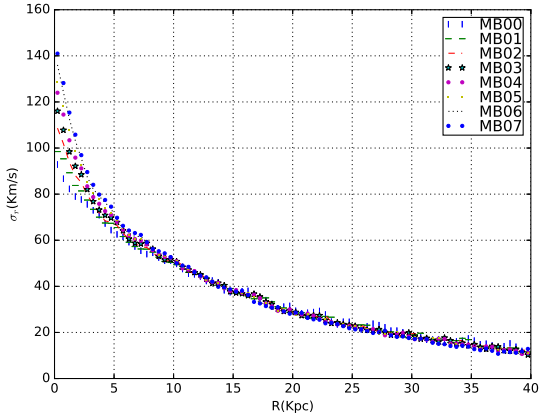

Fig. 3.6 Initial radial velocity dispersions for all the MB models

length for halo, disk and bulge components has been chosen 30, 25 and 10 pc respectively. We mention our results in terms of code units.

The introduction of concentrated bulges increases the frequency of 2 body interactions in our simulations and affects the conservation of angular momentum of the galaxy. This means that the force calculation accuracy plays a important role in determining position and velocities of the particles and therefore angular momentum conservation. We have done many test simulations to determine the most important parameters for conserving the angular momentum. We found that reducing the softening length does not help much in conserving the angular momentum. Instead for our current simulation, reducing the time step of integration (η) and the force accuracy parameter over the evolution time period are the most important parameters for angular momentum conservation(Klypin et al., 2009). We haves used the values $\eta <= 0.15$ and force accuracy parameter $<= 0.0005$ in most of the simulations. As a result in all of our models, the angular momentum is conserved to within 1 % of the initial value.

3.1.3 Bar strength and Pattern Speed

Bar strength has been defined in different ways in the literature (Combes & Sanders, 1981; Athanassoula, 2003). In our study for defining bar strength we have used the mass contribution of disk stars to the m=2 fourier mode.

$$a_2(R) = \sum_{i=1}^{N} m_i \cos(2\theta_i) b_2(R) = \sum_{i=1}^{N} m_i \sin(2\theta_i) \tag{3.5}$$

where a_2 and b_2 are defined in the annulus around the radius R in the disk, m_i is mass of i^{th} star, θ_i is azimuthal angle. We have defined the bar strength as

$$\frac{A_2}{A_0} = max\left(\frac{\sqrt{a_2^2 + b_2^2}}{\sum_{i=1}^{N} m_i}\right) \tag{3.6}$$

We calculate the pattern speed(Ω_B) of the bar by measuring change in phase angle $\phi = \frac{1}{2}\tan^{-1}\left(\frac{b_2}{a_2}\right)$ of the bar which is calculated using the fourier component in the annulus corresponding to maximum bar strength. We use annular regions of size 1 kpc for disk particles only.

3.1.4 Angular Momentum Calculation

We measured the angular momentum of the different components of a galaxy separately; disk, bulge and halo. Angular momentum of a particle is calculated using the product of its particle

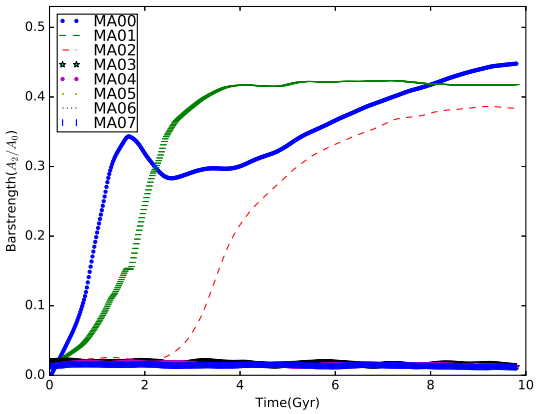

Fig. 3.7 Evolution of bar strength with time for all MA models.

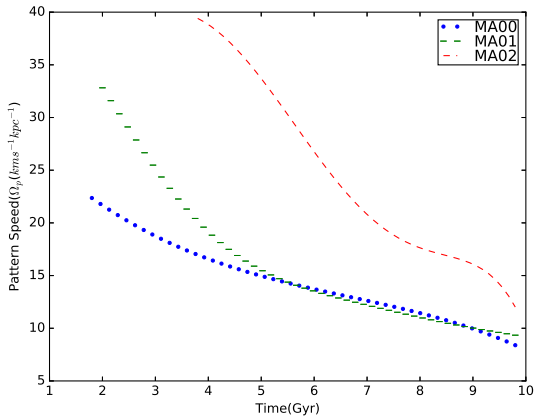

Fig. 3.8 Pattern speed evolution with time of all bar forming MA models

mass, radial distance from galactic center and circular velocity. In this paper we plot time evolution of total angular momentum of each component in the galaxy.

3.2 Results

3.2.1 Evolution of Bar Strength

We tracked bar formation and evolution up to 9.78 Gyr in all of the models from MA00 to MA07. Figure 3.7 shows the evolution of bar strength for these models. The X-Y face-on view of all the MA models after 9.78 Gyr is shown in Figure 3.9. We see that the model without bulge (MA00) grows to peak bar strength around 1.5 Gyr during dynamical evolution and

it's bar strength decreases rapidly before secular evolution phase. In secular evolution it's bar strength increases gradually with time. In the model with low mass bulges (MA01) the bar grows to peak strength around **3 Gyr** and sustains its strength during secular evolution phase. Further with increasing bulge masses in model MA02, bar instability sets in later and reaches peak value around **7 Gyr.** In the later models MA03, MA04, MA05, MA06 and MA07 that have bulge to disk fraction > 0.3 bar type of instability is suppressed completely due to the presence of massive bulge.

Figure 3.11 shows evolution of bar strength for the models MB00 to MB07, that have less concentrated bulges and lower disk surface densities compared to models MA00 to MA07. As in the previous models, the simulation is run for 9.78 Gyr. The main difference in the bar evolution of models MA and MB is that the bar forms much later in model MB. This is due to the lower mass surface density Σ of the disk which leads to a lower disk self gravity and hence instabilities take longer to develop. We find that the model with no bulge (MB00) shows bar type instability, for which bar strength peaks at around **7.5 Gyr** and the bar gets weaker with further evolution. On introduction of a bulge in our MB models we see that the bar strength shows nonlinear trends as a function of bulge to disk fraction. For small bulge to disk ratios of 0.1- 0.3, the bar triggering time scale increases with bulge mass and the peak bar strength remains almost the same. As we increase bulge fraction from 0.4 to 0.6 we see that the bar formation time scale increases and peak strength reduces for the time we evolve our model. For models with bulge to disk fraction 0.7, a bar does not form at all. The X-Y face on views of all the MB models after 9.78 Gyr is shown in Figure 3.10

3.2.2 Evolution of Bar Pattern Speed

We show the evolution of bar pattern speed (Ω_p) with time in Figure 3.8 for all MA models which form bars. In this plot we do not have models MA03 to MA07 because their disks do not form bars. It is very clear that the disks that have more massive bulges have bars with higher Ω_p. Also, in all the models, the Ω_p decreases with time and the rate of decrease in pattern speed increases with increase in bulge mass fraction.

The variation of bar pattern speed with time for all MB models which form bars, is shown in Figure 3.12. Note that we can plot Ω_p only after the bars form and start growing. So this plot excludes models MB06 and MB07 which do not form bars. As in models MA, as the bulge fraction increases (from MB00 to MB05), the Ω_p value is higher. Thus, bar rotation is faster for bulge dominated galaxies, whatever be the bulge concentration or disk surface density. This is because the increase in bulge mass makes the inner disk potential deeper resulting in larger angular velocities. In all the bar forming models, Ω_p shows little variation for several Gyr until

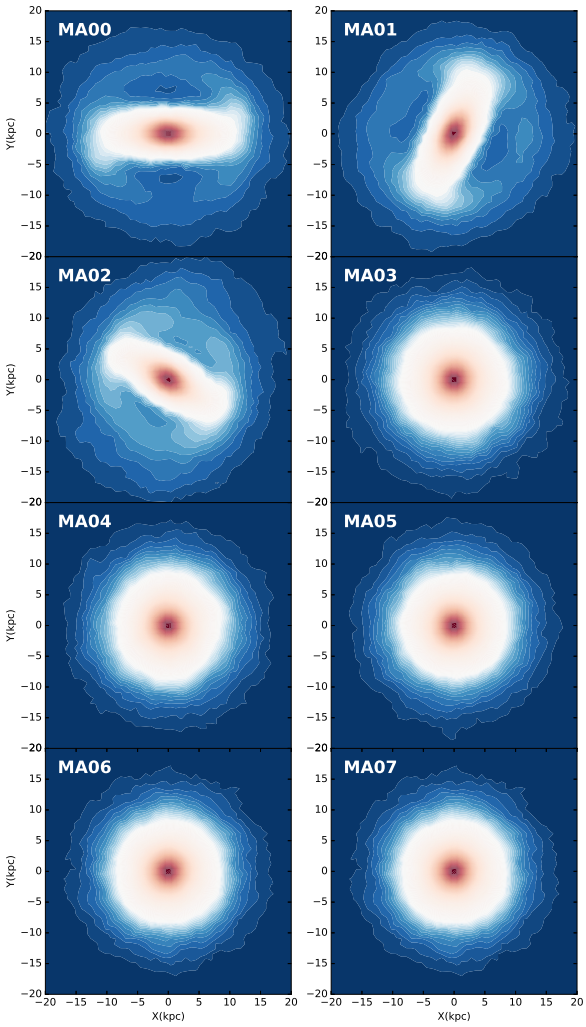

Fig. 3.9 X-Y cross section of all the MA models at 9.78 Gyr

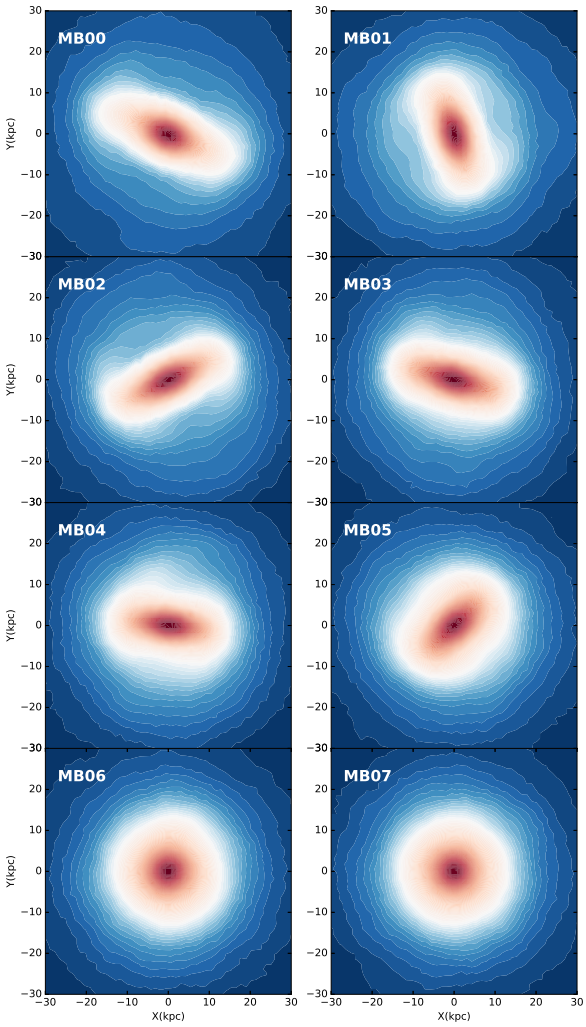

Fig. 3.10 X-Y cross section of all the MB at 9.78 Gyr

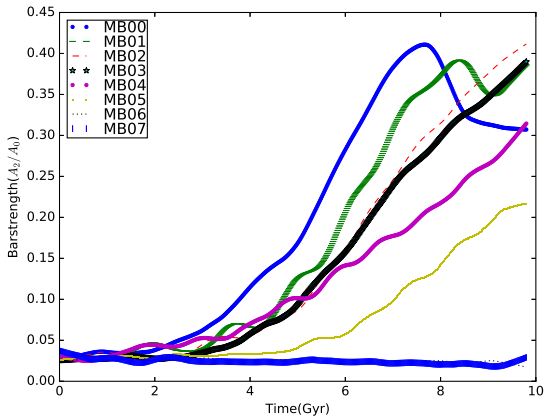

Fig. 3.11 Evolution of bar strengths with time for all MB models.

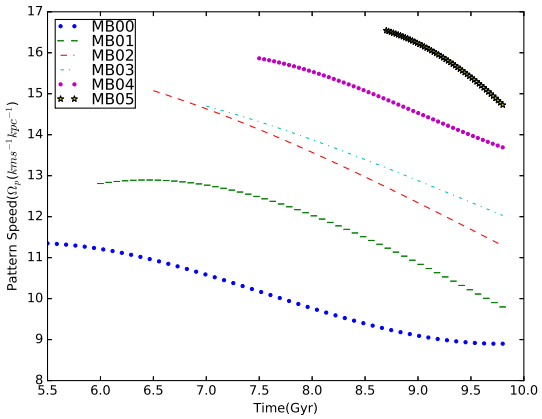

Fig. 3.12 Pattern speed evolution with time of all bar forming MB models

8 to 9 Gyr, after which Ω_p decreases sharply with time. We interpret that this may be related to the thickening of the bar as the bar growth peaks after this time period.

3.2.3 Angular Momentum Exchange

Several studies have shown that angular momentum exchange between the disk and halo plays a vital role in the formation and evolution of bars (Athanassoula, 2003; Valenzuela & Klypin, 2003; Martinez-Valpuesta et al., 2006; Saha & Naab, 2013; Long et al., 2014). We see this in both MA and MB type of models in our simulations. In this sub-section we discuss the importance of angular momentum transport between the disk, halo as well as bulge in our models. We have also plotted the total angular momentum exchange with time for the individual galaxy components in Figure 3.13 and Figure 3.14 for MA and MB type models respectively.

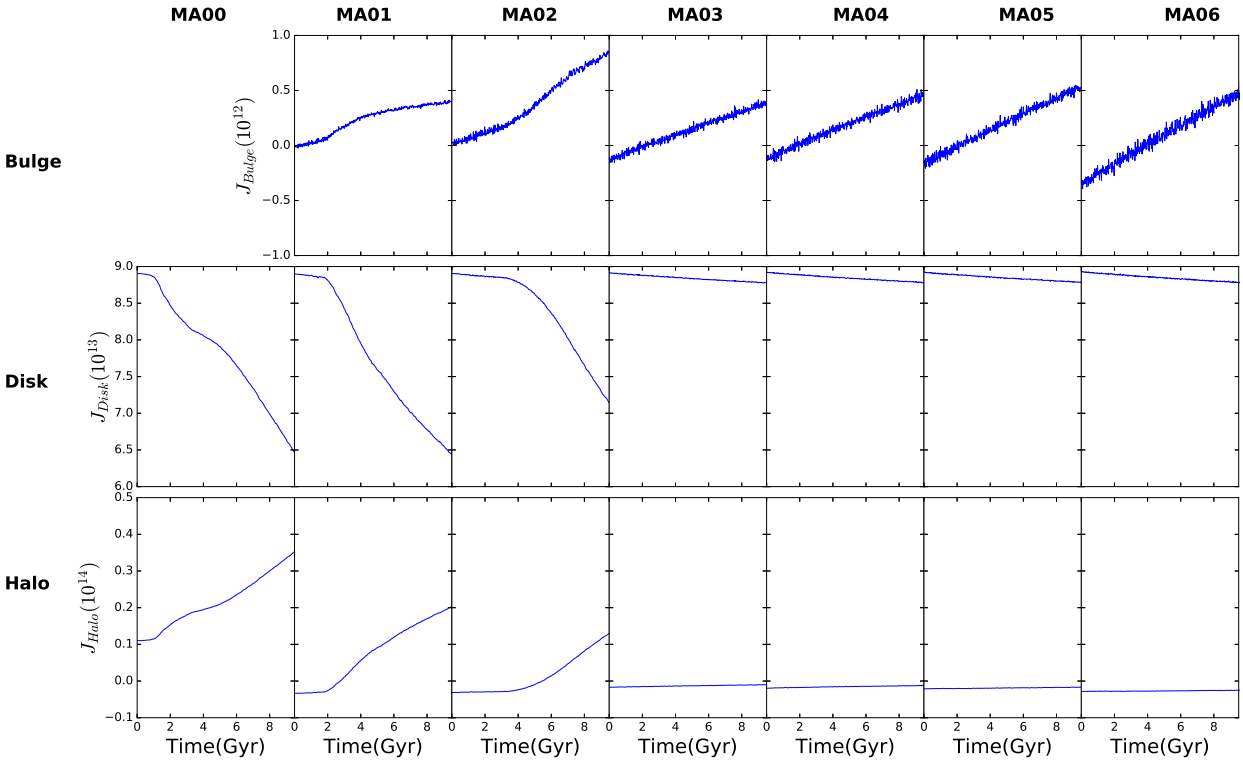

Fig. 3.13 Total Angular Momentum for all the components(Bulge, Disk and Halo) of all MA models

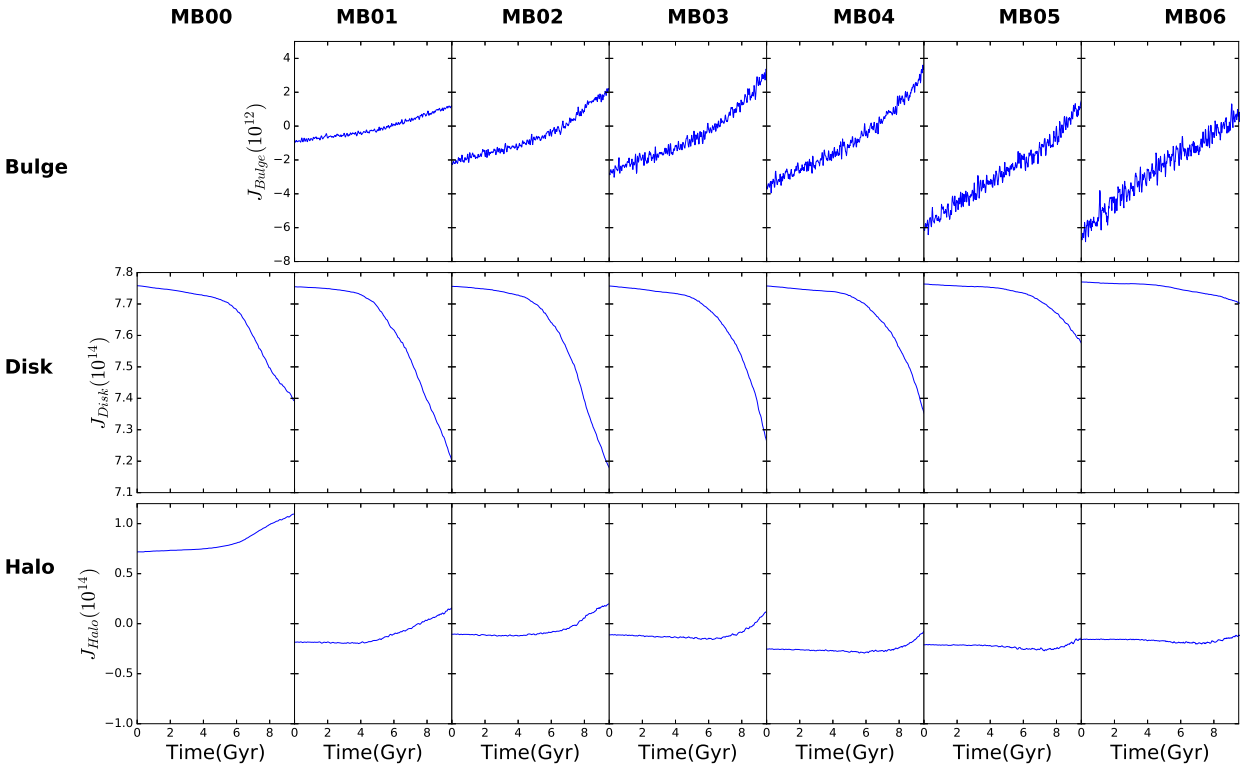

Fig. 3.14 Total Angular Momentum for all the components(Bulge, Disk and Halo) of all MB models

3.2.3.1 MA Models : High density bulges and disks

The overall change in angular momentum for bulge, disk and halo components of MA models are shown in Figure 3.13. We see that disk component loses total angular momentum by huge amount in bar forming models compare to models which does not show bar instability. We also see that angular momentum loss rate for the disks increases sharply when the bars reach their peak strength, the time scale for which increases with increase in bulge mass.We can see that the total angular momentum gain is maximum for the halo component and is around 15 to 20 times that of the bulge component.

We also note that the total angular momentum of the bulge component first increases with increase in bulge mass for models MA00, MA01 and MA02 which show bar instabilities. Further increase in bulge mass in model MA03 leads to decrease in bulge angular momentum. After this, an increase in bulge mass (Model MA04 onwards) results in a slow increase in the bulge total angular for all the bulges and could represent the slow spin up of bulges.

For the halo component, the total angular momentum exchange is maximum for the MA00 model which does not have a bulge. On introduction of bulge for models MA01 and MA02, the halo component gains angular momentum after the bar gains its peak strength around 2 Gyr and 4 Gyr respectively. For models MA03 onwards where the bar instability is not triggered and the bulges mass increases, the angular momentum exchange becomes very small.

3.2.3.2 MB Models : low density bulges and disks

In all the MB models, the bar forms after 6 Gyr which is much later than in the MA models, mainly because the the disk mass surface density is much lower. Figure 3.14 shows total angular momentum change for bulge, disk and halo components of all the MB models. We see that disk component loses angular momentum by large amount in bar forming models. Similar to MA models here also the rate of decrease in angular momentum correlates with the bar strength peaking time scale which is shown in Figure 3.11. Total loss of angular momentum by disk component decreases with increase in bulge mass as we go from MB01 to MB07. In these models we see that both halo and bulge components gain angular momentum. Also, the total angular momentum gain is maximum for the halo component and is around 5 to 40 times that of the bulge component.

We see that increase in total angular momentum of bulge increases with increase in bulge masses. It can also be seen clearly that rate of increase of angular momentum for bulge components increase after bar strengths peak which varies in all the models.

The rate of gain in angular momentum by the halo component also start increasing only after the bar gets its peak strength. Further total change in angular momentum of halo component

decreases with increase in bulge mass. This clearly shows that a massive bulge component delays bar formation by curbing angular momentum transport from disk component to halo component.

3.2.4 Bar Instability criteria

Earlier works have shown that cold stellar disks (Hohl, 1971; Kalnajs, 1972; Athanassoula, 2003) with low velocity dispersion can become bar unstable within a few gigayears of evolution. Ostriker and Peebles have given a criteria that if the ratio of rotational kinetic energy to potential energy of a disk exceeds 0.14 ($t_{OP} > 0.14$), then the galaxy disk is bar unstable (Ostriker & Peebles, 1973). In all of our models(MA and MB), we see that all of the $t_{OP} > 0.14$. This suggests that all of our models should have formed bars as the disk is cold enough to become bar unstable. We show the values of t_{OP} for all the models in Table 1. We find that models MA become bar unstable when $t_{OP} > 0.177$ and models MB become unstable when $t_{OP} > 0.197$. Thus the t_{OP} does not appear to be constant in the different disk models and depends on the disk surface mass density as well as the bulge mass concentration. We suggest that this shift in Ostriker and Peebles criteria to higher values is due to live/spinning nature of halo (Saha & Naab, 2013) and bulge components.

Toomre (1981) has shown that bar instabilities can occur through the feedback mechanism during swing amplification. This feedback mechanism is cut down in the presence of ILR resonances, that do not allow the waves to propagate and hence bars should not form in the presence of ILR's. However, we do not find that the presence of ILRs in our simulation is a deciding criteria for bar formation.

As we know bulges are the prominent mass component in the centres of galaxies. Hence, they contribute significantly to disk rotation in the central regions. We have found that all the bar forming models have fractional bulge to total radial force values, F_b/F_{tot} at the disk scale radius R_d, to have values of less than 0.35. Here $F_b = V_b^2/R_d$ and $F_{tot} = V_{tot}^2/R_d$; $V_b$is velocity due to bulge component and V_{tot} is velocity due to bulge,disk and halo components. We have plotted this ratio F_b/F_{tot} with radius in Figures 3.15 and 3.16 for the models MA and MB. The cut off for fractional bulge force is shown clearly in Figure 3.17. The dots of different shapes represent the values of F_b/F_{tot} at disk scale lengths and the value is never larger than 0.35. Hence, our work shows that bars can form in disk galaxies only when $F_b/F_{tot} < 0.35$. This happens because velocity dispersion of disk stars increases as result of increase in radial force due to increasing mass of bulge component. We thus propose that this is a new criteria for bar formation in terms of radial force due to the bulge mass in the disk. This criteria gives clear idea about the amount of bulge force that prevents bar formation, regardless of the bulge

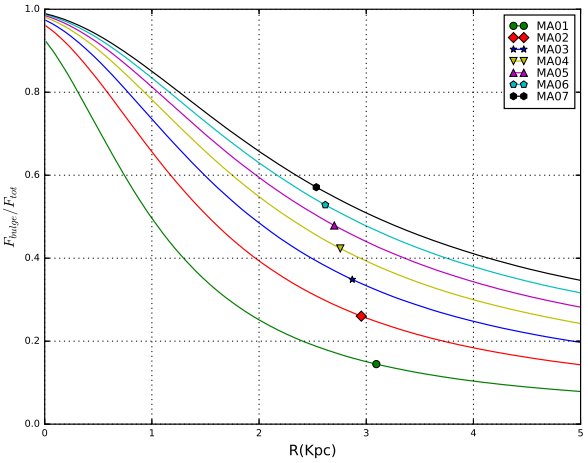

Fig. 3.15 Fractional bulge force at disk scale length for MA Models(various shape dots)

mass or concentration. In the next chapter we have applied this criterion to a large sample of galaxies.

3.2.5 Boxy Bulges in the models

Figure 3.18 and Figure 3.19 show the peanut/box(P/B) shape features at the end of evolution in both the MA and MB models respectively in the y-z planes at both start and end of the simulations. We see that only the bar forming models show P/B feature. Their origin is due to heating of bar through vertical resonances (Pfenniger & Norman, 1990). P/B features are stronger for MA models than MB models. This is because the bar forms earlier (t$\sim$2Gyr) in MA models and this provides sufficient time for bar heating during the secular evolution phase. While in MB models the bar forms much later (t$\sim$6 Gyr) and it does not have enough time to secularly evolve. We find that there is a weak correlation of these P/B feature and the classical bulge mass fraction in both the MA and MB models.

3.3 Implications Of Our Results

Our simulations show that the formation of bar instabilities changes with bulge mass and bulge concentration. Both effects can be explained by the criterion $F_b/F_{tot} < 0.35$ for bar formation, as described in the previous section. The cut off implies that angular momentum transfer among galaxy components gets damped due to increase in velocity dispersion of stars due to introduction of massive bulges. This means that galaxies with strong bulges will not form

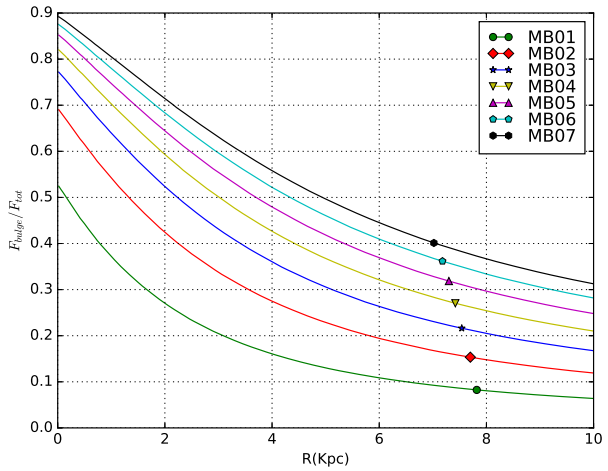

Fig. 3.16 Fractional bulge force at disk scale length for MB Models(various shape dots)

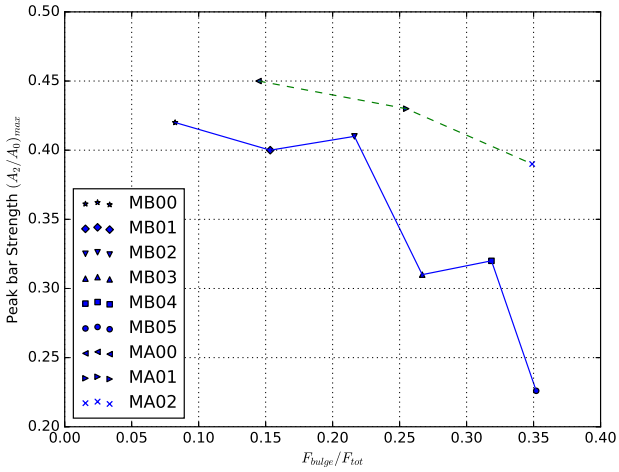

Fig. 3.17 Peak bar strength with respect to fractional bulge force for all the bar forming MA(dashed line) and MB models(solid line).

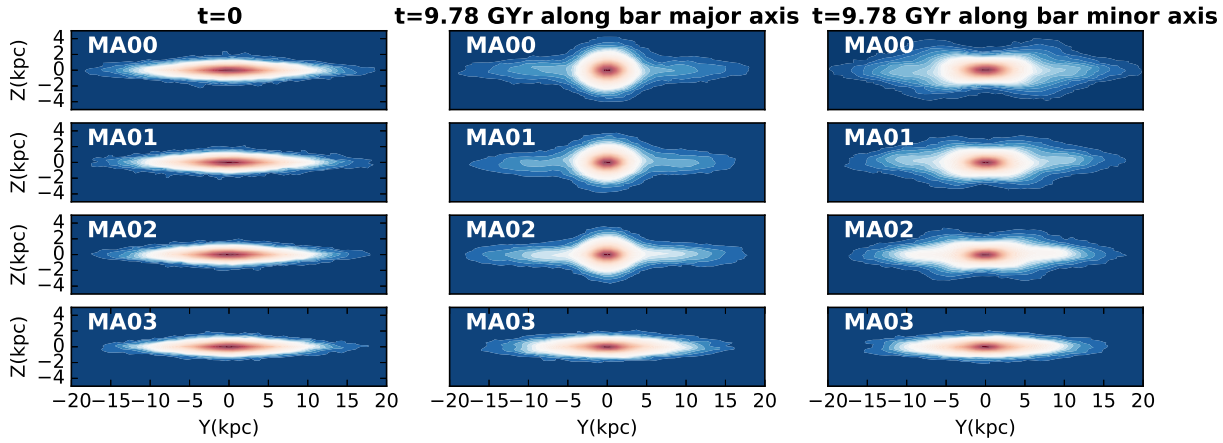

Fig. 3.18 First column shows edge on(YZ cross section) of MA models at t=0; second and third column shows 2 different edge on view at t=9.78 Gyr

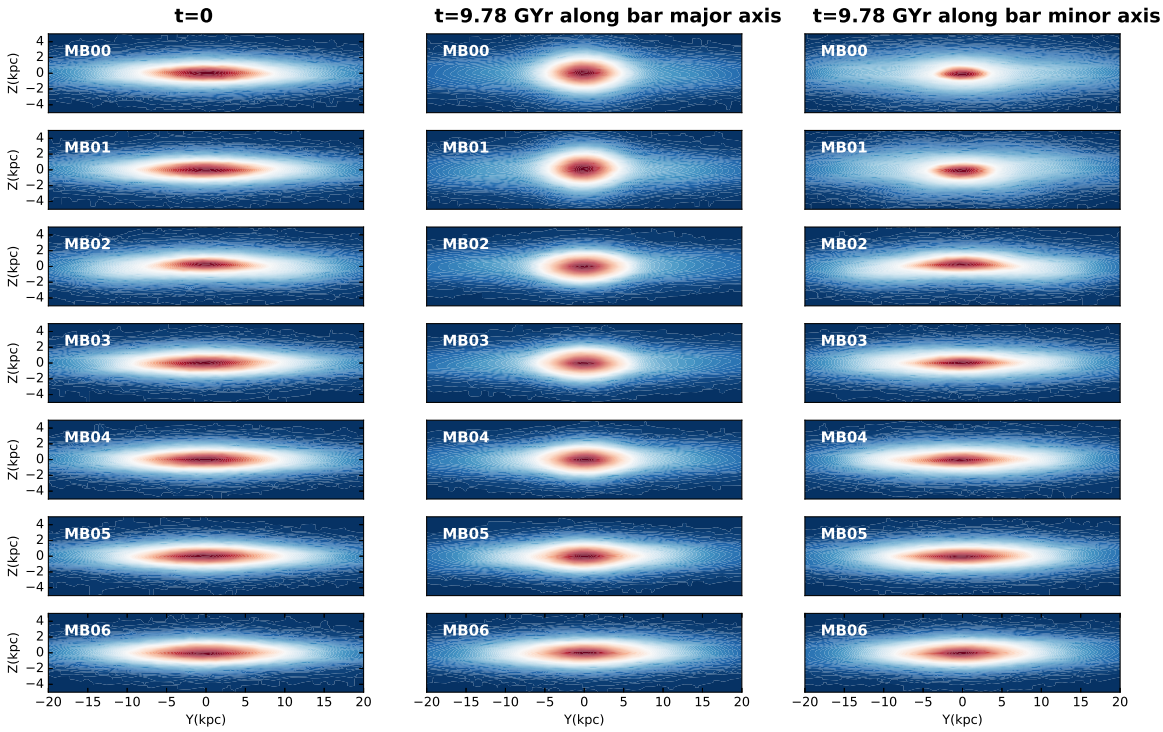

Fig. 3.19 First column shows edge on(YZ cross section) of MB models at t=0; second and third column shows 2 different edge on view at t=9.78 Gyr

bars easily in their disks, perhaps only during interactions with other galaxies as well. Or in other words, strong bulges make disks extremely stable. Such strong bulges may form during galaxy formation epochs, in which case the galaxies do not form bars easily or during secular evolution when gas is driven into the nuclear region by bars or spiral arms leading to the build up of central mass concentrations (Norman et al., 1996; Das et al., 2003, 2008).

Our bulge related bar instability criterion can be easily related to observations in the following way. For a given galaxy image in the near-infrared (which is a waveband that traces the main stellar content of galaxy), a bulge-disk-bar image decomposition will yield the luminosity of the individual components (L_{bulge}, L_{disk}, L_{bar}). Further force due to bulge component can be calculated through mass of bulge (M_{bulge}), which can be obtained by multiplying M/L ratio with L_{bulge}. Rotation curve(V_{tot}) and disk scale length of the galaxy can be used to obtain total force due to galaxy at disk scale length. Hence, our criterion can be written in observable quantities as:

$$\frac{F_b}{F_{tot}} = \frac{GM_{bulge}}{R_d V_{tot}^2} \tag{3.7}$$

This effect of strong bulges can be clearly seen in observations of bulge dominated disk galaxies. Bars are not common in S0 galaxies that have classical bulges and bulge-disk decomposition for S0's reveal a bulge to total luminosity (B/T) value equal to 0.35 (Barway et al., 2016). This value is similar in nature to our criterion of $F_b/F_{tot} < 0.35$. Studies of late type spiral galaxies indicate that bulge dominated spirals have a smaller fraction of barred galaxies compared to disk dominated ones (Barazza et al., 2008). However, later studies with Galaxy Zoo have shown that bars tend to form in disks with stronger bulges (Hoyle et al., 2011). A more rigorous study of B/T values for a large sample of barred galaxies is required to fully test our criterion. Another important implication of our study is that bars do form in dark matter dominated disks. Our models MB are similar to large LSB galaxies that contain massive dark matter halos which is supposed to make disks stable against bar formation as predicted by classical theory (Hohl, 1971; Ostriker & Peebles, 1973). We see bar instability in our models despite the massive dark matter halos; this is similar to the observations of low surface brightness galaxies (e.g. UM 163) (Honey et al., 2016). This can be explained by the live and rotating nature of halos as seen in our study and others in the literature (Saha & Naab, 2013; Long et al., 2014). In our case we have assumed a constant halo spin value equal to 0.035.

Another important implication of this study is the continuous gain in angular momentum by the bulge. We see that for the models that do not form bars, there is no angular momentum exchange with the halo, as shown in Figures 3.13 and 3.14. But the bulge component always

gains angular momentum irrespective of bar formation in all the models. The amount of angular momentum absorbed by the bulges is more in the case when the disk forms bars.

3.4 Summary

In this paper we have used N-body simulations to understand the effect of bulge mass and bulge concentration on bar formation and evolution in disk galaxies. We have evolved two models; models MA have dense bulges and disks of relatively high surface mass density Σ and models MB have less dense bulges and low Σ values compared to MA. We vary the bulge mass in similar steps for both models.

1. For models with concentrated bulges (MA) we notice that a bar forms earlier for bulgeless galaxies compared to those with bulges. The delay in bar formation increases as the bulge to disk mass fraction increases. No bar forms when the bulge to disk mass fraction is > 0.3.

2. For less dense bulge models (MB), the bar formation time scale increases with bulge mass up to bulge to disk mass fraction equal to 0.5. No bar forms when the bulge to disk mass fractions is > 0.6.

3. Our simulations show that bars are faster for models with massive bulges. The rate of decrease in pattern speed of the bar increases with introduction of massive bulges in our galaxy models.

4. We see that in both MA and MB type models, the introduction of more massive bulges makes the disk stellar dispersion higher in the inner disk region. Hence massive bulges do not allow overall disk-halo angular momentum exchange which in turn makes the disk bar stable. The fraction of bulge to disk mass ratio required to make a disk bar stable varies with the density of bulge. In our study we see that it has a value of 0.3 for the dense bulge models (MA) and 0.6 for the low density bulge model (MB).

5. We put a limit on bar formation in disks with bulges by introducing a quantity B which is the ratio of radial force due to bulge and disk components (B = F_b/F_{tot}) at disk scale length (r_d). We find that bars do not form for B$>$0.35. This is because the velocity dispersion of disk stars becomes large enough to inhibit bar type instability. This criterion does not depend on bulge concentration but takes into account the radial force due to a bulge that prohibits bar formation. It is similar to earlier values derived for disks with spherical halos (Sellwood, 1980).

6. Rate of angular momentum transfer to bulge and halo components from disk is more for dense bulges (MA) than less dense ones (MB).

7. Bulge component always gains total angular momentum of the same order irrespective of bar formation in any of the simulated models, while the gain in total angular momentum for halo component dampens by huge amount for bar stable models compare to bar unstable ones.

For small creatures such as we the vastness is bearable only through love.

Carl Sagan

4

Observational test for Our Bar Formation Criterion

In this chapter we test the bar formation criterion derived from simulations in the previous chapter. Early studies have shown that a massive halo component can prevent the formation of bars in disk galaxies (Ostriker & Peebles, 1973; Hohl, 1971). The presence of a massive halo makes a disk kinematically hot and prevents bar instabilities from forming. It has also been shown that a massive central bulge component prevents bar formation as it introduces Inner Lindblad resonances (Sellwood, 1980). Apart from bulge mass, the effect of bulge densities on bar formation have also been explored (Efstathiou et al., 1982). Recent N-body simulations of disk galaxies have shown that both bulge mass and bulge concentration have a strong effect on bar formation timescales in disk galaxies (Kataria & Das, 2018) (hereafter KD2018). The criterion depends on the ratio of the force due to the bulge and that due to the total galaxy at the disk scale length R_d, and is given by $FB = \frac{GM_{bulge}}{R_d V_{tot}^2}$. If this ratio is greater than 0.35, the disk does not form a bar.

Observational studies also show that there exists a correlation between bulges and bars (Sheth et al., 2008; Skibba et al., 2012) as well as between central mass concentration within bulges and bar ellipticity (Das et al., 2003, 2008). It has been observed in large optical surveys

that the bar fraction decreases with increasing bulge brightness (Barazza et al., 2008; Aguerri et al., 2009). As we move from early to late type spiral galaxies along the Hubbe Sequence, it is clear that bulges become less prominent (Binney & Tremaine, 2008). Furthermore, some observations show that bulge to disk mass ratio decreases from early to late type spiral galaxies (Laurikainen et al., 2007; Graham & Worley, 2008). Laurikainen et al. (2007) have shown that bulge to disk flux ratio is smaller for early type barred spiral galaxies compared to early type non-barred spiral galaxies. All of these studies indicate that bars should be less common in early type spiral galaxies.

Thus both observations (Barazza et al., 2008; Aguerri et al., 2009) and simulations (KD2018) indicate that massive bulges do not allow bars to form easily in the disks of galaxies and bulge concentration may also play a role. In this regard the bar formation criterion $FB = 0.35$, determined from simulations of disk galaxies by KD2018 is an important theoretical prediction that can be tested with observations of barred galaxies. The criterion is written in terms of parameters that can be easily obtained from observations and includes the effect of both bulge mass and concentration.

In this chapter, our focus is to obtain the value of FB for each galaxy to test the bar formation criterion mentioned above for a sample of barred galaxies only. For making a fair comparison, we have limited the sample of galaxies with bulge-to-total mass ratios similar to that of the simulated models in KD2018.

This chapter is organized as follows. Section 4.1 summarizes the bar formation criterion. In Section 4.2, we describe the sample data and its analysis. Section 4.3 is devoted to results and discussion. Summary of this work is presented in Section 4.4 .

4.1 The Bar Formation Criterion

The simulations of KD2018 show that both bulge mass and bulge concentration play an important role in inhibiting bar formation in disk galaxies. The study includes 2 types of models called MA and MB, which differ in bulge concentration. In KD2018 bulge concentration is measured by the ratio of bulge half mass radius to disk scale length. The models have bulge to disk mass ratios that vary from 0 to 0.7 or bulge to total galaxy mass ratios that vary from 0 to 0.41. The study shows that if the ratio of radial force due to the bulge component and that due to the total galaxy potential (FB) exceeds a value of 0.35, the bar instability will not develop in the disk. The relation is given by:

$$FB = \frac{F_b}{F_{tot}} = \frac{GM_{bulge}}{R_d V_{tot}^2} \tag{4.1}$$

Here M_{bulge} is the mass of bulge component, R_d is the disk scale length, V_{tot} is the total rotational velocity at disk scale length. They find that the bulge mass that inhibits bar formation is lower for models with dense bulges (MA) compared to models with less dense bulges (MB).

The above formula can be applied to observations fairly easily as long as the bulge luminosity, disk scale length and galaxy rotation velocities are known for a sample of galaxies.

4.2 Data

The first two parameters in equation [4.1], M_{bulge} and R_d, can be obtained from the two dimensional (2D) bulge disk decomposition of a galaxy. For this purpose, we have used the bulge-disk decomposition of barred galaxies provided by Salo et al. (2015). These 2D decompositions were done using 3.6μm images from the Spitzer Survey of Stellar Structure in Galaxies (S4G) using the GALFIT software (Peng et al., 2002, 2010). The study of Salo et al. (2015) provides the bulge, disk and bar parameters of a sample of 100 galaxies along with reliable estimates of their bulge Sersic index and the bulge-to-total light ratio (B/T). In our paper, we aim to see the effect of classical bulges on bar formation and hence we want to calculate FB for only classical bulges. Hence to achieve this goal, we selected bulges with $n > 2$ which is the typical Sersic index for classical bulges (Fisher & Drory, 2008). This reduces our sample size to 56 galaxies.

The other parameter in the bar formation criterion is the rotation velocity at disk scale length, v_{rot}. To determine this parameter, we have used rotation velocities from individual sources detailed in the literature (Table 4.1). For sources for which we could not find individual papers we have used the Hyperleda (Paturel et al., 2003; Makarov et al., 2014) database. This constraint further reduces our sample size to 45 because of the unavailability of rotation curves. For most of the individual sources, we have used HI line widths at full width half maximum (FWHM), also called the W50 value in the literature to determine v_{rot}. It is a measure of the total width at half the peak value of the HI line and is approximately twice the disk flat rotation velocity in a galaxy. These W50 values have been further corrected for galaxy inclination angle to obtain final flat rotation velocities v_{tot}. These rotation velocities correspond to the outer region of galaxies. However, the FB calculation needs rotation velocities at disk scale lengths and so this approximation may result in lower values of the FB constant in some galaxies. A discussion for this limitation is given in section 4.3.

In the simulations presented in KD2018, an upper limit of 0.41 for bulge-to-total mass ratio was used. To obtain the bulge-to-total mass ratio for our sample of galaxies, we have used mass-to-light (M/L) ratio values of 0.5 (Lelli et al., 2016) for converting bulge luminosity to bulge mass. Figure 4.1 shows the distribution of our sample data with respect to bulge-to-total

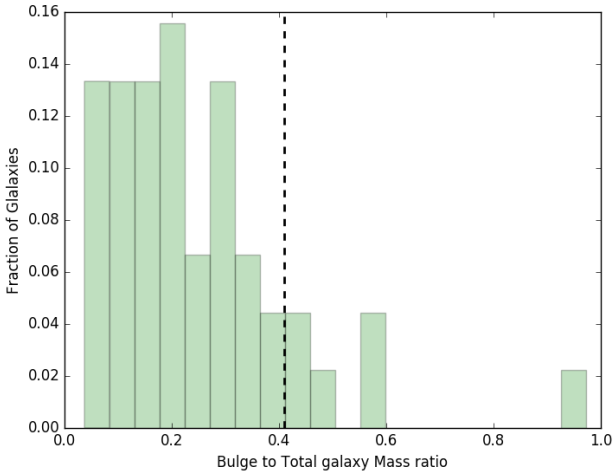

Fig. 4.1 The above figure shows the distribution of bulge to total disk mass for the sample galaxies. Here the vertical dashed line represents the upper limit of this ratio in the simulations of KD2018.

mass ratio. Here, the vertical dashed line denotes the upper limit of the bulge-to-total mass used in simulations (KD2018). In order to have a fair comparison, we have removed the galaxies which are outside the upper limit of bulge-to-total ratio used for simulated galaxies. This further reduces our sample to 39 galaxies which we used for this study. Unless otherwise mentioned, we have used WMAP cosmology (Hinshaw et al., 2013) for converting angular distances to physical distances.

4.3 Results and Discussion

Once the observational data for the galaxy sample was obtained, we calculated the force constant FB using the bulge masses, disk scale lengths and flat rotational velocities for all the sample galaxies. In Fig. 4.2 we have plotted the histogram of the FB parameter for all the barred galaxy sample. We see that all the galaxies lie below the value of 0.35 (Fig. 4.2). This confirms that the value of $FB = 0.35$ represents an upper bound on the fractional radial bulge force which allows bar formation (KD2018).

The HI line-widths W_{50} gives an approximate estimate of two times the flat rotation velocity of the galaxy disk. However, the criterion given by equation [4.1] requires the rotation curve at disk scale length R_d. In general v_{rot} at R_d will be less than $\frac{1}{2}W_{50}$. Hence, our estimates of FB are a lower limit to the values of equation [4.1]. For example, in the case of NGC4569, we initially used a flat rotation velocity v_{rot} of 250 Kms^{-1}. However, the rotation curve shows

that v_{rot} at R_d corresponds to 190 Kms^{-1} (Sofue et al., 1999). Thus, in NGC4569 the FB parameter changes from 0.025 to 0.043. However, both values satisfy the bar formation criterion (FB <0.35). Similarly, if we assume that the rotation curves values at R_d are lower by 25% compared to the maximum value of the rotation curve, which is typically the case for most of the galaxies (Sofue et al., 1999), our criterion will still be valid for 95 % of the sample galaxies.

It will be interesting to explore this bar formation criterion (FB) for our Galaxy, the Milky Way, which is a barred spiral galaxy (Gerhard, 2002). We have obtained the classical bulge mass from the literature and it has a value of 0.89 x $10^{10} M_{\odot}$ (Wegg et al., 2015a). Theoretical modelling of photometric and kinematic data (Binney & Tremaine, 2008; McMillan, 2011; Bovy & Rix, 2013; Licquia, 2016) predicts that the disk scale length R_d value of the Milky Way varies from 2 to 3 kpc. The rotation curve was obtained from McGaugh (2018). We find that the FB parameter at disk scale length ranges from 0.29 to 0.53 for the given range of disk scale length. If the Milky Way is a barred spiral galaxy then the disk scale length should be greater than 2.7 kpc in order to satisfy the bar formation criterion discussed above.

Having explored the FB criterion for the Milky Way galaxy, we next examine the distribution of morphological classes for our sample of barred galaxies to see over what types of bulge dominated galaxies the criterion ($FB < 0.35$) holds. Our sample includes 12 S0 galaxies and 27 Spiral galaxies. The FB parameter is plotted separately for Spirals and S0 galaxies in Fig. 4.3. The plot clearly shows that there is a larger fraction of Spirals compared to S0 galaxies that have lower values of the FB parameter. This can be attributed to the presence of massive bulges in S0 galaxies compared to regular spirals which make the FB values larger for the S0 class compared to Spirals.

The results of Fig. 4.3 agrees with the earlier study of local barred fractions in different morphological classes (Aguerri et al., 2009). It must be noted that lower values of FB correspond to less massive bulges as shown in equation [4.1]. This agrees with the presence of massive bulges in barred S0 galaxies and smaller fractions of bars in S0 galaxies (Barway et al., 2016). It also agrees with the lower fraction of barred giant low surface brightness galaxies (LSBGs) that often have massive bulges (Honey et al., 2016).

Fig. 4.4 shows the bar radius which is a proxy for bar strength against the galaxy type which is quite interesting in the line of earlier studies (Elmegreen & Elmegreen, 1985; Menéndez-Delmestre et al., 2007; Barway et al., 2011). These studies claim that bars tend to be stronger in early-type galaxies, which is exactly what we observe in our sample galaxies. Recent observations (Buta et al., 2010) have also shown that stronger bars are rare in S0s in comparison with Spirals which we confirm in our study. We have also looked at absolute bar fractions in S0, early type and late-type Spiral galaxies of our sample which corresponds to 0.31, 0.38 and 0.31 respectively. These fractions are not in agreement with a recent study (Barazza et al.,

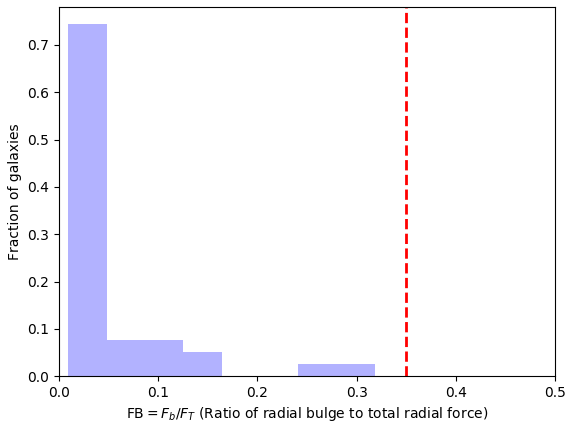

Fig. 4.2 Distribution of galaxies given according to the ratio FB i.e. ratio of radial bulge force to total radial force. The bar formation criteria from simulations corresponds to a value of 0.35 which is shown by red-dashed vertical line.

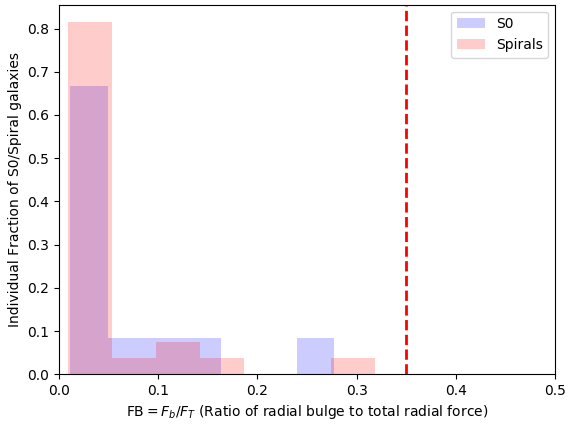

Fig. 4.3 Distribution of bar criterion FB in different morphological groups namely S0 and spiral galaxies. The bar formation criteria from simulations corresponds to a value of 0.35 which is shown by vertical red-dashed line.

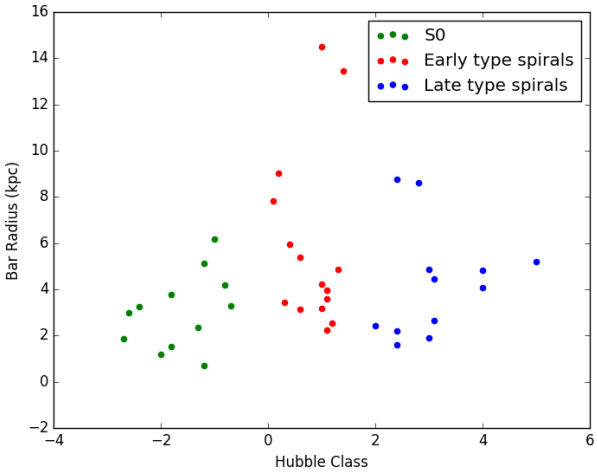

Fig. 4.4 Bar radius plotted against the Hubble class for our sample galaxies.

2008) comprising a large sample which claims higher bar fractions in late-type Spiral galaxies compared to early-type ones. As our sample is not suitable for bar fraction study because of the small sample size, therefore, we are not able to confirm earlier results of bar fractions.

The simulations of KD2018 show that the central mass concentration in a disk galaxy makes it kinematically hotter i.e. increases the velocity dispersion of disk stars. This can adversely affect bar formation as a bar will not form in a hot disk. The effect of the bulges on a disk not only depends on its mass, but also on the bulge concentration. In this study we have not studied the observational effect of bulge concentration on our criterion because of different definitions of concentration in simulations(KD2018) and observations(Barway et al., 2016). A more detailed observational study which will include wide sample containing barred and unbarred galaxies, is needed to test the effect of bulge mass and concentration in the line with simulated results (KD2018). However, our preliminary test of the theoretical bar formation criterion (Fig. 4.2) shows clearly that the effect of bulge mass within disk scale length is an important result for understanding bar formation in galaxies.

4.4 Summary

The primary motivation for the work presented here was to test the bar formation criterion given by KD2018 to an observational data set. We started this study with a sample of 100 barred galaxies for which bulge, bar and disk decomposition is given in literature (Salo et al., 2015). We have finally used 39 barred galaxies for the study, due to the constraints on the classical

nature of bulges, simulation sample matching criteria and the availability of rotation curves. We find that all the barred galaxies in our sample follow the theoretical bar formation criterion.

In future, this study can be improved by using precise rotation velocities at disk scale lengths using Integrated Field Unit (IFU) data, as IFU data can provide the rotation velocities at all radii. This is especially important for galaxies that do not have a strong gas component and for which HI or CO rotation curves are not possible to obtain. A much broader study of the bar formation criterion to disk galaxies by calculating the FB constant will improve our understanding of why bars form in some galaxies but not in all galaxies.

4.5 Caveats of the Study

Our study is limited by the choice of a constant ratio of disk to dark matter components which is not the case in observations. The bar formation criterion mentioned in this work should be valid for the galaxies which have recently formed the bar because in our simulations this criterion is calculated for initial parameters of galaxies. This is also important as our simulation does not have gas component which affects bar formation mechanism i.e bar strength evolution with time etc. Apart from these caveat, it must be noted that the initial velocity dispersion of stars in the disk depends on several physical processes such galaxy interactions, galaxy mergers, heating by spiral arms and giant molecular clouds. These effects are not included in our simulations. Therefore, the bar formation criterion should be valid for relatively isolated galaxies only. In future, we plan to extend the bar formation criterion to include the effect from the physical processes mentioned above.

Table 4.1 Details of parameter for our galaxy samples

Galaxy name	Type	V_{rot}	R_d(kpc)	M_{Bulge}	F_b	Source
ESO027-001	SBc	88.63	4.13	13.985	0.037	Hyperleda
NGC0254	S0-a	148.49	2.9	12.428	0.032	Hyperleda
NGC0615	Sb	199.13	3.05	12.819	0.020	(Staveley-Smith & Davies, 1987)
NGC0718	Sa	155.4	2.89	12.677	0.030	Hyperleda
NGC1022	SBa	143.12	2.095	12.269	0.047	(Kilborn et al., 2009)
NGC1291	S0-a	200	7	9.112	0.025	(McGaugh et al., 2000)
NGC1367	Sa	278.84	3.29	12.382	0.011	(Waugh et al., 2002)
NGC2962	S0-a	244.1	3.67	12.722	0.019	(Giovanardi et al., 1983)
NGC2968	Sa	129.47	3.06	11.905	0.079	(van Driel et al., 2016)
NGC3489	S0-a	144	0.9	11.2	0.107	(Sun et al., 2013)
NGC3507	SBb	85.11	1.83	13.754	0.024	(van Driel et al., 2016)
NGC3626	S0-a	196.76	2.23	11.939	0.033	(Bottinelli et al., 1996)
NGC3627	Sb	202.95	2.39	10.882	0.025	(Bottinelli et al., 1996)
NGC3705	SABa	209.97	1.51	13.012	0.021	(Bottinelli et al., 1996)
NGC4045	Sa	344.49	3.49	12.586	0.009	(Bottinelli et al., 1996)
NGC4133	SABb	166.1	1.21	13.904	0.019	Hyperleda
NGC4203	E-S0	343.5	2.14	11.314	0.011	(Bottinelli et al., 1996)
NGC4355	SABa	46.97	1.78	13.83	0.319	Hyperleda
NGC4457	S0-a	85.94	2.54	10.896	0.119	(Bottinelli et al., 1996)
NGC4754	S0	171.44	3.63	11.134	0.036	Hyperleda
NGC4818	SABa	123.55	2.14	12.327	0.020	Hyperleda
NGC4856	S0-a	200.71	2.97	11.244	0.043	(Bottinelli et al., 1996)
NGC4897	Sbc	168.1	3.65	13.726	0.022	Hyperleda
NGC5101	S0-a	123.7	6.29	11.227	0.100	(Bottinelli et al., 1996)
NGC5195	SBa	120.26	3.12	10.122	0.048	Hyperleda
NGC5205	SBbc	160.75	2.63	13.734	0.021	(Bottinelli et al., 1996)
NGC5338	S0	80.71	1	14.574	0.016	(Bottinelli et al., 1996)
NGC5377	Sa	202.39	6.9	11.732	0.026	(Bottinelli et al., 1996)
NGC5443	Sb	167.57	3.87	13.608	0.014	Hyperleda
NGC5448	Sa	215.44	6.04	12.517	0.017	(Bottinelli et al., 1996)
NGC5473	E-S0	157.96	2.42	12.299	0.085	Hyperleda
NGC5689	S0-a	201.64	5.08	12.08	0.039	(Bottinelli et al., 1996)
NGC6278	S0	105.14	3.04	13.007	0.16	(Bottinelli et al., 1996)
NGC7280	S0-a	135.71	2.53	13.23	0.021	(Bottinelli et al., 1996)
NGC7465	S0	85.71	1.08	13.092	0.278	(Bottinelli et al., 1996)
NGC7552	Sab	119.53	3.32	11.087	0.149	(Bottinelli et al., 1996)
NGC7731	SBa	96	2.73	14.839	0.033	(Bottinelli et al., 1996)
UGC08756	Sa	141.59	1.41	13.833	0.025	(Courtois & Tully, 2015)
NGC4569	S0-a	250	2.53	11.22	0.024	(Sofue et al., 1999)

Somewhere, something incredible is waiting to be known

Carl Sagan

5

The Effect of Bulge Mass on Bar Pattern Speed

As we have seen in the previous chapters, bar formation and evolution depends on the bulge masses in the galaxies. In this chapter we explore the effect of bulge masses on the pattern speeds of the bar.

It is well known that both bar and bulge properties in disk galaxies change significantly from early to late type spirals along the Hubble Sequence (Laurikainen et al., 2007; Binney & Tremaine, 2008). Bars in early type spirals appear to be longer and have a more uniform intensity relative to late type spirals. Their luminosity profiles appear to be flat (Díaz-García et al., 2016). This could be due to an excess of old and young stars at the bar ends, presumably due to 4:1 resonance crowding (Elmegreen, 1996). Bars in late type spirals, however, have exponential profiles. Another difference is that bars in early type spirals generally extend out to corotation radii whereas bars in late type spirals are shorter and extend out to the Inner Lindlblad Resonance (ILR) radii only (Elmegreen & Elmegreen, 1985).

The bulges in disk galaxies also show a similar variation along the Hubble Sequence. Bulges in early type spirals are more luminous and more massive than those in late type spirals and the bulge to disk luminosity ratio B/D decreases from early type to late type spirals (Laurikainen

et al., 2007; Graham & Worley, 2008). The value of log(B/D) for early type galaxies (Sa-Sb) is -0.49 while for late type galaxies (Sc-Sm) it is -1.40. Thus early type spirals have long, bright bars associated with massive bulges, whereas the later type spirals have relatively shorter bars and their galaxies have smaller bulges. This correlation suggests that bar formation and evolution must be related with bulge mass (Gadotti, 2011).

In chapter 2 we examined how bulge mass affects bar formation (Kataria & Das, 2018) (hereafter KD2018). We found that for a given disk scale length, bars are more difficult to form in disks with massive bulges and the bar pattern speed (Ω_p) increases with bulge mass. The gravity of the central bulge can affect the bar pattern speed. This is clearly shown in Fig. 8 and Fig. 12 of KD2018. In this chapter we present a more detailed study of how bulge mass affects Ω_p and especially its evolution with time ($d\Omega_p/dt$). There have been several theoretical studies that indicate that Ω_p slows down over time. Lynden-Bell (1979) discussed that bars capture orbits as they evolve and transfer angular momentum from the inner to the outer parts of their disks. This takes place along the spiral arms in the disk. As a result a spiral structure can produce torques which reduces the pattern speed of a bar and increases bar eccentricity. Due to this slowdown of the bar, the corotation and outer lindblad resonance (OLR) radii increases. The dynamical friction (Chandrasekhar, 1943) of massive dark matter halos on bars has also been shown to be an important factor in the slowdown of bar pattern speeds (Sellwood, 1980; Weinberg, 1985; Debattista & Sellwood, 1996). The frictional drag can be due to the gravitational wake caused by the bar but resonances between the halo and bar orbits also plays a role in slowing down the bar pattern speed (Weinberg & Katz, 2007b).

A massive bulge may also have a similar effect as a dark halo on Ω_p with respect to angular momentum transfer. Bars transfer a significant amount of angular momentum to their bulges (Saha et al., 2012; Saha, 2015; Kataria & Das, 2018). In the process bulges can gain spin but the net increase depends on the mass of the bulges (Saha et al., 2016). The variation of Ω_p with galaxy type has also been studied numerically and the results indicate that bars in early type galaxies with prominent bulges have higher pattern speed (Combes & Elmegreen, 1993).

The most commonly used observational technique to determine Ω_p is the Tremaine-Weinberg method (Tremaine & Weinberg, 1984b), which uses a widespread tracer population such as old disk stars (Guo et al., 2019). There are other methods such as those that use the cold gas kinematics (Weiner et al., 2001; Rand & Wallin, 2004; Piñol-Ferrer et al., 2014) or the location of rings around bars (Fathi et al., 2009). The bar morphology in photometric images at different wavelengths can also constrain Ω_p (Seigar et al., 2018). One of the key morphological indicators of bar pattern speed is the ratio of corotation radius to bar length ($\mathscr{R}$). It is used to indicate whether a bar is fast or slow. A bar is termed fast if $\mathscr{R} > 1.4$ and slow if otherwise. Some observational studies indicate that nearly all bars, regardless of the galaxy

Hubble type, are fast bars (Aguerri et al., 2015), whereas others suggest that $\mathscr{R}$ depends on the galaxy morphology (Rautiainen et al., 2008) as well as the dynamical age of the bar (Gadotti, 2011). The observational results of Ω_p suggest that it is not just galaxy and bar morphology that plays a role in constraining Ω_p, the secular evolution of bars maybe important as well. Simulations are one of the only ways in which to study this evolution. Cosmological simulation (Algorry et al., 2017) with ΛCDM cosmology show that bar should be slower, in contradiction with observations mentioned above.

In this study we use N-body simulations to study the effect of bulge mass on bar pattern speeds. Our aim is to see if there is a correlation of the decrease in Ω_p with bulge mass in disk galaxies. Since a bar is a global instability its evolution can be studied better with N-body simulations (Sellwood, 1980; Combes & Sanders, 1981; Efstathiou et al., 1982; Sellwood & Sparke, 1988; Athanassoula & Misiriotis, 2002; Athanassoula, 2003; Valenzuela & Klypin, 2003; Machado et al., 2012; Saha & Naab, 2013; Long et al., 2014; Kataria & Das, 2018). In the following sections we describe the numerical methods which are used for generating initial condition and then the disk evolution. In section 5.2 we present the main results from our simulations of the variation of bar Ω_p with bulge mass, the change in bar properties and the angular momentum transfer between bulge, disk and halo. In section 5.3 we discuss the main implications of our work for understanding the evolution of Ω_p in galaxies.

5.1 Modeling and Evolving Galaxies

5.1.1 Initial Conditions of model galaxies

We have generated our initial galaxy models using GalIC (Yurin & Springel, 2014). In all of our initial models we have used 10^6 dark matter halo particles, 10^5 disk particles and 5x10^4 bulge particles.

For this study we have generated 5 models that have compact disks and concentrated bulges, hence the bar instability is triggered within a couple of Gyrs of evolution as shown in our earlier work (KD2018). The details of the models are given in Table 5.1. The total mass of each individual galaxy is equal to 63.8 x$10^{10} M_{\odot}$. This mass corresponds to the virial velocity of the halo which is equal to 140 Kms^{-1} (Springel et al., 2005). For our models, the ratio of halo, disk and bulge particle masses varies from 1:1.12:0 in Model 1 to 1:1.4:0.23 in Model 5. Also, all the bulges are initially non-rotating. The disks are locally stable as the value of the Toomre parameter Q is greater than 1. The Toomre factor varies with radius and is given by $Q(r) = \frac{\sigma(r)\kappa(r)}{3.36G\Sigma(r)}$. Here $\sigma(r)$ is the radial dispersion of disk stars, $\kappa(r)$ is the epicyclic frequency of stars and $\Sigma(r)$ is the mass surface density of the disk.

Table 5.1 Initial Disk Models with increasing bulge masses

Models	$\frac{M_B}{M_D}$	$\frac{M_B}{M_T}$	$\frac{M_D}{M_T}$	$\frac{M_H}{M_T}$	$\frac{R_b}{R_d}$	$Q(R_D)$	M_B $[10^{10}M_\odot]$
Model 1	0	0	0.1	0.9	0	1.077	0
Model 2	0.05	0.005	0.1	0.895	0.169	1.198	0.32
Model 3	0.1	0.01	0.1	0.89	0.174	1.123	0.64
Model 4	0.15	0.015	0.1	0.885	0.175	1.460	0.96
Model 5	0.2	0.02	0.1	0.88	0.180	1.171	1.28

Column(1) Model name (2) Ratio of bulge to disk mass (3) Ratio of bulge to total galaxy mass (4) Ratio of disk to total galaxy mass (5) Ratio of halo to total mass (6) Ratio of half mass bulge radius to disk scale length(R_b/R_d) (7) Toomre parameter at disk scale length R_d(8) Bulge mass

The profile of all the galaxy components namely dark matter halo, disk and bulge are given in chapter 1. Here we see that the bulges are cuspy which will allow an ILR to form at any bar pattern speed. Therefore it will prohibit swing amplification as predicted by linear theory (Binney & Tremaine, 2008). It has been shown that the effect of cuspy bulges is that the ILR disappears in thick disks (Polyachenko et al., 2016), which is the case in the present work. Apart from disk thickness there are other factors like nonlinear processes (Widrow et al., 2008) and the inner Q barrier (Bertin, 2014) which can put off the effect of an ILR.

Fig. 5.1 shows the initial and final rotation curves as well as the variation of initial surface density and initial Toomre parameter with radius for all of our models. We see that the inner part of the rotation curve rises with increase in bulge mass fraction which is not the case for the final evolved models which we discuss in section 5.2.6. Fig 5.2 shows the contribution of individual components i.e. bulge, disk and halo to the total rotation curves. As expected the contribution of the bulge component to the rotation curve increases as we keep on increasing bulge fraction. We also plot the radial velocity dispersion of the disk particle in Fig. 5.3 which shows that the inner disk velocity dispersion increases with increasing bulge mass fraction.

5.1.2 Simulation Method

We evolved all the initial galaxy models using the GADGET-2 code (Springel, 2005). We have evolved our galaxy models up to 9.78 Gyr for conducting our pattern speed study. The opening angle for the tree is chosen as θ_{tot} =0.4. The softening length for halo, disk and bulge components have been chosen as 30, 25 and 10 pc respectively. We have taken the values of the time step parameter to be $\eta <= 0.15$ and force accuracy parameter $<= 0.0005$ in most of the simulations. As a result in all of our models, the angular momentum is conserved to within 1 %

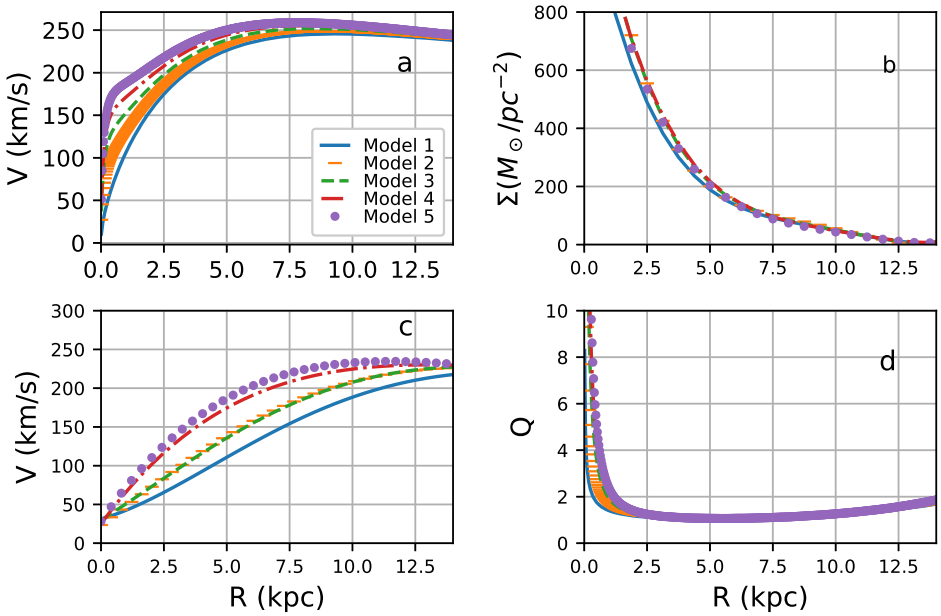

Fig. 5.1 a) The initial rotation curves of the stellar disk; b) the initial disk surface density; c) the final rotation curve at 9.78 Gyr; d) the Toomre parameter variation with radius for all the models

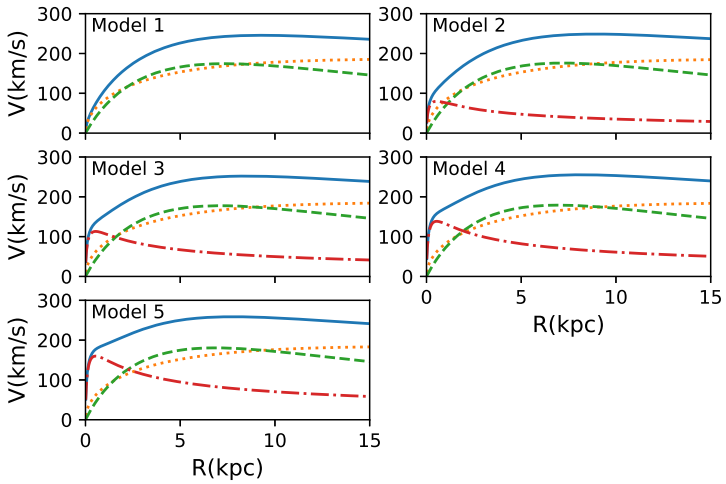

Fig. 5.2 The above plots represents the rotation curves for all of our models. The solid line is the total rotational velocity due to all the components and the rotation velocity due to the individual components is also shown. In all the plots the halo is a dotted line; the disk is a dashed line; the bulge is a dash-dot line.

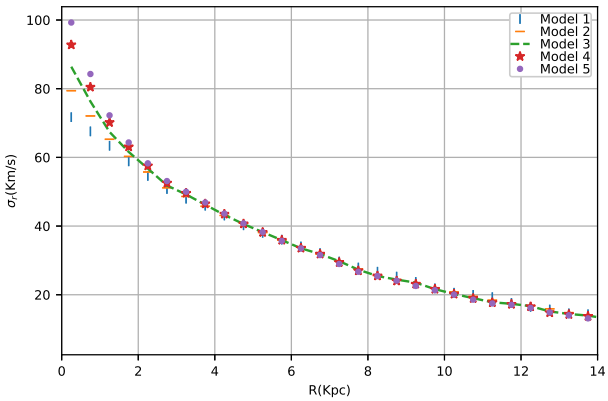

Fig. 5.3 Initial disk velocity dispersions for all the models

of the initial value. We have conducted the experiment with 1.1 x 10^6 and 2 x 10^6 particle for the model 1 to check bar growth time scales. We find that the growth of a bar does not depend on the number of particles as shown in Figure 5.4. We have also plotted the bar pattern speed in Figure 5.5 which also shows a similar behaviour for increasing number of particles. Therefore we finally used 1.15 x 10^6 particles for all the simulations in this study.

5.1.3 Bar strength and Pattern Speed

Bar strength has been defined in different ways in the literature for N-body simulations (Combes & Sanders, 1981; Athanassoula, 2003). In our study for defining bar strength we have used the mass contribution of disk stars to the m=2 fourier mode.

$$a_2(R) = \sum_{i=1}^{N} m_i \cos(2\theta_i) \qquad b_2(R) = \sum_{i=1}^{N} m_i \sin(2\theta_i) \tag{5.1}$$

where a_2 and b_2 are defined in the annulus around the radius R in the disk, m_i is mass of i^{th} star, θ_i is the azimuthal angle. We have defined the bar strength as

$$\frac{A_2}{A_0} = max\left(\frac{\sqrt{a_2^2 + b_2^2}}{\sum_{i=1}^{N} m_i}\right) \tag{5.2}$$

The above method of bar strength calculation has also been used in observations (Buta et al., 2006), where bar strength has been calculated from the optical and near-infrared (NIR) images of disk galaxies (Das et al., 2008). As in our simulations, the bar strength is derived from the variation of Fourier modes with radius in a galaxy.

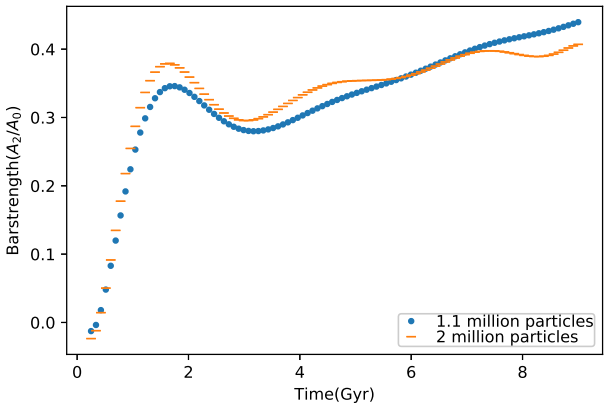

Fig. 5.4 Bar strength evolution of Model 1 for 1.1 and 2 million particles in the simulations. A comparison of the two curves shows that the time of growth of a bar does not depend on the number of particles.

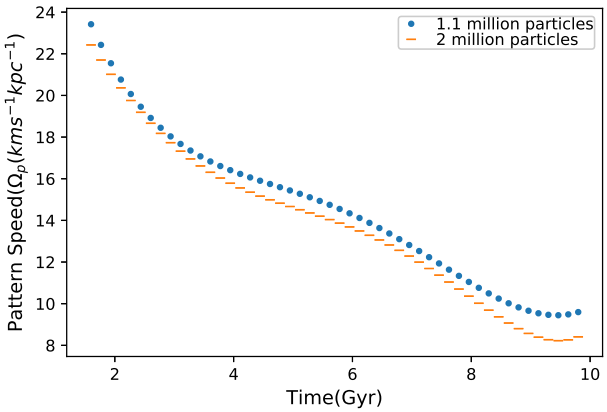

Fig. 5.5 Pattern speed evolution of Model 1 for 1.1 and 2 million particles

We calculated the pattern speed (Ω_P) of the bar by measuring the change in phase angle $\phi = \frac{1}{2}\tan^{-1}\left(\frac{b_2}{a_2}\right)$ of the bar. This is calculated using the Fourier component in concentric annular bins throughout the disk of the galaxy. We used annular regions of width 1 kpc for disk particles only. The measured pattern speed corresponds to the bin which has the maximum value of m=2 mode i.e. bar strength.

5.1.4 Angular Momentum Calculation

The total angular momentum of the different components of a galaxy i.e. disk, bulge and halo, are measured separately. The angular momentum of a particle is calculated from the product of its mass, radial distance from galactic center and circular velocity, where the radial distance is calculated about the rotation axis of the galaxy. The time evolution of the total angular momentum of each component of the galaxy models has been discussed in section 5.2.6.

5.1.5 Ellipticity Calculation

We have used the *ellipse* task in the IRAF code to measure the bar ellipticity for all our galaxy models (Honey et al., 2016). The initial definition of ellipticity as used by IRAF is given by

$$\varepsilon = 1 - \frac{b}{a} \tag{5.3}$$

where b is the semi-minor axis and a is semi-major axis.In this research we have used *PHOTUTILS* (10.5281/zenodo.2533376), but instead of using the IRAF tasks we have used a python module of *Ellipse*.

Before starting this analysis we have converted the output binary files produced by GADGET code to FITS file format (Pence et al., 2010), which is compatible with IRAF/PHOTUTILS. To do this we generated a spatial grid in the x-y plane that has 93 bins in each direction. Then the disk particles were distributed among each of the pixels. The *Ellipse* task fits ellipses of increasing major axis length. We have maintained a common center for all the ellipses, which is the galaxy optical center. The position angle corresponding to each fitted ellipse remains constant until the major axis of an ellipse matches with that of the bar radius (or major axis), after which the elliptical isophotes become progressively rounder as the disk luminosity becomes more prominent. We have defined the bar ellipticity to correspond to constant position angle within a margin of 10 degree such that there is a sharp decrease in ellipticity by 20%. We have defined these values as ε_{sce}.

5.1.6 $\mathscr{R}$ parameter calculation

$\mathscr{R}$ is the ratio of corotation radius (R_{CR}) to bar radius (R_b). We calculated the corotation radius by determining the distance of the lagrange point(L1/L2) from the center of the galaxy. At the lagrange point, the effective force is zero since the gravitational force balances the centripetal force in the bar rotating frame (Debattista & Sellwood, 2000). We have divided the galaxy into annular bins of constant radial widths. Then for each bin we calculated the gravitational pull along the bar major axis using the potential gradient values and the centripetal force in the bar rotating frame using the Ω_p value and radius of bin. The corotation radius was then taken to be the radius at which these two forces balance each other.

There are several definitions given in the literature of the measurement of bar length. These definitions correspond to the variation of the ellipticity and position angle (PA) of the fitted isophotes, which were fitted using the *ellipse* function. In the following paragraph we describe the different definitions for the semi-major bar length a_{max}, a_{min} and a_{10}.
1. a_{max} corresponds to maximum ellipticity for $\Delta PA < 10$. (Erwin, 2005; Marinova & Jogee, 2007)
2. a_{min} corresponds to minimum ellipticity for $\Delta PA < 10$. (Erwin, 2005; Zou et al., 2014)
3. a_{10} corresponds to $\Delta PA = 10$ (Erwin & Sparke, 2003; Zou et al., 2014).
In above definitions a_{max} under estimates the actual bar length while a_{min} over estimates the bar length. In our study a_{10} is not suitable as we are studying galaxies where the phase-angle changes sharply as we move from bar to disk isophotes or phase-on bars. We also noticed that as we fitted isophotes with increasing radii (Fig. 5.6), in a few of cases the ellipses become rounder in the outer region but the PA still remains the same. This is because the position angle of the circles are ill defined. Therefore we have taken the bar length to correspond to the radius where the ellipticity changes sharply by 20% or more (ε_{sce}). All the values of the final bar lengths are listed in Table 5.2 according to all three definitions.

5.2 Results

5.2.1 Pattern Speed (Ω_p)

The Ω_p evolution for all the models have been shown in Fig. 5.7. We have plotted the pattern speed only after the bar has formed. We set a cutoff on bar strength $A_2/A_0 = 0.2$ which is taken to be the starting point of bar formation. The bar formation timescales for Model 1, Model 2, Model 3, Model 4 and Model 5 are 1.2 Gyr, 1.2 Gyr, 2 Gyr, 2.5 Gyr and 3.96 Gyr respectively. The $d\Omega_p/dt$ has a very different form for the bulgeless galaxy (Model 1) compared to other models. The $d\Omega/dt$ falls rapidly and reaches a stable value for Model 1 but shows an increase

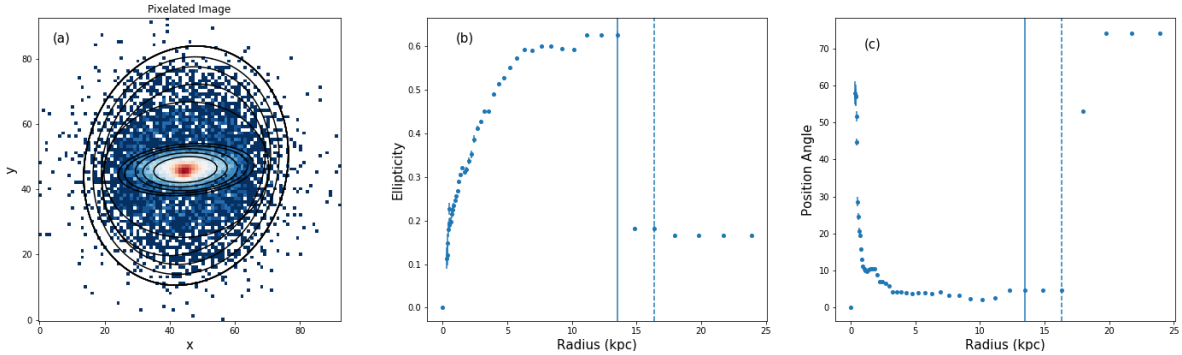

Fig. 5.6 (a) Fitted isophotes with increasing radii Model 2 at 6 Gyr (b) Ellipticity of isophotes with increasing semi major axis of ellipses (c) Position angle (PA) of fitted ellipses with semi major axis. Here the vertical solid line represent bar length corresponding to a_{max} and a_{sce} definitions while dashed vertical line represent bar length corresponding to a_{min} definition.

Table 5.2 Bar length and ellipticity calculation using various definitions at t=9.78 Gyr in all the models

Model	a_{min}	a_{max}	a_{sce}	ε_{min}	ε_{max}	ε_{sce}
Model 1	17.15	14.19	14.19	0.13	0.748	0.748
Model 2	14.19	13.55	13.55	0.077	0.641	0.641
Model 3	18.06	15.48	16.77	0.03	0.637	0.637
Model 4	16.125	16.125	16.125	0.63	0.63	0.63
Model 5	14.19	10.97	14.19	0.52	0.623	0.6

Column(1) Model name (2) a_{min} which corresponds to maximum ellipticity within ΔPA <10 (3) a_{max} which corresponds to minimum ellipticity within ΔPA <10 (4) a_{sce} which corresponds to sharp change in ellipticity by 20% of previous value (5) Ellipticity corresponding to a_{min} (6) Ellipticity corresponding to a_{max} (7) Ellipticity corresponding to a_{sce}.

Table 5.3 $\Delta\Omega_p$ values for models with increasing bulge masses

Model	$\Delta\Omega_p$	initial R_{CR}	initial R_b	initial $\mathscr{R}$	final R_{CR}	final R_b	final $\mathscr{R}$
Model 1	-16.98	9.275	8.39	1.16	25.25	14.48	1.74
Model 2	-20.94	7.75	6.45	1.20	24.25	14.19	1.71
Model 3	-24.85	7.4	5.72	1.29	23.25	15.48	1.50
Model 4	-25.70	7.7	6.45	1.19	22.75	16.13	1.41
Model 5	-26.11	6.75	5.71	1.18	17.75	14.19	1.25

Column(1) Model name (2) $\Delta\Omega_p$ value (3) initial value of the co-rotation radius R_{CR} (4) initial value of bar radius R_b (5) initial value of $\mathscr{R}$ where $\mathscr{R} = \mathscr{R}_{\mathscr{C}\mathscr{R}}/\mathscr{R}_{\lfloor}$ when the bar just formed (6) final value of co-rotation radius R_{CR} (7) final value of the bar radius R_b (8) final value of the $\mathscr{R}$ for models evolved up to 9.78 Gyr.

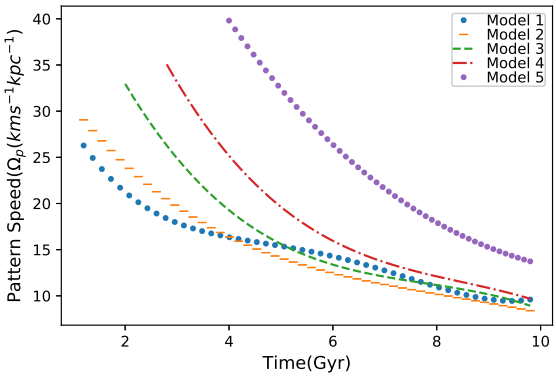

Fig. 5.7 Pattern speed evolution of all the models with time

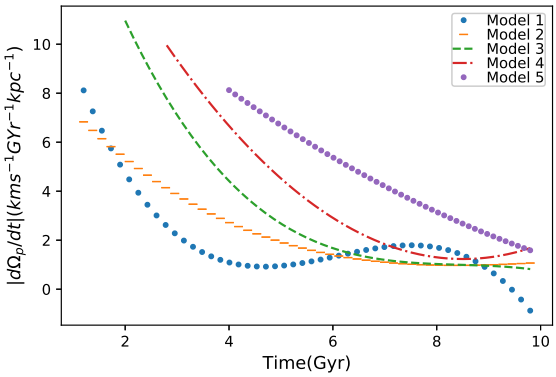

Fig. 5.8 The absolute value of Rate of change in pattern speed of bar with time for all the models

in $d\Omega_p/dt$ after 6 Gyr which is not the case for other models. This correlates with faster increase in bar strength of Model 1 compared to other models that have bulges as shown in Fig. 5.9. Model 1 is the only disk without a bulge and so the dynamical friction of a bulge does not affect its pattern speed evolution. Hence, the evolution of $d\Omega_p/dt$ is unlike the other models. Thus, as shown in Fig. 5.8 a bulge clearly has a significant effect on Ω_p.

For the other models with bulges, it is clear that the initial bar pattern speed increases with increasing bulge mass (Fig. 5.7). As the bars start evolving, the pattern speed decreases with time for all the models. We have plotted the rate of change in pattern speed ($d\Omega_p/dt$) in Fig. 5.8. It is clear that the absolute value of the initial rate of $d\Omega_p/dt$ is larger for models with larger bulge masses as the slope of the curves becomes steeper with increasing bulge mass.

5.2.2 $\Delta\Omega_p$: Total change in pattern speed

We have also quantified the total change in bar pattern speed since the bar formed and the parameter is given by:

$$\Delta\Omega_p = \int \frac{d\Omega_p}{dt} dt \tag{5.4}$$

This quantity is an estimate of total change in bar pattern speed from the beginning stage of its formation to the final evolved state and is shown in Table 5.3. We can clearly see from Table 5.3 that the absolute value of the decrease $\Delta\Omega_p$ increases with increase in bulge mass. This can be related to the high rate of decrease in pattern speed for massive bulges as shown in Fig. 5.8. Physically this can be interpreted as a result of the dynamical friction exerted on the bar by the bulge. The effect increases with more massive bulges. It is similar to the dynamical friction of the other spherical component, the halo, on the bar (Chandrasekhar, 1943).

5.2.3 $\mathscr{R}$ parameter

The $\mathscr{R}$ parameter is a measure of how fast a bar is rotating with respect to the disk. Fast bars correspond to $\mathscr{R}$ <1.4 while slow bars have $\mathscr{R}$ >1.4. We see in our simulations that the models initially have $\mathscr{R}$ <1.4 as shown in Table 5.3 which means that all the initial bars are fast. As we evolve our models up to 9.78 Gyr, we find that except for Model 5 which has the most massive bulge, the bars in all other models become slow and have $\mathscr{R}$ >1.4. The bar slowdown is due to the dynamical friction of the bulge, as mentioned earlier in section 5.2.2. But the bar slowdown is not so prominent in Model 5 because the bar in Model 5 has formed very late and hence the bar has not had enough time to slowdown despite facing the maximum dynamical friction due to the bulge, which is the most massive amongst all the models. Also, despite the early formation of a bar in Model 1, the Ω_p does not suffer as much slowdown as the other models (Table 5.3). This is because model 1 does not have a bulge and hence does not experience the dynamical friction.

5.2.4 Bar Formation Timescale and Bar Strength

We have traced the evolution of bar strength with time for increasing bulge to disk mass ratios (Fig. 5.9). We find that the bar forms very early at $t \sim 1.5$ Gyr for the bulgeless model (Model 1). But as the bulge mass fraction increases, the bar formation timescale increases and the bar forms later. The bar formation timescale for the less massive bulge model (Model 2) is similar to that of the bulgeless model (Model 1). The most massive bulge model (Model 5) forms a bar around $t \sim 3.96$ Gyr. This is because a more massive bulge in a galaxy center makes a galaxy potential deeper and the disk kinematically hotter. Hence, it becomes more difficult for a bar to

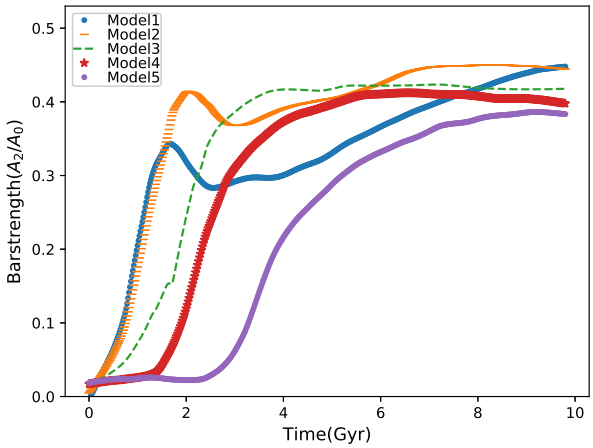

Fig. 5.9 Bar strength evolution of all the models with time

form. After the bar has formed, it goes into the secular evolution phase in all models. In this phase the bar strengths increase except for Model 3 and Model 4 where it is almost constant as the galaxy evolves. The final X-Y cross sections for all the models is shown in Fig. 5.10 where we can see that the final bars have similar morphologies. This trend matches that of the bar strength plot shown in Fig. 5.9, where nearly all the bars have similar A_2/A_0 values with only small variations. Thus increasing the bulge does not strongly affect the final bar strength as the final values vary by $A_2/A_0 <= 0.1$.

5.2.5 Bar Ellipticity

We have measured the bar ellipticity at different time intervals : 1.98 Gyr, 3.96 Gyr, 5.94 Gyr, 7.92 Gyr and 9.78 Gyr, to study how the bar ellipticity changes with time in different galaxy models. Table 5.4 shows the bar ellipticity at the above mentioned times. For the bulgeless Model 1, the ellipticity continues to increase with time. This increasing ellipticity corresponds to the continuous slowdown of Ω_p (Fig. 5.7). However, for the bulge dominated models (Model 2, Model 3, Model 4 and Model 5), the bar ellipticity increases continuously with time in the beginning but hovers around a mean value (Table 5.4) as the bar evolves. This could be because of the continuous exchange of particles and angular momentum between the bulge and the disks.

We find that the change in bar ellipticity (ε) with time correlates with the change in bar strength (A2/A0) for all of our models. We can physically interpret this correlation in the following way; as the eccentricity of the stellar orbits in the bar increases, the bar strength also increases.

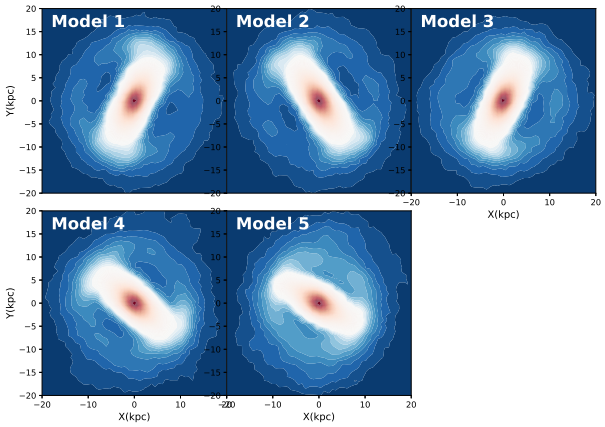

Fig. 5.10 X-Y cross section of all the evolved models at 9.78 Gyr. In this plot we have omitted bulge particle and shown only disk stars in order to focus on bar in the disk.

This is clearly seen in Figure 5.11 which shows the bar ellipticity evolution with time for all the models. We can also see that the final ellipticity of the bars at the end of the simulation decreases as bulge mass increases progressively from the bulgeless model (Model 1) to the most bulge dominated model (Model 5). This trend can be seen in bar strength values as well (Table 5.4). This is not surprising as the axisymmetric bulge makes the disk kinematically hotter and makes the bar orbits more circular (Sellwood, 1980; Athanassoula, 2003; Das et al., 2003), causing the ellipticity to decrease.

5.2.6 Angular Momentum Exchange

During disk evolution, the angular momentum of the bulge can change with time and this may affect the bar pattern speed. To investigate this we plotted the evolution of total angular momentum with time for bulge, disk and halo components for all the models in Fig. 5.12. A similar analysis was done in KD2018. We find that the angular momentum for bulge and halo components always increase with time for all the bar forming models, while the disk component always loses angular momentum. The rate of change in angular momentum of the components (bulge, disk, halo) only increases after the bar has been triggered and hence the bar is important for the angular momentum exchange. As the inner disk transfers the angular momentum to the halo and bulge components, the rotation velocities of the inner disk stars decreases, this is clearly seen in the initial and final rotation curves shown in Fig. 5.1.

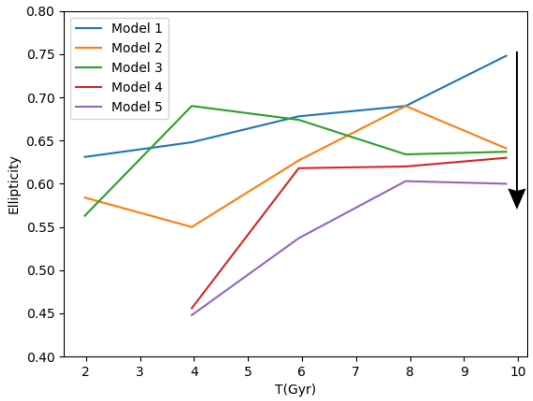

Fig. 5.11 Ellipticity evolution with time is shown for all the models. The down arrow in the figure indicates that final bar ellipticity decreases with increase in bulge mass.

Table 5.4 Ellipticity variation with time for models with increasing bulge masses

Model Name	t= 1.98		t=3.96		t=5.94		t=7.92		t=9.78	
	ε	$\frac{A_2}{A_0}$	ε	$\frac{A_2}{A_0}$	ε	$\frac{A_2}{A_0}$	ε	$\frac{A_2}{A_0}$	ε	$\frac{A_2}{A_0}$
Model 1	0.63	0.33	0.65	0.30	0.68	0.36	0.69	0.42	0.75	0.45
Model 2	0.58	0.43	0.55	0.38	0.63	0.42	0.69	0.45	0.64	0.44
Model 3	0.56	0.24	0.69	0.42	0.67	0.42	0.63	0.42	0.64	0.42
Model 4	-		0.46	0.36	0.62	0.41	0.62	0.41	0.63	0.40
Model 5	-		0.45	0.21	0.54	0.33	0.60	0.37	0.60	0.39

column(1) Model name (2) ellipticity and bar strength of bar at t=1.98 Gyr(3) ellipticity and bar strength of bar at t=3.96 Gyr (4) ellipticity and bar strength of bar at t=5.94 Gyr (5) ellipticity and bar strength of bar at t=7.92 Gyr (6) ellipticity and bar strength of bar at t=9.78 Gyr

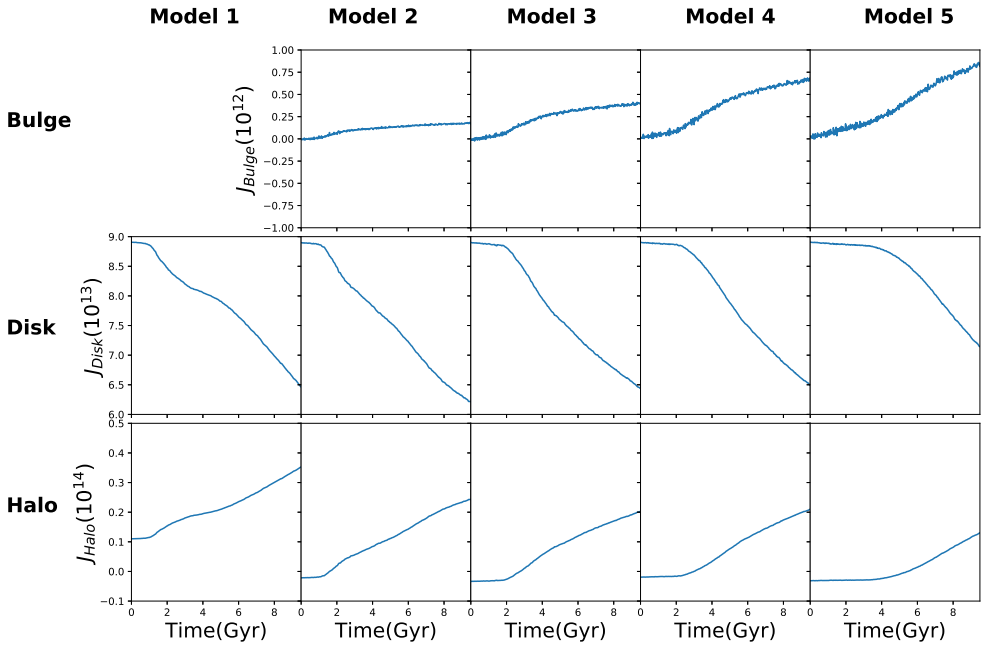

Fig. 5.12 Total Angular momentum evolution with time for individual components namely bulge, disk and halo of all the models

We can also see that total gain in angular momentum for the bulge component increases with bulge mass as we go from Model 2 to Model 5. On the other hand, the total gain in angular momentum for the halo component decreases with increasing bulge mass. This is probably because a more massive bulge captures more disk particles and hence absorbs more angular momentum from the disk. However, it should be noted that in terms of absolute values, the halo still shows the largest increase in angular momentum.

5.3 Discussion

In this section we discuss the implications of our results for observations of bars. Our simulations can explain why there is no specific correlation between bulge mass and the $\mathscr{R}$ parameter. Rautiainen et al. (2008) find that the bulge to the total disk flux (B/T) ratio is only weakly correlated to $\mathscr{R}$. Here the B/T ratio is treated as a proxy for Hubble type as suggested by previous studies (Laurikainen et al., 2007; Graham & Worley, 2008). Further, they claim that slow bars favour galaxies with low mass fraction of bulges or late type galaxies. On the other hand recent observations of Califa galaxies (Aguerri et al., 2015) find that most bars are fast

irrespective of Hubble type. What can be reason for different nature of the results in both the observations?

We think that there can be two possible explanations for larger decrease in bar pattern speed with increasing bulge mass. (1) The dynamical friction due to the halo plays an important role in the secular evolution of a bar (Tremaine & Weinberg, 1984a; Weinberg, 1985; Debattista & Sellwood, 2000; O'Neill & Dubinski, 2003; Valenzuela & Klypin, 2003; Holley-Bockelmann et al., 2005; Weinberg & Katz, 2007b,a). But Weinberg & Katz (2007b) claim that the frictional drag on a bar is mainly contributed by the ILR resonances. Therefore, the dynamical friction of a bulge on a bar must be important as the bulge lies within the vicinity of ILR region, although the overall frictional drag due to the bulge will be smaller compared to that of the dark matter halo. Apart from this we also see a significant transfer of angular momentum from the disk to the bulge which increases with increasing bulge mass (Fig. 5.12). The fact that a bar transfers a significant amount of angular momentum to a non-rotating classical bulge through ILR resonances has been discussed earlier in the literature (Saha et al., 2012). Also, when we compare the change Ω_p in a bulgeless galaxy with that of a galaxy with a massive bulge, we clearly see that the absolute change in pattern speed is higher for the disk with a massive bulge. (2) Lynden-Bell (1979) has shown that the pattern speed of a bar decreases as it evolves because it captures stellar orbits which results in the increase of bar ellipticity. This results in the slowdown of bars as shown in other studies as well (Polyachenko, 2004, 2013). This capture of bar orbits has also been shown to increase barlength (Martinez-Valpuesta et al., 2006). We see that the relative increase in ellipticity and bar length is more in massive bulge models compared to disks with less massive bulges. This can be due to larger orbit capture in the case of massive bulges compared to less massive ones. Thus, the capture of stellar orbits can contribute to the decrease in pattern speed in massive bulge models.

We can now explain the conflicting observations mentioned in the first paragraph using our simulation results. In our simulations bars that are initially fast after their formation are formed in the disks with more massive bulges. But they also tend to slowdown faster with time due to dynamical friction compared to the bars that had lower initial pattern speeds (Fig. 5.7 and 5.8). This slowdown is more prominent in galaxies with higher bulge to disk mass fractions (see Table 5.3). However, it is interesting to note that although the rate of slowdown is more in the case of high bulge mass fraction models, the final bar does not become as slow as $\mathscr{R} < 1.4$. This is because the other factor which comes into play is the bar formation timescale which increases with increase in bulge mass. The bars in the models with low bulge mass fraction, despite having a lower rate of decrease in pattern speeds, have enough time to become slow bars and reach the final value of $\mathscr{R} > 1.4$. Hence the rate of decrease in pattern speed and the timescale of bar formation play key roles in deciding whether bars are fast or slow. Thus, our

results can explain Rautiainen et al. (2008) if the observed bars are old (evolved for t≈8 Gyr) and the Califa observations (Aguerri et al., 2015) if the observed bars are young (evolved for t<1Gyr).

Studies of barred galaxies suggests that bar strength decreases with increase in central velocity dispersion of stars (Das et al., 2003) (Table 5.4). Since the latter increases with bulge mass and bulges are larger in early type spirals compared to late type spirals, it follows that bar strength should change along the Hubble Sequence. However, observations suggest that there is no correlation between bar strengths and Hubble type (Elmegreen et al., 2007). These conflicting results can be understood from the results of our simulations that show that bar strength (A_2/A_0) varies for different bulge masses but the variation changes with time (Fig. 5.9). For example at t=4 Gyr the diffrence in A_2/A_0 between the most massive and smallest bulge is 0.2 but is 0.1 at t=10 Gyr. Thus there is a clear dependence on the secular evolution of the bars as well. So the apparently conflicting simulation and observational results can be understood as due to the fact that observations catch bars at different stages of evolution. Hence, it is not surprising that the correlations of bar strength and bulge mass that we see in our simulations is not clearly seen in observations.

5.4 Summary

We have conducted an N-body study of how bar pattern speed (Ω_p) in disk galaxies varies with increasing bulge mass. We summarize the main results of our work below.

1) We find that the initial Ω_p of bars in galaxy disks increases with the bulge mass fraction.

2) We find that initial bars in all the models are fast: $\mathscr{R} < 1.4$. But as the bars evolve with time they become slower and $\mathscr{R} >$1.4. This trend reduces with increasing bulge mass.

3) Our simulations show that the rate of decreases in Ω_p is larger for larger bulge to disk mass fractions. The decrease in Ω_p can be due to several factors; the dynamical friction of the halo has the largest effect. But we show that the dynamical friction of the bulge is also important. The capture of stellar orbits may also contribute to the slowdown of Ω_p.

4) The exchange in angular momentum from disk to bulge increases with increasing bulge mass so that the most massive bulges gain the most angular momentum from the disk. This could be the reason why the bar Ω_p slows down with increasing bulge mass. On the other hand, the exchange of angular momentum from disk to halo decreases with increasing bulge mass; however, in absolute terms, the angular momentum gain by the halo is always larger than that of the bulge

5) Our simulations can explain the conflicting nature of observations of $\mathscr{R}$ which find both a correlation (Rautiainen et al., 2008) and no correlation (Aguerri et al., 2015) with bulge mass or

Hubble type. We can find these correlations if the observed bars are old (evolved for t≈8 Gyr) and no correlation is the observed bars are young (evolved for t<1 Gyr).
6) The variation of bar ellipticity with time does show a correlation with bar strength. We also find that the ellipticities of the final bars show a significant decrease with increasing bulge mass.

We are like butterflies who flutter for a day and think it is forever.

Carl Sagan

6

Role of bars in eroding cuspy halos

In this chapter we discuss the effect of angular momentum transport by bars on the density profiles of the halos. The presence of dark matter halos in galaxies has been detected from the flat rotation curves obtained with optical (Rubin et al., 1978) as well as HI observations (Bosma, 1978, 1981a,b). Theoretical studies such as those by Ostriker & Peebles (1973) have shown that galaxy disks become unstable unless they are embedded in a massive spherical potential. These early simulations indicated the existence of dark matter halos surrounding galaxies. Theoretical predictions of galaxy dark matter were later confirmed by observations of dwarf spheroidal galaxies (Faber & Lin, 1983) and elliptical galaxies (Stewart et al., 1984; Fabian et al., 1986) that are found to be surrounded by dark matter halos.

Cosmological simulations (Springel et al., 2005; Schaye et al., 2015) show that dark matter plays an important role in the formation of galaxies in the Universe. Dark matter halos provide the deep potential wells where the primordial gas falls in and forms galaxies. These simulations also confirm that dark matter halos have Navarro-Frank-White type of density profiles which vary as r^{-1} in the central region while varying as r^{-3} in the outer region (Navarro, 1995; Navarro et al., 1996, 1997). Further studies (Moore et al., 1998; Jing & Suto, 2000) have shown that the inner profiles can vary as r^{-1} to $r^{-1.5}$. This inner density profile which rises steeply in the central region is often called a “Cusp". The modeling of HI observations of dwarf

galaxies (Moore, 1994; Flores & Primack, 1994) show that there is a discrepancy between the observed rotation curves and those calculated theoretically, especially in the inner parts of the galaxies. Using galaxy rotation curves these studies show that the dark matter profile varies as r^0 in the inner parts, which is also called “halo core" while it varies as r^{-2} in the outer parts. This is typically called the pseudo isothermal profile. This discrepancy between observations and theoretical models of the inner profiles of galaxy halos is widely known as “Core-Cusp" problem of LCDM cosmology (de Blok, 2010). Studies suggest that during the epoch of galaxy formation, the infalling gas mass causes a change in the shape of the dark matter profile by making the inner potential well deeper (Moore et al., 1998). This process is commonly known as “adiabatic contraction"(Blumenthal et al., 1986) and it contracts the inner dark matter density profile by increasing the density in the inner region. This formation scenario produces halos that have inner density profiles which are also very steep and increases the discrepancy further.

6.1 Earlier studies for resolving the cusp-core problem

There have been several studies that have tried to explain this core-cusp problem. Navarro et al. (1996) suggested that baryonic processes can produce a core in the inner dark matter profile of dwarf galaxies. In their N-body study the effect of star formation has been studied on the inner baryons and the dark matter density profile. It shows that if a significant amount of baryons are injected into the center of the dark halo it can produce an inner core in the halo profile. Burkert (1995) have analysed four dwarf galaxies which have been observed by Moore (1994) and derived the rotation curves. They found that baryonic processes may not be sufficient to produce cores in the dark matter profiles as it requires fine-tuning of these processes. Their study suggested that the flat core is an intrinsic property of the dark matter halo and they defined a new dark matter halo profile called the "Burkert profile" in which the inner dark matter profile is a core (r^0) and the outer dark matter profile varies as r^{-3}.

DDO 154 has been studied in detail to understand the importance of baryonic processes in deciding the shape of the dark matter profile (Gelato & Sommer-Larsen, 1999). In this study, the authors have tried to reproduce the observed rotation curve of DD0154 by simulating a NFW halo along with violent gas outflows in the disk. They find that it is possible to reproduce the observed rotation curve if the disk can blow out 33 to 75 percent of it’s initial disk mass. This method does not use the fine tuning of baryonic processes argument (Burkert, 1995) as the observed rotation curve can be reproduced for a wide range of gas blow outs. Recent simulated dwarf galaxies (Oh et al., 2011) which includes the baryonic feedback processes have shown that the inner core profile can vary as $r^{-0.28}$ which matches the dwarf galaxy dark matter profiles obtained from the THINGS survey (Walter et al., 2008). Other numerical

studies of the evolution of isolated dwarfs that include a new scheme of feedback processes (Teyssier et al., 2013) have the following observational predictions for the nature of dwarf galaxies which have core type halo profiles a) bursty star formation history with peak to trough ratio of 5 to 10 having a duty cycle similar to dynamical timescales in the galaxy b) a hot stellar distribution with $v/\sigma \approx 1$. These observational predictions are in agreement with the isolated dwarf Wolf-Lundmark-Mellote (WLM) galaxies. The FIRE(Feedback in realistic environment) simulations (Oñorbe et al., 2015) that have a high force and mass resolution, show that the presence of cores in dwarf galaxies correlates with the history of star formation in the galaxies. A dwarf galaxy is more likely to have a core if it shows maximum star formation after $z > 2$, after the early phase of galaxy mergers has commenced. However, there is a recent study which claims (Genina et al., 2018) that different slopes of inner core profiles depend upon the viewing angle. This study has been conducted on dwarf galaxies chosen from the APOSTLE hydrodynamic simulations of the Local Group.

As Navarro et al. (1996) already point out, baryonic feedback processes will be only effective in dwarf galaxies because of their smaller masses. Since spiral galaxies are massive and hence have deep potential wells, gas feedback may not be enough to affect the inner dark matter halo profile. Other observational studies (Kuzio de Naray & Spekkens, 2011) have shown that feedback processes cannot be important for altering the central dark matter profile of dark matter dominated Low Surface Brightness (LSB) galaxies.

The cusp to core transition has been explored through several other ideas such as dynamical friction of an orbiting mass clump (El-Zant et al., 2001), AGN feedback (Teyssier et al., 2011; Martizzi et al., 2012), Supernova Feedback (Pontzen & Governato, 2012) , Bose Einstein Condensate of dark matter (Harko & Madarassy, 2012), scalar field dark matter (Robles & Matos, 2013; Tulin & Yu, 2018) warm dark matter Halo (Villaescusa-Navarro & Dalal, 2011), the sinking of massive objects(Goerdt et al., 2013) and tidal compression in mergers of puffed up satellites (Dekel et al., 2003).

Large scale global instabilities in galaxy disks are also thought to play an important role in affecting inner dark matter profile. Weinberg & Katz (2002) have shown that bars can remove cusps from the center of dark matter halo within 5 bar orbital times. This is due to the transfer of angular momentum from the Inner Lindblad Resonances (ILR) like resonance within the cusp region to the dark matter halo particles. In a later work Weinberg & Katz (2007b,a) have emphasized on the importance of the resolution of the simulation and put a limit of 10^8 as minimum number of particles. On the other hand Sellwood (2008) disagrees with this limit of 10^8 particles and claims that such angular momentum exchange does not occur even if the number of particles are 3 orders of magnitude lower than this limit. Further studies by Dubinski et al. (2009) included a large range of resolutions to resolve the core-cusp issue. Their study

claims that their results converse after 10^6 to 10^7 particles in their simulations and the dark matter halo cusp is preserved. They claim that thick bars rather than thin bars are formed and question the effect of thin bars in removing the cusp. Thin bars may also evolve into thicker bars due to buckling instability.

In this chapter we revisit the importance of bars in removing the cusps of dark matter halos using progressively higher N-body simulations. We start with an axisymmetric disk that has a cuspy dark matter halo and a disk that is bar unstable and track the cusp to core transition due to the bar. Our study is different from previous bar simulations that investigate halo properties, as we include a bulge component in our galaxy models. In the following sections we discuss the numerical techniques used to generate and evolve disk galaxies, the results and finally the implications of our study.

6.2 Modeling and Evolving Galaxies

6.2.1 Initial Condition for Galaxies

We have used the GALIC code (Yurin & Springel, 2014) to generate the initial galaxy models which contain an axisymmetric disk and halo components. We have used 10^6 halo particles for all the models but we have increased the number of disk particles i.e. 10^5, 5×10^5 and 10^6, for the increasing the resolution The models are labeled L, M and H models. We have also prepared a model with an additional bulge component having 50000 particles and similar to the low resolution model (L-bulged). The total mass of the model galaxy is 63.8 $\times 10^{10} M_{\odot}$ and the disk mass is 6.38 $\times 10^{10} M_{\odot}$. We have used a halo spin parameter of 0.035 which corresponds to the maxima of the log normal distribution of simulated dark matter halo angular momenta in cosmological simulations (Bullock et al., 2001). The disk scale length is 2.6 kpc. Figure 6.1 shows the rotation curves for all three models and also the contribution of each component. The dark matter dominates the outer regions of all the model galaxies. Figure 6.2 and 6.3 show the surface density and radial velocity dispersion of our models; both distributions fall with radius.

The density profile for all the galaxy components namely disk and halo is given in chapter 1.

We have checked that all the models are locally stable as Toomre parameter is greater than 1 for all the models through out the disk. Figure 6.4 shows the radial variation of Toomre parameters for all the initial models.

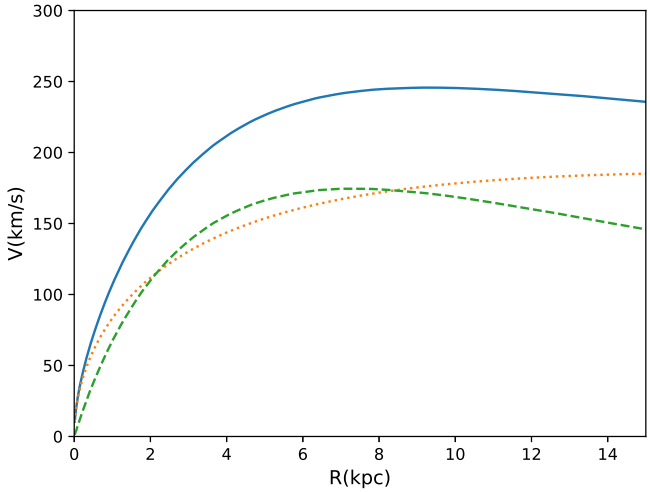

Fig. 6.1 Solid line represents the total rotation curve of the galaxy. The dashed line represents the rotation curve due to disk component while dotted line represents the rotation curve due to halo component.

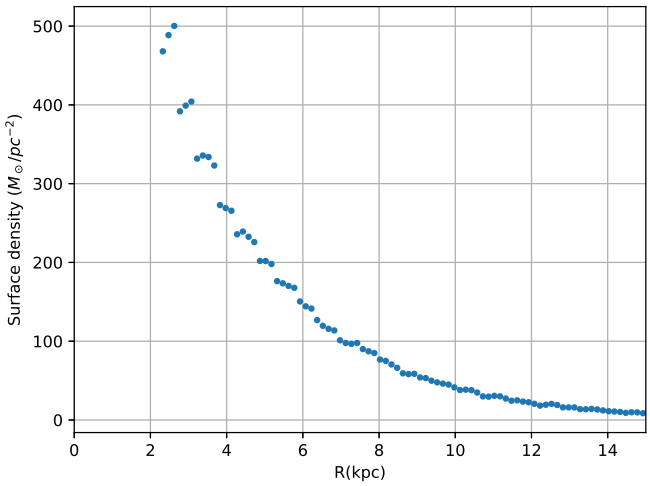

Fig. 6.2 Surface density variation as a function of radius

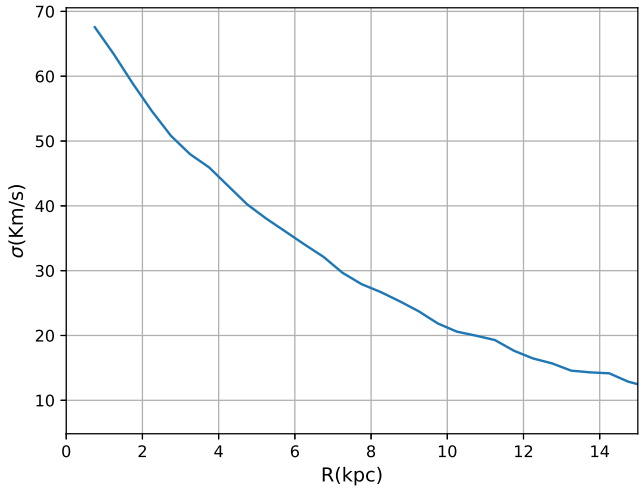

Fig. 6.3 Radial velocity dispersion for all of our models.

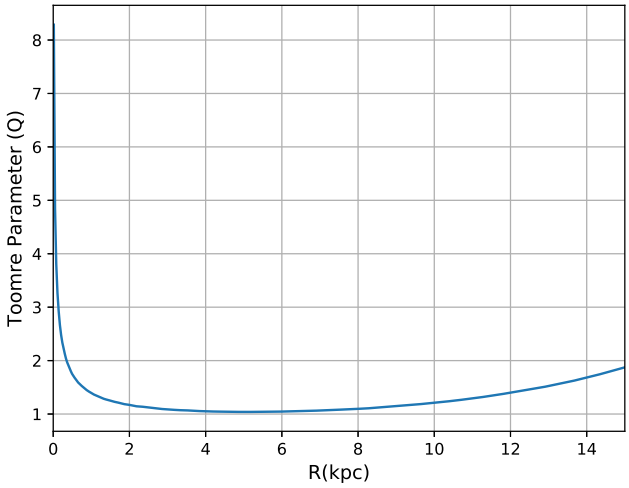

Fig. 6.4 Toomre parameter variation with radius in the initial models

6.2.2 Simulation Method

Once the initial disk galaxies were generated, we evolved them with the GADGET-2 code (Springel, 2005) for 4 Gyr to 8 Gyr to see how the mass distribution of the halos changes with time. The opening angle for the tree is chosen as θ_{tot} =0.4. The softening length for halo, disk and bulge components has been chosen 30, 25 and 10 pc respectively. After fine tuning the simulations parameters we see that the angular momentum is conserved within 0.2 % of the initial values. More details about the paramenters in given in chapter 1.

6.3 Results

As we evolve the three bulgeless models with progressively higher resolutions, bars form in their disks. For the model with a bulge we have evolved with only one resolution (low resolution) as bulges decrease the angular momentum transfer to halos (Kataria & Das, 2018). We have calculated the bar strength A_2/A_0 and pattern speed Ω_p as defined in the previous study (Kataria & Das, 2018). Fig. 6.5 shows the bar strength evolution with time for all the models. We find that in all the models, the bar formation time (which is defined as the time when the bar reaches a strength of 0.2) is similar and has a value of $\sim$1.2 Gyr, except for model M (with 5×10^5 disk particles) which takes slightly longer (by 0.3 Gyr). However, the time when the bar reaches it's peak value is different for all the three models (Fig. 6.5). We also see that model with a bulge forms a bar later as discussed in chapter 3. Fig.6.6 shows the pattern speed evolution in the models; the variations in pattern speeds are similar for all bulgeless models and the final pattern speed values are close to each other. However, the rate of decrease in pattern speed for model M is larger compared to the other two models. The pattern speed of the model with bulge is different as discussed in chapter 5.

Since the bar transfers angular momentum from the disk to the halo, it has the potential to alter the dark matter profile in the inner region. We have examined the halo profile variation in all three simulations of increasing particle resolution. Fig. 6.7 shows the time evolution of the halo profile for the L model or low resolution simulation with 10^5 disk particles. We find that the initial cuspy halo becomes a core within 4 Gyr of isolated evolution. For the medium resolution simulation (model M) with 5×10^5 disk particles, the initial cuspy halo forms a weak core within 4 Gyr of evolution. In the high resolution simulation (model H) that has 10^6 disk particles (Fig. 6.10), the halo cusp does not get affected by the bar in 4 Gyr. We further evolved model H up to 8 Gyr and found that a weak core forms in the inner part of the dark matter halo. We have plotted the inner dark matter angular momentum variation in Fig. 6.11 for all the simulation in order to check transfer of angular momentum to the inner dark matter

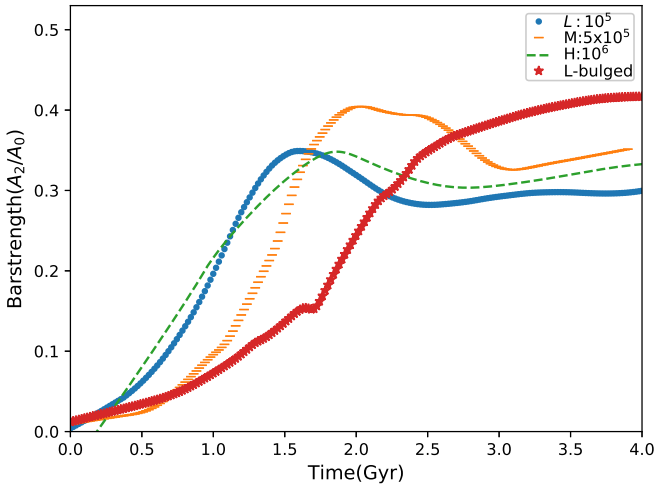

Fig. 6.5 The time evolution of bar strength has been shown with increasing the resolution of simulation.

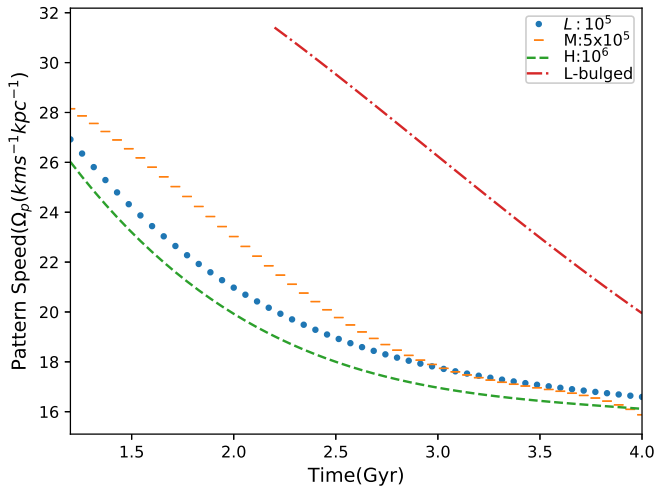

Fig. 6.6 Above figure shows the time evolution of bar pattern speed with increasing resolution of the simulations.

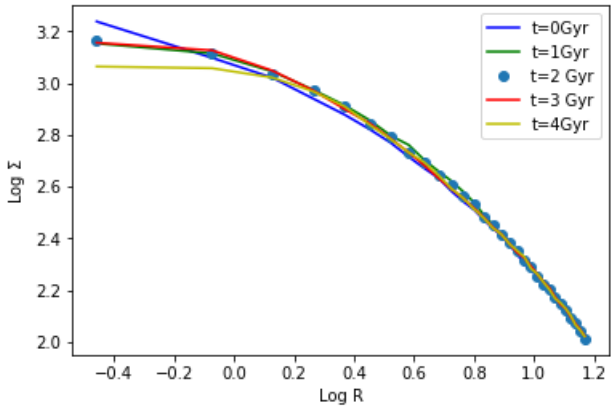

Fig. 6.7 Time evolution of halo profile in low resolution simulation having 10^5 disk particles. Cusp of the halo dissolves in to a core within 4 Gyr of evolution.

halo component within a 2 kpc cylinder of infinite length. We see that as the resolution of simulation increases, the total gain in angular momentum by the inner halo reduces.

6.4 Discussion

Studies clearly show that bars transfer angular momentum from disks to halos (Kataria & Das, 2018). Weinberg & Katz (2002) have earlier shown that bars transfer angular momentum to the halo through inner resonances and this can alter the dark matter halo profile within a few dynamical timescales. This result was in contradiction with Dubinski et al. (2009) where they find that a halo retains its cusp even after the disk becomes bar unstable. The reason for the contradicting results could be the nature of the bars in both simulations. Bars can be thin or thick depending on whether the axis ratios b/a is less than or greater than $b/a = 0.3$. If bars are thick, then halo retains its cuspiness while it is not the case with thin bars. We find that the bar in our low resolution simulation is thick with $b/a > 0.3$ (model L) while in higher resolution simulations (models M and H) the bar is thin with $b/a < 0.3$. This agrees with the earlier conclusion by Dubinski et al. (2009), as halo cusps are retained for longer time in high resolution simulation that have thin bars.

The reason for the difference in halo cusp profiles in models with thin and thick bars is that the rate of transfer of angular momentum from disk to halo is different for different b/a values. This is clearly seen in Fig. 6.11, where the bars in the low resolution simulations (thick bars) transfer more angular momentum compared to the thin bars (models M and H).

Our high resolution simulation results show that halo cusps can be ultimately eroded by bars to core profiles, but it takes 7 Gyr of secular evolution before this transformation takes

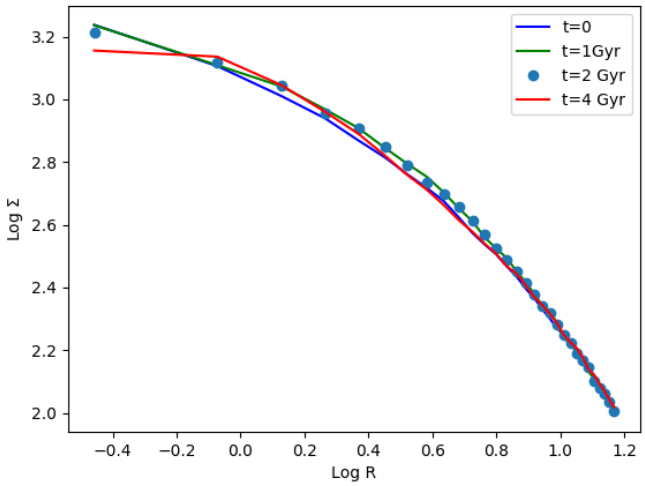

Fig. 6.8 This figure shows the evolution of the halo profile of the model with a bulge that has resolution similar to model L. We see that the halo profile changes from cusp to core within 4 Gyr but the cusp to core transition is weak compared to the bulgeless similar resolution model.

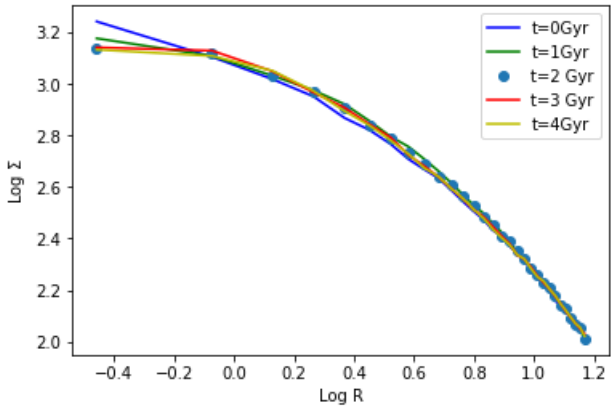

Fig. 6.9 This show the evolution of halo profile for the medium resolution simulation having 5×10^5.

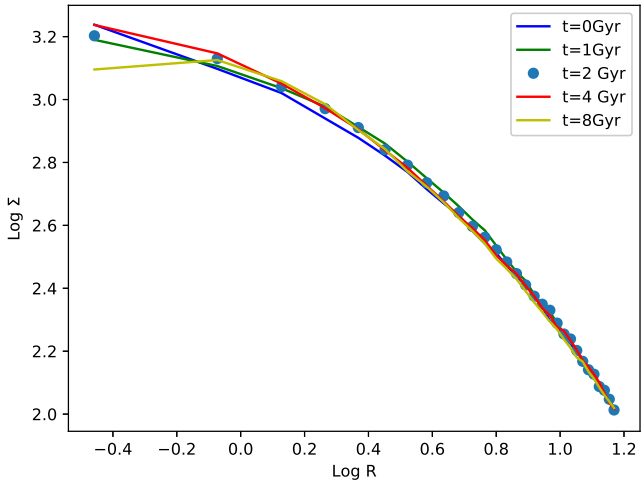

Fig. 6.10 Time evolution of dark matter halo profile for the high resolution simulation having 10^6 disk particles. We see weak cusp to core transition after 8 Gyr of evolution.

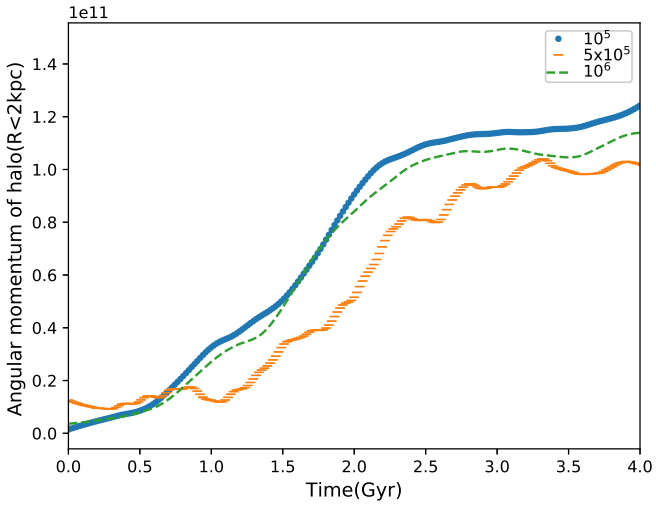

Fig. 6.11 The time variation of angular momentum of halo particles which are within a infinitely long cylinder of radius 2kpc, has been shown for the three resolution simulations namely L, M and H.

place. This is a fairly long time compared to secular evolution timescales to be meaningful. Instead, other processes like galaxy mergers and tidal interactions which produce much larger exchanges of angular momentum maybe more important for altering dark matter halo profiles.

Our study also includes a model with a bulge, to see how bulges effect cusp-core transitions. The presence of a bulge delays bar formation as well as suppressing angular momentum transfer to the halo. We find that cusp-core transition is much slower in galaxies with a bulge (Fig. 6.8).

6.5 Summary

We test the role of bars in altering the inner dark matter halo profiles of disk galaxies. We start with cuspy halo models that have disks of increasing number of particles i.e. higher resolution. The disks in our models are bar unstable and form bars around 1.2 Gyr of isolated evolution. We find that the transfer of angular momentum from the disk to the halos by bars depends on the resolution of the simulations. For the high resolution simulations, it takes $\sim$7 Gyr to transform the halo cusp into a core. We find that the presence of a bulge increases this timescale even further. Thus our study suggests that the timescales of cusp to core transition due to bars is too long to be meaningful for isolated galaxy evolution scenarios.

If you want to make an apple pie from scratch, you must first create the universe.

Carl Sagan

7

Conclusion and Future Work

In this chapter we summarize the main conclusions of this thesis. We also provide a brief overview of our future directions of work in the field.

In the first part of our thesis we have used N-body simulations of bar formation in an isolated galaxy to study the effect of bulge mass and bulge concentration on bar formation and its evolution. Our simulations of different bulge concentration models show that there is an upper cut-off in bulge to disk mass ratio M_b/M_d above which bars cannot form; the cut-off is smaller for denser bulges (Mb/Md = 0.2) compared to less dense ones ($M_b/M_d = 0.5$). We define a new criterion for bar formation in terms of bulge to disk radial force ratio (F_b/F_d) at the disk scale length above which bars cannot form and show that if $F_b/F_d > 0.35$, a disk is stable against bar formation (Kataria & Das, 2018). We further cross check our results with the observations of galaxies which require the following observable quantities: bulge masses, disk scale lengths and rotation velocities of galaxies at disk scale lengths.

In the second part of thesis we test the theoretical prediction using observational data obtained from the literature. Our sample consists of 39 barred galaxies with a wide range of Hubble classes from the *S*4*G* catalogue (Salo et al., 2015) for which bulge, disk and bar decomposition have been done. We find that all of our sample galaxies satisfy the condition F_b/F_d <0.35 and hence agree with the theoretical bar formation criterion given by simulations,

even though a few galaxies in the sample have very massive bulges. We find that this criterion have few caveats: (a) it is valid for galaxies which has just formed a bar, (b) the effect of velocity dispersion which is a result of several physical processes like spiral arms, interactions and mergers has not been included, but may be important.

In the third part of thesis work we investigate how the mass of the central spheroidal component, the bulge, affects bar pattern speeds. We find that the decrease in bar pattern speed clearly depends on bulge mass in galaxies and decreases faster for those with more massive bulges. We also find that the gain in angular momentum by bulges is larger for more massive bulges. Our results indicate that the dynamical friction of bulges on bars results in the slowdown of their pattern speeds, which is similar to the dynamical friction exerted by galaxy halos on bars. We discuss the implications of our results for observations of bar pattern speeds in galaxies.

In the final part of thesis work we have looked into one of the major and long standing problems of the widely accepted Lambda CDM cosmological model, the core-cusp problem (de Blok, 2010). There have been several attempts to resolve this problem, which includes baryonic processes such as supernova feedback and infalling satellites. But there is no general solution to this problem, which can explain the observed flat core nature of dark matter halos in all disk galaxies. In this study we use N-body simulations to investigate whether bar instabilities can erode cuspy dark matter halo profiles and change them into flatter core profiles. We find that the resolution of the simulations plays an important role in determining the final results, as the cusp to core transition occurs for only low resolution simulations. As the resolution is increased, i.e. number of disk particles becomes larger, the cusp-to-core transition takes $\sim 7 \times 10^9$ years which is too long to be meaningful for eroding the cusps of dark matter halos.

In the future we would like to see the effect of gas component on the bar formation criterion. The gas component having dissipative nature and angular momentum exchange property, will add to better understanding of disk galaxy evolution. As cold gas forms stars in galaxy disks, it can affect the kinematics of the stars and we would like to know how important is this effect. Also, we know that bars buckle during secular evolution, often forming boxy or pseudo bulges. We would like to study how the metallicity of pseudo bulges are connected with the disks and the original bar structures.

References

Aguerri J. A. L., Balcells M., Peletier R. F., 2001, *A & A*, 367, 428

Aguerri J. A. L., Méndez-Abreu J., Corsini E. M., 2009, *A & A*, 495, 491

Aguerri J. A. L., et al., 2015, *A & A*, 576, A102

Algorry D. G., et al., 2017, *MNRAS*, 469, 1054

Athanassoula E., 1992, *MNRAS*, 259, 345

Athanassoula E., 2002, *ApJL*, 569, L83

Athanassoula E., 2003, *MNRAS*, 341, 1179

Athanassoula E., 2005, *MNRAS*, 358, 1477

Athanassoula E., 2007, *MNRAS*, 377, 1569

Athanassoula E., Misiriotis A., 2002, *MNRAS*, 330, 35

Athanassoula E., Sellwood J. A., 1986, *MNRAS*, 221, 213

Athanassoula E., Morin S., Wozniak H., Puy D., Pierce M. J., Lombard J., Bosma A., 1990, *MNRAS*, 245, 130

Athanassoula E., Lambert J. C., Dehnen W., 2005, *MNRAS*, 363, 496

Babusiaux C., Gilmore G., 2005, *MNRAS*, 358, 1309

Barazza F. D., Jogee S., Marinova I., 2008, 396, 351

Barnes J. E., 2011, ZENO: N-body and SPH Simulation Codes (ascl:1102.027)

Barnes J. E., Hernquist L. E., 1991, *ApJL*, 370, L65

Barnes J., Hut P., 1986, *Nature*, 324, 446

Barway S., Wadadekar Y., Kembhavi A. K., 2011, *MNRAS*, 410, L18

Barway S., Saha K., Vaghmare K., Kembhavi A. K., 2016, *MNRAS*, 463, L41

Baugh C. M., Cole S., Frenk C. S., 1996, *MNRAS*, 283, 1361

Benjamin R. A., et al., 2003, *Pub. Astron. Soc. Pac.*, 115, 953

Berentzen I., Shlosman I., Martinez-Valpuesta I., Heller C. H., 2007, *ApJ*, 666, 189

Bertin G., 2014, Dynamics of Galaxies

Binney J., Merrifield M., 1998, Galactic Astronomy

Binney J., Tremaine S., 2008, Galactic Dynamics: Second Edition

Binney J., Gerhard O. E., Stark A. A., Bally J., Uchida K. I., 1991, *MNRAS*, 252, 210

Binney J. J., Dehnen W., Evans N. W., Hafner R., 1997, in IAU Joint Discussion. p. 33

Bissantz N., Gerhard O., 2002, *MNRAS*, 330, 591

Blitz L., Spergel D. N., 1991, *ApJ*, 379, 631

Blumenthal G. R., Faber S. M., Flores R., Primack J. R., 1986, *ApJ*, 301, 27

Bosma A., 1978, PhD thesis, -

Bosma A., 1981a, *AJ*, 86, 1791

Bosma A., 1981b, *AJ*, 86, 1825

Bottinelli L., Gouguenheim L., Fouque P., Paturel G., 1996, VizieR Online Data Catalog, 7136

Bournaud F., Combes F., 2002, *A & A*, 392, 83

Bournaud F., Jog C. J., Combes F., 2007, *A & A*, 476, 1179

Bovy J., Rix H.-W., 2013, The Astrophysical Journal, 779, 115

Bullock J. S., Kolatt T. S., Sigad Y., Somerville R. S., Kravtsov A. V., Klypin A. A., Primack J. R., Dekel A., 2001, *MNRAS*, 321, 559

Burkert A., 1995, *ApJL*, 447, L25

Buta R., Combes F., 1996, Fund. Cosmic Physics, 17, 95

Buta R., Laurikainen E., Salo H., Block D. L., Knapen J. H., 2006, *AJ*, 132, 1859

Buta R., Laurikainen E., Salo H., Knapen J. H., 2010, *ApJ*, 721, 259

Buta R. J., et al., 2015, *ApJ Suppl.*, 217, 32

Byrd G. G., Valtonen M. J., Sundelius B., Valtaoja L., 1986, *A & A*, 166, 75

Cabrera-Lavers A., González-Fernández C., Garzón F., Hammersley P. L., López-Corredoira M., 2008, *A & A*, 491, 781

Cao L., Mao S., Nataf D., Rattenbury N. J., Gould A., 2013, *MNRAS*, 434, 595

Chandrasekhar S., 1943, *ApJ*, 97, 255

Chirikov B. V., 1979, Physics Reports, 52, 263

Christodoulou D. M., Shlosman I., Tohline J. E., 1995, *ApJ*, 443, 551

Churchwell E., et al., 2005a, GLIMPSE II: Imaging the Central +/-10 Degrees of the Galactic Plane with IRAC, Spitzer Proposal

Churchwell E. B., Benjamin R. A., GLIMPSE Team 2005b, in American Astronomical Society Meeting Abstracts #206. p. 54.04

Combes F., 2008, arXiv e-prints, p. arXiv:0811.0153

Combes F., Elmegreen B. G., 1993, *A & A*, 271, 391

Combes F., Sanders R. H., 1981, *A & A*, 96, 164

Combes F., Debbasch F., Friedli D., Pfenniger D., 1990, *A & A*, 233, 82

Contopoulos G., 1980, *A & A*, 81, 198

Contopoulos G., Papayannopoulos T., 1980, *A & A*, 92, 33

Corsini E. M., 2008, in Bureau M., Athanassoula E., Barbuy B., eds, IAU Symposium Vol. 245, Formation and Evolution of Galaxy Bulges. pp 125–128 (arXiv:0709.3815), doi:10.1017/S1743921308017444

Courtois H. M., Tully R. B., 2015, *MNRAS*, 447, 1531

Curir A., Mazzei P., Murante G., 2006, *A & A*, 447, 453

Das M., Teuben P. J., Vogel S. N., Regan M. W., Sheth K., Harris A. I., Jefferys W. H., 2003, *ApJ*, 582, 190

Das M., Laurikainen E., Salo H., Buta R., 2008, *Astrophys. Space Sci.*, 317, 163

Debattista V. P., Sellwood J. A., 1996, in Buta R., Crocker D. A., Elmegreen B. G., eds, Astronomical Society of the Pacific Conference Series Vol. 91, IAU Colloq. 157: Barred Galaxies. p. 357

Debattista V. P., Sellwood J. A., 2000, *ApJ*, 543, 704

Debattista V. P., Carollo C. M., Mayer L., Moore B., 2004, *ApJL*, 604, L93

Debattista V. P., Mayer L., Carollo C. M., Moore B., Wadsley J., Quinn T., 2006, *ApJ*, 645, 209

Dekel A., Devor J., Hetzroni G., 2003, *MNRAS*, 341, 326

Del Popolo A., Le Delliou M., 2017, Galaxies, 5, 17

Díaz-García S., Salo H., Laurikainen E., Herrera-Endoqui M., 2016, *A & A*, 587, A160

Drury L. O., 1980, *MNRAS*, 193, 337

Dubinski J., Berentzen I., Shlosman I., 2009, *ApJ*, 697, 293

Dwek E., et al., 1995, *ApJ*, 445, 716

Efstathiou G., Lake G., Negroponte J., 1982, *MNRAS*, 199, 1069

Eggen O. J., Lynden-Bell D., Sandage A. R., 1962, *ApJ*, 136, 748

El-Zant A., Shlosman I., Hoffman Y., 2001, *ApJ*, 560, 636

Elmegreen D. M., 1996, in Block D. L., Greenberg J. M., eds, Astrophysics and Space Science Library Vol. 209, New Extragalactic Perspectives in the New South Africa. p. 275, doi:10.1007/978-94-009-0335-7_33

Elmegreen D. M., 1998, Galaxies and galactic structure

Elmegreen B. G., Elmegreen D. M., 1985, *ApJ*, 288, 438

Elmegreen B. G., Elmegreen D. M., Chromey F. R., Hasselbacher D. A., Bissell B. A., 1996, *AJ*, 111, 2233

Elmegreen B. G., Elmegreen D. M., Hirst A. C., 2004, *ApJ*, 612, 191

Elmegreen B. G., Elmegreen D. M., Knapen J. H., Buta R. J., Block D. L., Puerari I., 2007, *ApJL*, 670, L97

Erwin P., 2005, *MNRAS*, 364, 283

Erwin P., Debattista V. P., 2013, *MNRAS*, 431, 3060

Erwin P., Sparke L. S., 2003, The Astrophysical Journal Supplement Series, 146, 299

Eskridge P. B., et al., 2000, *AJ*, 119, 536

Faber S. M., Lin D. N. C., 1983, *ApJL*, 266, L17

Fabian A. C., Thomas P. A., Fall S. M., White R. E. I., 1986, *MNRAS*, 221, 1049

Fathi K., Beckman J. E., Piñol-Ferrer N., Hernand ez O., Martínez-Valpuesta I., Carignan C., 2009, *ApJ*, 704, 1657

Fisher D. B., Drory N., 2008, *AJ*, 136, 773

Flores R. A., Primack J. R., 1994, *ApJL*, 427, L1

Freeman K., et al., 2013, *MNRAS*, 428, 3660

Freudenreich H. T., 1998, *ApJ*, 492, 495

Fridman A. M., Poliachenko V. L., 1984, Physics of gravitating systems. II - Nonlinear collective processes: Nonlinear waves, solitons, collisionless shocks, turbulence. Astrophysical applications

Gadotti D. A., 2009, *MNRAS*, 393, 1531

Gadotti D. A., 2011, *MNRAS*, 415, 3308

Gelato S., Sommer-Larsen J., 1999, *MNRAS*, 303, 321

Genina A., et al., 2018, *MNRAS*, 474, 1398

Gerhard O., 2002, in Da Costa G. S., Sadler E. M., Jerjen H., eds, Astronomical Society of the Pacific Conference Series Vol. 273, The Dynamics, Structure History of Galaxies: A Workshop in Honour of Professor Ken Freeman. p. 73 (arXiv:astro-ph/0203109)

Gerhard O., Martinez-Valpuesta I., 2012, *ApJL*, 744, L8

Gerin M., Combes F., Athanassoula E., 1990, *A & A*, 230, 37

Giovanardi C., Krumm N., Salpeter E. E., 1983, *AJ*, 88, 1719

Goerdt T., Moore B., Read J., Stadel J., 2013, in SnowPAC 2013 - Black Hole Fingerprints: Dynamics, Disruptions and Demographics. p. 44

Goldreich P., Lynden-Bell D., 1965, *MNRAS*, 130, 97

Graham A. W., Worley C. C., 2008, *MNRAS*, 388, 1708

Guo R., Mao S., Athanassoula E., Li H., Ge J., Long R. J., Merrifield M., Masters K., 2019, *MNRAS*, 482, 1733

Harko T., Madarassy E. J. M., 2012, Journal of Cosmology and Astroparticle Physics, 2012, 020

Hinshaw G., et al., 2013, *ApJ Suppl.*, 208, 19

Hohl F., 1971, *ApJ*, 168, 343

Hohl F., 1976, *AJ*, 81, 30

Holley-Bockelmann K., Weinberg M., Katz N., 2005, *MNRAS*, 363, 991

Honey M., Das M., Ninan J. P., Manoj P., 2016, *MNRAS*, 462, 2099

Hopkins P. F., Cox T. J., Younger J. D., Hernquist L., 2009, *ApJ*, 691, 1168

Hopkins P. F., et al., 2010, *ApJ*, 715, 202

Hoyle B., et al., 2011, *MNRAS*, 415, 3627

Hubble E. P., 1926, *ApJ*, 64

Jalali M. A., 2007, *ApJ*, 669, 218

James R. A., Sellwood J. A., 1978, *MNRAS*, 182, 331

Jing Y. P., Suto Y., 2000, *ApJL*, 529, L69

Jogee S., et al., 2004, *ApJL*, 615, L105

Julian W. H., Toomre A., 1966, *ApJ*, 146, 810

Kalnajs A. J., 1972, *ApJ*, 175, 63

Kalnajs A. J., 1977, *ApJ*, 212, 637

Kalnajs A. J., 1978, in Berkhuijsen E. M., Wielebinski R., eds, IAU Symposium Vol. 77, Structure and Properties of Nearby Galaxies. p. 113

Kataria S. K., Das M., 2018, *MNRAS*, 475, 1653

Kauffmann G., White S. D. M., Guiderdoni B., 1993, *MNRAS*, 264, 201

Kilborn V. A., Forbes D. A., Barnes D. G., Koribalski B. S., Brough S., Kern K., 2009, *MNRAS*, 400, 1962

Kim T., Gadotti D. A., Sheth K., Lee M., S4G Team 2014, in American Astronomical Society Meeting Abstracts #223. p. 205.03

Klypin A., Valenzuela O., Colín P., Quinn T., 2009, *MNRAS*, 398, 1027

Knapen J. H., Shlosman I., Peletier R. F., 2000, *ApJ*, 529, 93

Kormendy J., 1983, *ApJ*, 275, 529

Kormendy J., Kennicutt Jr. R. C., 2004, *Anu Rev. in Astronomy and Astrophysics.*, 42, 603

Kormendy J., Drory N., Bender R., Cornell M. E., 2010, *ApJ*, 723, 54

Kulsrud R. M., Mark J. W. K., Caruso A., 1971, *Astrophys. Space Sci.*, 14, 52

Kuzio de Naray R., Spekkens K., 2011, *ApJL*, 741, L29

Laurikainen E., Salo H., Buta R., Knapen J. H., 2007, *MNRAS*, 381, 401

Lee Y. H., Ann H. B., Park M.-G., 2019, *ApJ*, 872, 97

Lelli F., McGaugh S. S., Schombert J. M., 2016, *AJ*, 152, 157

Li Z.-Y., Shen J., 2012, *ApJL*, 757, L7

Licquia T. C. andNewman J. A., 2016, *ApJ*, 831, 71

Lindblad P. A. B., Lindblad P. O., Athanassoula E., 1996, *A & A*, 313, 65

Long S., Shlosman I., Heller C., 2014, *ApJL*, 783, L18

López-Corredoira M., Cabrera-Lavers A., Gerhard O. E., 2005, *A & A*, 439, 107

Lynden-Bell D., 1979, *MNRAS*, 187, 101

Lynden-Bell D., Kalnajs A. J., 1972, *MNRAS*, 157, 1

Machado R. E. G., Athanassoula E., Rodionov S., 2012, in Capuzzo-Dolcetta R., Limongi M., Tornambè A., eds, Astronomical Society of the Pacific Conference Series Vol. 453, Advances in Computational Astrophysics: Methods, Tools, and Outcome. p. 363 (arXiv:1207.3452)

Makarov D., Prugniel P., Terekhova N., Courtois H., Vauglin I., 2014, *A & A*, 570, A13

Marinova I., Jogee S., 2007, *ApJ*, 659, 1176

Martinez-Valpuesta I., Shlosman I., 2004, *ApJL*, 613, L29

Martinez-Valpuesta I., Shlosman I., Heller C., 2006, *ApJ*, 637, 214

Martizzi D., Teyssier R., Moore B., Wentz T., 2012, *MNRAS*, 422, 3081

Mayer L., Wadsley J., 2004, *MNRAS*, 347, 277

McGaugh S. S., 2018, Research Notes of the American Astronomical Society, 2, 156

McGaugh S. S., Schombert J. M., Bothun G. D., de Blok W. J. G., 2000, *ApJL*, 533, L99

McMillan P. J., 2011, *MNRAS*, 414, 2446

McWilliam A., Zoccali M., 2010, *ApJ*, 724, 1491

Meidt S. E., Rand R. J., Merrifield M. R., Shetty R., Vogel S. N., 2008, *ApJ*, 688, 224

Meidt S. E., Rand R. J., Merrifield M. R., 2009, *ApJ*, 702, 277

Melvin T., et al., 2014, *MNRAS*, 438, 2882

Menéndez-Delmestre K., Sheth K., Schinnerer E., Jarrett T. H., Scoville N. Z., 2007, *ApJ*, 657, 790

Merritt D., Hernquist L., 1991, *ApJ*, 376, 439

Miwa T., Noguchi M., 1998, *ApJ*, 499, 149

Monaghan J. J., Lattanzio J. C., 1985, *A & A*, 149, 135

Moore B., 1994, *Nature*, 370, 629

Moore B., Lake G., Katz N., 1998, *ApJ*, 495, 139

Naab T., et al., 2014, *MNRAS*, 444, 3357

Nair P. B., Abraham R. G., 2010, *ApJL*, 714, L260

Nataf D. M., Udalski A., Gould A., Fouqué P., Stanek K. Z., 2010, *ApJL*, 721, L28

Navarro J. F., 1995, arXiv e-prints, pp astro–ph/9511016

Navarro J. F., Frenk C. S., White S. D. M., 1996, *ApJ*, 462, 563

Navarro J. F., Frenk C. S., White S. D. M., 1997, *ApJ*, 490, 493

Noguchi M., 1987, *MNRAS*, 228, 635

Norman C. A., Sellwood J. A., Hasan H., 1996, *ApJ*, 462, 114

Oñorbe J., Boylan-Kolchin M., Bullock J. S., Hopkins P. F., Kereš D., Faucher-Giguère C.-A., Quataert E., Murray N., 2015, *MNRAS*, 454, 2092

O'Neill J. K., Dubinski J., 2003, *MNRAS*, 346, 251

Oh S.-H., Brook C., Governato F., Brinks E., Mayer L., de Blok W. J. G., Brooks A., Walter F., 2011, *AJ*, 142, 24

Ostriker J. P., Peebles P. J. E., 1973, *ApJ*, 186, 467

Palmer P. L., Papaloizou J., Allen A. J., 1990, *MNRAS*, 243, 282

Paturel G., Theureau G., Bottinelli L., Gouguenheim L., Coudreau-Durand N., Hallet N., Petit C., 2003, *A & A*, 412, 57

Pence W. D., Chiappetti L., Page C. G., Shaw R. A., Stobie E., 2010, *A & A*, 524, A42

Peng C. Y., Ho L. C., Impey C. D., Rix H.-W., 2002, *AJ*, 124, 266

Peng C. Y., Ho L. C., Impey C. D., Rix H.-W., 2010, *AJ*, 139, 2097

Pérez I., Fux R., Freeman K., 2004, *A & A*, 424, 799

Pfenniger D., Friedli D., 1991, *A & A*, 252, 75

Pfenniger D., Norman C., 1990, *ApJ*, 363, 391

Pfenniger D., Combes F., Martinet L., 1994, *A & A*, 285, 79

Piñol-Ferrer N., Fathi K., Carignan C., Font J., Hernandez O., Karlsson R., van de Ven G., 2014, *MNRAS*, 438, 971

Polyachenko E. V., 2004, *MNRAS*, 348, 345

Polyachenko E. V., 2013, Astronomy Letters, 39, 72

Polyachenko E. V., Berczik P., Just A., 2016, *MNRAS*, 462, 3727

Pontzen A., Governato F., 2012, *MNRAS*, 421, 3464

Portail M., Wegg C., Gerhard O., Martinez-Valpuesta I., 2015, *MNRAS*, 448, 713

Portail M., Wegg C., Gerhard O., Ness M., 2017, *MNRAS*, 470, 1233

Quinn T., Katz N., Stadel J., Lake G., 1997, arXiv e-prints, pp astro–ph/9710043

Rafikov R. R., 2001, *MNRAS*, 323, 445

Raha N., Sellwood J. A., James R. A., Kahn F. D., 1991, *Nature*, 352, 411

Rand R. J., Wallin J. F., 2004, *ApJ*, 614, 142

Rattenbury N. J., Mao S., Sumi T., Smith M. C., 2007, *MNRAS*, 378, 1064

Rautiainen P., Salo H., Laurikainen E., 2008, *MNRAS*, 388, 1803

Reese A. S., Williams T. B., Sellwood J. A., Barnes E. I., Powell B. A., 2007, *AJ*, 133, 2846

Robles V. H., Matos T., 2013, *ApJ*, 763, 19

Romano-Díaz E., Shlosman I., Heller C., Hoffman Y., 2008, *ApJL*, 687, L13

Romeo A. B., 1992, *MNRAS*, 256, 307

Romeo A. B., Wiegert J., 2011, *MNRAS*, 416, 1191

Rubin V. C., Ford W. K. J., Thonnard N., 1978, *ApJL*, 225, L107

Saha K., 2015, *ApJL*, 806, L29

Saha K., Naab T., 2013, *MNRAS*, 434, 1287

Saha K., Martinez-Valpuesta I., Gerhard O., 2012, *MNRAS*, 421, 333

Saha K., Gerhard O., Martinez-Valpuesta I., 2016, *A & A*, 588, A42

Saito R. K., et al., 2012, *A & A*, 537, A107

Salo H., 1991, *A & A*, 243, 118

Salo H., et al., 2015, VizieR Online Data Catalog, 221

Sandage A., Bedke J., 1994, The Carnegie Atlas of Galaxies. Volumes I, II.

Scannapieco C., Athanassoula E., 2012, *MNRAS*, 425, L10

Schaye J., et al., 2015, *MNRAS*, 446, 521

Seigar M. S., Harrington A., Treuthardt P., 2018, *MNRAS*, 481, 5394

Sellwood J. A., 1980, *A & A*, 89, 296

Sellwood J. A., 1989, *MNRAS*, 238, 115

Sellwood J. A., 1996, *ApJ*, 473, 733

Sellwood J. A., 2006, *ApJ*, 637, 567

Sellwood J. A., 2008, *ApJ*, 679, 379

Sellwood J. A., 2014, Reviews of Modern Physics, 86, 1

Sellwood J. A., Evans N. W., 2001, *ApJ*, 546, 176

Sellwood J. A., Merritt D., 1994, *ApJ*, 425, 530

Sellwood J. A., Moore E. M., 1999, *ApJ*, 510, 125

Sellwood J. A., Sparke L. S., 1988, *MNRAS*, 231, 25P

Sellwood J. A., Wilkinson A., 1993, Reports on Progress in Physics, 56, 173

Shen J., Sellwood J. A., 2004, *ApJ*, 604, 614

Shen J., Rich R. M., Kormendy J., Howard C. D., De Propris R., Kunder A., 2010, *ApJL*, 720, L72

Sheth K., et al., 2008, *ApJ*, 675, 1141

Simmons B. D., et al., 2014, *MNRAS*, 445, 3466

Skibba R. A., et al., 2012, *MNRAS*, 423, 1485

Skrutskie M. F., et al., 2006, *AJ*, 131, 1163

Sofue Y., Tutui Y., Honma M., Tomita A., Takamiya T., Koda J., Takeda Y., 1999, *ApJ*, 523, 136

Springel V., 2005, *MNRAS*, 364, 1105

Springel V., Di Matteo T., Hernquist L., 2005, *MNRAS*, 361, 776

Stanek K. Z., Mateo M., Udalski A., Szymanski M., Kaluzny J., Kubiak M., Krzeminski W., 1994, arXiv e-prints, pp astro–ph/9410044

Stanek K. Z., Udalski A., SzymaŃski M., KałuŻny J., Kubiak Z. M., Mateo M., KrzemiŃski W., 1997, *ApJ*, 477, 163

Staveley-Smith L., Davies R. D., 1987, *MNRAS*, 224, 953

Stewart G. C., Canizares C. R., Fabian A. C., Nulsen P. E. J., 1984, *ApJ*, 278, 536

Sun A.-L., Greene J. E., Impellizzeri C. M. V., Kuo C.-Y., Braatz J. A., Tuttle S., 2013, *ApJ*, 778, 47

Teuben P., 1995, in Shaw R. A., Payne H. E., Hayes J. J. E., eds, Astronomical Society of the Pacific Conference Series Vol. 77, Astronomical Data Analysis Software and Systems IV. p. 398

Teyssier R., Moore B., Martizzi D., Dubois Y., Mayer L., 2011, *MNRAS*, 414, 195

Teyssier R., Pontzen A., Dubois Y., Read J. I., 2013, *MNRAS*, 429, 3068

Toomre A., 1964, *ApJ*, 139, 1217

Toomre A., 1981b, The structure and evolution of normal galaxies. Cambridge University Press, Cambridge

Toomre A., 1981a, in Fall S. M., Lynden-Bell D., eds, Structure and Evolution of Normal Galaxies. pp 111–136

Tremaine S., Weinberg M. D., 1984a, *MNRAS*, 209, 729

Tremaine S., Weinberg M. D., 1984b, *ApJL*, 282, L5

Tulin S., Yu H.-B., 2018, Physics Reports, 730, 1

Valenzuela O., Klypin A., 2003, *MNRAS*, 345, 406

Vásquez S., et al., 2013, *A & A*, 555, A91

Villaescusa-Navarro F., Dalal N., 2011, Journal of Cosmology and Astroparticle Physics, 2011, 024

Walter F., Brinks E., de Blok W. J. G., Bigiel F., Kennicutt Robert C. J., Thornley M. D., Leroy A., 2008, *AJ*, 136, 2563

Waugh M., et al., 2002, *MNRAS*, 337, 641

Wegg C., Gerhard O., 2013, *MNRAS*, 435, 1874

Wegg C., Gerhard O., Portail M., Martinez-Valpuesta I., 2015a, Monthly Notices of the Royal Astronomical Society, 448, 713

Wegg C., Gerhard O., Portail M., 2015b, *MNRAS*, 450, 4050

Weiland J. L., et al., 1994, *ApJL*, 425, L81

Weinberg M. D., 1985, *MNRAS*, 213, 451

Weinberg M. D., Katz N., 2002, *ApJ*, 580, 627

Weinberg M. D., Katz N., 2007a, *MNRAS*, 375, 460

Weinberg M. D., Katz N., 2007b, *MNRAS*, 375, 425

Weiner B. J., Sellwood J. A., Williams T. B., 2001, *ApJ*, 546, 931

Weinzirl T., Jogee S., Khochfar S., Burkert A., Kormendy J., 2009, *ApJ*, 696, 411

Widrow L. M., Pym B., Dubinski J., 2008, *ApJ*, 679, 1239

Wyse R. F. G., Gilmore G., Franx M., 1997, *Anu Rev. in Astronomy and Astrophysics.*, 35, 637

Yurin D., Springel V., 2014, *MNRAS*, 444, 62

Zánmar Sánchez R., Sellwood J. A., Weiner B. J., Williams T. B., 2008, *ApJ*, 674, 797

Zou Y., Shen J., Li Z.-Y., 2014, *ApJ*, 791, 11

de Blok W. J. G., 2010, Advances in Astronomy, 2010, 789293

de Vaucouleurs G., 1991, Science, 254, 1667

van Driel M., et al., 2016, VizieR Online Data Catalog, 359